

CONVICTION

Public report



Project within Trafiksäkerhet och automatiserade fordon

Author Martin Sanfridson (editor)
Date 2022-09-15



Content

1. Summary	4
2. Sammanfattning på svenska	5
3. Background	8
4. Purpose, research questions, and method	11
5. Objective	12
6. Results and deliverables	14
6.1 Fulfillment of long-term goals and project goals	14
6.2 Logging equipment for field tests	17
6.2.1 Ego motion patterns	17
6.2.2 Sensors	19
6.2.3 Supporting measurements	25
6.2.4 Target objects	28
6.2.5 Measurement platforms	34
6.3 Simulation models and results	45
6.3.1 Lidar simulation	45
6.3.2 Comparison experimental and simulated data	46
6.3.3 Ideal and physics-based sensor model	47
6.3.4 Simulation in rain and fog	48
6.3.5 Radar hardware in the loop simulation	49
6.3.6 Radar HIL over the air system setup	49
6.3.7 ASGARD1 and PROSIVIC integration	50
6.3.8 Case study: Euro NCAP CPNC scenario	51
6.3.9 Theoretical study: water on objects	54
6.3.10 Mathematical model of lidar beam interaction	54
6.3.11 Extinction and back-scattering	59
6.3.12 Rain	61
6.3.13 Fog	62
6.3.14 Simulation model: water on objects	63
6.3.15 Scenarios and materials	64
6.3.16 Varying wetting ratio	66
6.4 Calibration for field measurement	69
6.4.1 Calibration of radars used	69
6.4.2 Adjustment of radar and lidar	70
6.5 Results from field experiments	73
6.5.1 Interpretation of RCS and heatmaps	73
6.5.2 Voxel based point cloud comparison	76
6.5.3 Ford Fiesta and surrogate	80
6.5.4 Linear approach to real and soft car	86
6.5.5 MC upright, leaning, and surrogate	94
6.5.6 Kick-bike: standing, lying, and surrogate	99

6.5.7	Exploration of miscellaneous objects.....	104
7.	Dissemination and publications	112
7.1	Final event.....	112
7.2	Dissemination.....	113
7.3	Publications.....	113
8.	Conclusions and future research	114
9.	Participating parties and contact persons	120
10.	Abbreviations	121
11.	References	122

FFI in short

FFI is a partnership between the Swedish government and automotive industry for joint funding of research, innovation and development concentrating on Climate & Environment and Safety. FFI has R&D activities worth approx. €100 million per year, of which about €40 is governmental funding.

For more information: www.vinnova.se/ffi

1. Summary

The CONVICTION project started right when the restrictions of pandemic COVID 19 hit Sweden and ended about two year later in June 2022. The project has been partly financed by Vinnova/FFI (2019-05835). It was coordinated by RISE with a consortium including Volvo Cars, Asta Zero, UniqueSec, ESI Nordic and Veoneer.

A main aim of CONVICTION has been to log lidar and radar sensor data to compare soft surrogate targets and real targets by simulation and other analyses. The project has focused on the sensors, soft targets, simulation and logging tools with a vision that the embedded perception's worldview should be accurate and reliable enough for the vehicle to drive responsibly at some degree of driver automation.

The project has systematically and successfully worked towards its goals. Rigs for collecting data from lidar and radar has been built. Data has been logged at the test track. A set of typical test track surrogates have been compared to their counterparts. Analysis methods have been suggested and used to show the difference between real objects and soft models. Sensor simulation models have been improved and verified. Radar HIL has been connected to scenario-based simulation and verified against simulation and test track objects. The project has analysed and simulated how rain and fog impacts on lidar output. At the end of the project, results were presented results at an open final event.

An interesting finding for the motorcycle target is that the peak RCS towards the sides goes down when the motorcycle is leaning. This means that a turning motorcycle may be more difficult to detect.

It has been found that the RCS of a convertible car with a soft roof does not change very much when the roof is down or when it is wet. For a lidar at close range, the difference in intensity (and number of recorded hits) between a dry and wet soft roof is very small.

In collaboration with another research project, a soft kick-bike was compared to real ones, both standing and lying. It was concluded that the RCS and heatmaps are quite similar.

A combined radar HIL and scenario-based simulation has been implemented successfully. This allows for applying richer and more complex scenarios with multiple objects.

Using a voxel grid for lidar point clouds, a soft car and its real counterpart has been compared. There are a few obvious differences, like the non-transparent window on the soft car, the exterior mirrors are more pronounced at a distance in the soft car. More work is needed to conclude the usefulness of the algorithm to compare point clouds from different lidars.

Literature study and ray tracing simulations show results for various scenarios and provides a valuable understanding of the interaction and has been a basis in the development of the mathematical model. The outcome is a practical and straightforward mathematical model that provides knowledge on lidar beam interaction in adverse weather conditions and may be applied in assessments of specific scenarios to identify relevant limiting factors.

The surrogate motorcycle target appears to show similar features to its real counterpart. One possible difference from a lidar viewpoint is that the most common detection points appear to be focused to a smaller area for the soft surrogate target, which can be seen as a much higher maximum detection count per grid.

Ideas of future work include more analysis of radar and lidar performance. It includes looking more at disturbances from water on object and shield surfaces and in the air. It should also include new radars with higher resolution both for simulation models and to investigate soft targets. The functionality of radar HIL can be extended to allow for more complex scenarios.

2. Sammanfattning på svenska

CONVICTION är en sammandragning av ”COMBiNed VerIFIcATION” där idén är att jobba parallellt med radar och lidar med målsättningen att utnyttja synergieffekter. Projektet startade när pandemin Covid-19 slog till och avslutades två år senare i juni 2022. Projektet har koordinerats av RISE och deltagare har varit Veoneer, Volvo Cars, UniqueSec, Asta Zero och ESI Nordic. Projektet har varit finansierat av FFI (2019-05835) och ingående företag.

Projektet CONVICTION är uppbyggt på tre ting: radar, lidar och surrogatmål. Arbetet med loggning, simulering och dataanalys har skett med fokus på dessa tre saker. Bakgrunden är naturligtvis utvecklingen av automation för att ersätta eller hjälpa föraren vid körning, ADS eller ADAS. En bevekelsegrund till ADS/ADAS är målsättning med färre skadade och döda i trafiken, en annan bevekelsegrund är ökad produktivitet. Att automationen är tillräckligt ansvarsfull måste dock garanteras. Vid högre grad av automation (SAE driver automation level) vilar ansvaret mindre på föraren och mer på den slutna loopen med exteroceptiska sensorer som input till perception för tolkning av omvärlden och vidare till beslutsfattande (reglering på hög nivå) och utställning (reglering på lägre nivå, närmre ställdonen). Projektet fokuserar på sensorerna med syfte att perceptionens uppfattning av omvärlden ska ha tillräcklig varseblivningsförmåga för att t ex fordonstillverkare ska ha en möjlighet att garantera att fordonet kör tillräckligt ansvarsfullt.

För att vara mer specifik, har målsättningarna med projektet varit att

- Utveckla och validera noggranna och repeterbara mätmetoder för att karaktärisera typiska objekt på väg (bilar, fotgängare, mm) för radar och lidar

- Utveckla mätmetoder för radarkaraktäristik med syfte att snabbt få fram mätningar som kan användas som grund för att jämföra med lidar
- Utveckla simuleringsmodeller för lidar och verifiera mot mätningar
- Analysera komplementär karaktäristik för lidar och radar
- Delge input till internationell standardisering av metoder för mätningar av lidar och radar karaktäristik vad gäller skillnaden mellan surrogatmål och vad de ska representera
- Undersöka svåra ytor och för lidar, som t ex extremt hög eller låg reflektivitet och påverkan av t ex vatten och dimma
- Validera simuleringar av trafikscenarior gjorda på elektromagnetisk nivå med loggat data.
- Jämföra data från radarmåls-simulator med scenario-simuleringar på elektromagnetisk nivå och med uppmätta data

Projektet har systematiskt arbetat mot dessa mål under två års tid. Tidigt arbete kretsade kring att beskriva state-of-the-art, kring att koppla ihop scenariobaserad simulering med radar HIL, och kring att designa och implementera rörelsebaserade plattformar och verktyg för loggning. Arbete sent i projektet har kretsat runt att utföra mätningar, att göra simuleringar, att analysera mätningar och att skriva rapport och presentera.

Ordinarie protokollförda projektmöten över video har, med undantag för semestrar, hållits varannan vecka och det har blivit totalt 30 stycken. Ett flertal andra möten för samarbete i arbetspaketerna har också hållits. Ett dussin mätkampanjdagar har tillbringats på AstaZeros testbanor för att utveckla och utföra mätningar av olika objekt. Ett event anordnades i slutet av projektet, i maj 2022 för att lyfta fram resultaten i projektet. Det hölls i en publikt tillgänglig lokal på Volvo Cars och besöktes av 40 deltagare.

Radarn vi främst har använt i projektet är av en vanligt förekommande typ i fordonsindustrin. För att få full kontroll över inställningar och även för att få ut IQ data som grund till beräkningar, har vi använt oss av en prototyp från en Tier2-leverantör. Det är en FMCW på 77 GHz med en enkel antenn på kretskort.

I projektet har vi använt två olika typer av lidar. Velodynes lidar med roterande skanning med våglängd 905 nm och en Luminartechs lidar som skannar ett segmenterat synfält på våglängden 1550 nm och med en högre vinkelupplösning, speciellt i vertikalled. Lidar har introducerats i produktion för lyxsegmentet, men har inte slagit igenom brett på grund av hög kostnad.

Den tekniska utvecklingen av lidar är fortsatt stark; det finns ett flertal tillverkare som har olika principiella tekniska lösningar i sina produkter. Även radar har en återstartad utvecklingskurva, främst FMCW som har antenner för upplösning även i höjddled. Utvecklingen av dessa två aktiva sensorer drivs av krav för ADS/ADAS att uppfatta omgivningen med högre prestanda och robusthet. Dessa två sensortyper ses vanligen som komplement till perception baserad på monokamera. Den skillnad i modalitet som

perceptionen kan nyttja är dels avståndsinformation som följd av en aktiv sensor, dels hastighet från dopplereffekten, och dels att olika våglängder ger olika svar mot objekt och störningar.

Riggat för att samla in data från lidar och radar har byggts. Tre olika typer av grundläggande rörelsemönster har använts: linjär, cirkel och spiral. Verktyg för att hantera loggdata till analys har programmerats. Analysverktyg har förfinats. Sensordata från verkliga mål, mjuka surrogatmål, störningar och föremål som kan vara svåra att upptäcka har samlats in och analyserats. Sensormodeller har förbättrats och verifierats för simulering. Radar HIL har kopplats ihop med scenariobaserad simulering. Vattens påverkan på lidar har studerats teoretiskt och simulerats.

Vi har bland annat funnit att en lutande motorcykel får en mycket mindre radarsignatur i lutningsplanet och att det typiskt inte återspeglas vid användning av rörelseplattform och surrogatmålet i kurva. Detta kan alltså ha betydelse om en radar observerar motorcykeln från sidan. I upprätt position är annars surrogatmål och riktig motorcykel lika sett från en radar.

Den mjuka surrogatbilen vi använt oss av byggs upp av skivor varöver man drar en presenning. Presenningen representerar det yttre och bör alltså ha rätt optiska egenskaper på olika ställen för att efterlikna en generell eller en specifik bil. En typisk skillnad är att surrogatmålet inte har riktiga fönster som en optisk sensor kan se igenom. En annan skillnad tycks vara att de yttre backspeglarna kan identifieras på längre avstånd bakifrån med lidar. Med största sannolikhet är en tredje skillnad att skivorna på insidan syns på en radarvärmekarta.

En teoretisk studie baserad på härledning av lidarekvationen för vattendroppar i luft och vatten på objektets yta, ger bland annat hur vatten på det mäta objektets yta påverkar lidarsignalen. Lack, tyg och plast har studerats för olika vinklar, droppstorlekar och vattenmängder. Påverkan är typiskt svagare än för regn och dimma mellan sensor och objekt, men resultatet är förstås beroende på exakta scenariot. Generellt kan man säga att dimma släcker ut lasersignalen mer än regn, om man tittar på typiskt förekommande kvantiteter av de båda väderfenomenen. För en från början torr diffus yta kommer en vattendroppe eller vattenfilm att reflektera tillbaka någon procent mer av ljuset till lidarn. Objektets diffusa ljusspridning, som är viktig för lidar, minskar några procent. Simuleringar baserat på strålgångar stämmer väl överens med teoretiska resultaten men antalet parametrar är förstås högre.

Resultat från over-the-air radar HIL har jämförts både med simuleringar och med loggningar på provbana för Euro NCAP scenariot som kallas CPNC, där ett barn vinkelrätt kommer ut och korsar vägen initialt dold av två parkerade bilar. Jämförelserna visar god överensstämmelse när parameter som t ex egofordons hastighet ändrats. En närliggande slutsats är att radar HIL kan vara ett högst användbart verktyg för verifiering av andra parametrar.

En grundläggande svårighet är hur själva jämförelsen av sensordata t ex från olika liknande sensorer eller för olika liknande objekt ska utföras. Skillnaden går t ex att beskriva t ex med bilder där sensordata aggregerats i ett objektfixerat raster i två eller tre dimensioner. Hur användaren av lidar och radar påverkas är därefter en tolkningsfråga. Att finna relevanta nyckeltal är dock ingen lätt uppgift.

Det finns en rad utvecklingsmöjligheter som en fortsättning av det som gjorts i CONVICTION. Radar HIL riggen kan utvecklas med mer komplexa scenarier och i kombination med scenariobaserad simulering. En mer detaljerad simuleringsmodell för radar kan utvecklas och verifieras med mätdata. Störningar för lidar som härrör till vatten i luften, på sensorskydd och objekt är fortsatt mycket intressanta. Dessa störningar vill man upptäcka, kompensera för och kvantifiera i specifikation. En genomförbarhetsstudie för generering och mätning av dimma har redan körts, FFI 2021-02582. Mättriggare kan användas för att undersöka ytterligare surrogatmål. Detta har redan gjorts en första gång i samarbete med FFI 2020-02959 "Vulnerable road users - Escoter". Det finns även intressanta forskningsfrågor t ex hur ska man jämföra mätdata (t ex punktmoln) från olika objekt, störningar eller sensorer, på ett sätt som är garanterat relevant för en "black box perception" och banplanering/ beslutsfattande.

3. Background

The development of ADAS and ADS, automating the driving task to increased "SAE Levels", puts stronger requirements on reliability, and therefore on its sensory input and the interpretation of this input. Several types of exteroceptive sensors can be employed in the perception, such as visible spectrum and infrared cameras, ultrasonic sensors, laser scanners, and radars. In the CONVICTION project we have concentrated on the lidar and radar sensors. Both these sensors have seen a recent rapid development driven by the requirements of ADS. One reason for their popularity is their ability to complement vision systems with range information.

A multi-modal perception increases performance and robustness in various conditions, such as sun glare or rain. In this project we have focused on existing and standalone sensors with no sensor fusion between modalities. Another aspect of stronger requirements is the need to verify ADS/ADAS on test tracks, from a sensor viewpoint. It is important that the reflectance characteristics of the test objects match that of the real object it is representing. A test track offers repeatability and safe conditions for testing. A typical safety measure possible at a test track is to replace the real target (typically a dynamic object) with a soft one. The idea that the perception of the system under test system should not be able to discriminate between the real and a surrogate. The soft target should have similar shape, reflectivity, and motion such that all involved sensors (or rather the perception) can be deceived by the substitute.

Simulation has become important in the development of ADS/ADAS, not the least for scenario-based verification, trying to find failure modes in the complex interaction with

the vehicle's environment. The credibility of simulation relies on access to sufficiently accurate models. In this context we are interested in models that describe how a sensor captures object properties in different angles, at different ranges, at different disturbances, etc.

Adverse weather is an obstacle to increased automation since it lowers the availability of the vehicle and thus the return rate of investment. There are several overviews published on the impact of water in different forms on the common sensors, see for example [10]. In the CONVICTION project we rely on analysis and simulation as methods in the study of these phenomena. Conducting meaningful experiments, for example to verify models, requires repeatable generation and measurement of the nature and magnitude of the induced water-based disturbance. This has been considered out of scope for the project for reasons of time, lack of suitable location and budget.

In addition to desktop simulation where models of the vehicle under test are used, it is also of interest to include actual sensor hardware and its embedded software. One part of the project has worked on an open loop HIL, hardware in the loop, in which a pre-determined scenario governs the actuation. A physical sensor hardware is deceived by a front-end allowing for testing a sensor during different scenarios. To automate batches spanning a large parameter space is a way to speed up verification. In the CONVICTION project we have worked on radar HIL. For example, we have connected a Euro NCAP scenario from the test track with desktop simulation and with HIL simulation. The usefulness of each of these three tools depends on what the level of detail is needed in each case.

The CONVICTION project revolves around three items: lidars, radars and soft targets. Logging equipment for sensors have been assembled to be used at the test track. One requirement was to easily integrate new sensors, to be future proof. Another requirement was to have features for quick, at-the-test-track, testing of log quality. A good logging system is a prerequisite for the activities at the test track.

The **lidar** sensor is not yet widely found in production vehicles because of its high cost, but mostly on vehicles for ADS. There is a diversity of technical lidar solutions, which could mean that the industry is still exploring possible principal technical solutions. Some of the major technology trends are: increased number of points (angular resolution in azimuth and elevation), increased range, and runtime configurable field of view. The output for a lidar is a point cloud that is typically fused with image data in the perception, which typically is centralized rather than being integrated in each sensor.

In this project we are interested in time-of-flight lidars composed of one or multiple pairs of laser sources and detectors which are made to scan the environment. The scanning can be mechanical rotation or by small mirrors, compare for example what is used in a laser printer. The most common laser wavelength is 905 nm but there are also newer sensors at 1550 nm. The optoelectronics for the latter is more expensive but allows for much

higher power – resulting in an increased range – while maintaining the same eye safety level.

A lidar is affected by water on its shield, in the air and on the detected objects. The formation in structures like water film and water drops and the total amount of water determine the reduction in returned intensity. Spray from road-tyre contact, turbulence around the sensor's shield, cavities in the surface of the target etc., affect the formation of water. The choice of laser wavelength matters also.

Lidars typically report the number of “hits” a laser ray does each time it is emitted. For edges and for small objects a ray can hit both a foreground and a background (or more). A cloud of drops, dust or snowflakes can result in a sparse scattered cloud object in the outputted point cloud data, rendering the background partially obscured. Another example is asphalt which surface cavities are gradually flooded with increased amount of water. The type of reflection of the dry asphalt changes from diffuse to specular the more water fills the surface, turning the asphalt into a mirror even at rather close distances depending on angles.

A simulation model of the lidar and object interaction can be made at different levels of detail depending on the purpose. It is necessary to understand what phenomena are dominating in different cases.

A front mounted **radar** is typically used for ADAS features such as automatic emergency braking and adaptive cruise control. Radars mounted around the vehicle (usually in the corners) for panoramic view typically have a shorter range and are useful in ADAS features that involves lateral movements of the ego vehicle. During specific types of bad visibility condition the radar can give more valuable information than a camera or a human eye and can thus be considered indispensable for ADS SAE level 4.

Frequency Modulated Continuous Wave (FMCW) type radars operating in the 76-81 GHz band, so called millimetre wave radars, will be used in the project. The automotive radar in production today has a simple antenna which usually gives a very limited resolution in the azimuth angle compared to that of a camera or lidar. The resolution in elevation angle is even more limited. The ability to discern objects is improved by using the doppler effect, which gives the relative speed of an object in the direction along the sensors line of sight.

The radar return has a complex nature which poses a challenge for detecting and tracking of traffic objects. Clutter from the road and various objects create returns that need to be separated from the returns of the relevant targets. All pre-processing and filtering are made in the radar unit. The production radar primarily outputs a list of objects over the low bandwidth CAN interface.

Simulation of radars can be done at different levels of details. A first level of detail is to use the RCS even at close distances and keep track of the relative motion of radar and

objects. A second level of detail is to use material and geometrical properties of objects for electromagnetic wave propagation. The former is less computational intense and will be applied in the project.

A radar can be given faked responses over the air by facing it to a frontend capable of responding to the emitted chirps. The method works in general but has a few limitations. The primary use of the setup is to run sensors in a rig by replaying a scenario altering parameters of the scenario or setting of the sensor to verify its functionality. It does not have to be a loop, HIL – hardware-in-the-loop, to be useful. By putting a scenario simulation together with a HIL rig the input space will be easier to control. The scenario simulator needs to tell the frontend the location, speed and magnitude of the response.

In the more general case of VIL – vehicle in the loop – other sensors also need to be fooled in a synchronized manner: wheel encoders, gnss, camera, etc.

When it isn't possible to test scenarios that may result in collision with real vehicles, pedestrians etc. as targets and the alternative is to use harmless surrogate objects also known as **soft targets**. These surrogate targets are typically mock-up objects made of soft materials that can be repeatedly hit without damage to themselves or the test vehicle. A common soft target is a car, or even only the rear end of a car. To test with surrogate targets, the sensor response of the surrogate targets must be consistent with the response of the corresponding real target. Previously, comparing targets for lidar has not been done in any larger extent. For NIR-reflectivity of the test objects, the test target must therefore be equipped with adequate reflecting parts.

The CONVICTION project is a continuation of the two FFI projects HiFi Visual Target (2016-02496) and HiFi Radar Target (2015-04852). The HiFi Visual Target project developed and tested optical and geometrical measurement methods of soft car targets with the focus on camera sensors. The optical measurement method was unable to detect the wear of soft car targets, but the geometrical method showed more promising results regarding the degradation of the shape of soft car targets.

The HiFi Radar Target project developed measurement and analysis methods to obtain characteristic radar reflection profiles of road objects. The methods have been used to collect data for both real and surrogate car targets. Analysis methods were developed to compare the different car targets. The methods from the project could be refined, made more efficient and expanded to enable the deeper analysis that could be needed for a larger diversity in targets and the understanding as to what makes a proper surrogate for those.

4. Purpose, research questions, and method

CONVICTION is a contraction for COMbiNedVerIfiCaTION, where the aim has been to work simultaneously with lidar and radar to explore synergies.

Long-term the aims of the project are to:

- Contribute to FFI 2030 roadmap linked to analysis, knowledge and enabling technology as well as improved safety in vehicles through improved verification and validation.
- Contribute to reach the goal of VisionZero, i.e., zero deadly traffic accidents.
- Strengthen the Swedish automotive industry's competitiveness in a global perspective.
- Be part in developing AstaZero to a world class test site for ADAS and ADS.
- Build competence and knowledge within Veoneer for the development, test and validation of components and systems for ADAS and ADS related functions.
- Provide tools and methods for ADS testing to Volvo Car Corporation - an enabler for the launch of fully autonomous cars.

5. Objective

The objective of the project is to enable more efficient and reliable verification of radar and lidar sensor systems, including ADAS/ADS that rely on these sensors. The scenery of using the sensors is the test track where, for safety and cost reasons, soft targets are surrogate for cars, motorcycles, pedestrians, animals, etc. As in proceeding projects HiFi Visual Target and HiFi Radar Target, the primary interest is to characterize any discrepancy between soft targets and their real counterparts. The virtual scene of simulation with detailed sensor models is regarded as a complementary part of the test track. It is of importance that the reflectance characteristic of the test object matches that of a real object to the largest extent possible.

To be more specific the CONVICTION project's aims were:

- Develop and validate accurate and repeatable measurement methods for the radar and lidar characteristics of road objects (i.e. vehicles, vulnerable road users)
- Develop refined and simplified measurement methods for radar characteristics in order to achieve quicker measurements and analysis and a base for comparison with lidars.
- Develop simulation models for lidar measurements in order to compare the measurement methods from definition- to simulation-to verification and validation
- Analyze the complementing characteristics of lidars and radars
- Provide input to international standardization regarding methods and limits for measurement of lidar and radar characteristics of real and soft targets
- Investigate difficult surfaces and conditions for lidar sensors like e.g. extreme high and low reflectance surfaces as well as the implications of e.g. water and fog.
- Validate EM simulations in traffic scenario simulator with measured data.

- Compare Radar Radio Frequency (RF) target signal generator outputs based on 1) EM simulations and 2) measured data

6. Results and deliverables

This section describes the activities and technical results starting with an additional subsection discussing the goal fulfilment, both long-term and for the project, as listed in the previous sections 4 and 5. First, a few words on the management of the project.

The project has systematically worked towards the goals listed in section 5 for two years. Early work revolved around describing the state-of-the-art, around coupling scenario-based simulation with radar HIL, and around designing and implementing motion-based platforms and tools for logging. Work sent in the project has revolved around carrying out measurements, making simulations, analyzing measurements and writing a report.

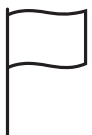
Ordinary minuted project meetings via video have been held every two weeks, with the exception of holidays. A total it came to 30 meetings in general attended by one or two people from each partner. A number of additional meetings for cooperation in the work packages have also been held. A dozen measurement campaign days have been spent on AstaZero's test tracks to develop and perform measurements of various objects.

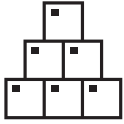
Two steering group meetings have been held. One main reason was to decide on a prolongation of the project by 3 months, which eventually was carried out.

An event organized at the end of the project, in May 2022 to highlight the results of the project. It was held in a publicly available building at Volvo Cars and was attended by 40 participants.

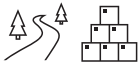
6.1 Fulfillment of long-term goals and project goals

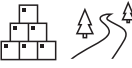
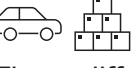
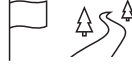
First, a repetition.

	Contribute to FFI 2030 roadmap linked to analysis, knowledge and enabling technology as well as improved safety in vehicles through improved verification and validation.
	Contribute to reaching the goal of VisionZero, i.e., zero deadly traffic accidents.
	Strengthen the Swedish automotive industry's competitiveness in a global perspective.

	Be part in developing AstaZero to a world class test site for ADAS and ADS.
	Build competence and knowledge within Veoneer for the development, test and validation of components and systems for ADAS and ADS related functions.
	Provide tools and methods for ADS testing to Volvo Car Corporation - an enabler for the launch of fully autonomous cars.

The table above repeats the long-term aims of the project. The icons are connected to the deliverables in the table below. The table below describes results and deliverables of the project.

Deliverable planned	Contribution made	Deviations
Sota report	 Knowledge building of lidar and radar technologies	
Radar and lidar test rig setup	 Construction of motion-based logging platform.	
Radar and lidar measurement methods including target analysis	 Ideas of how to measure data	
GO/NO GO test script for both radar and lidar tests	 Scripts for analysis and conversion of logged sensor data. Automated to run as a status check while at the track	
Lidar and radar reference target(s)	 Finding, constructing objects for alignment, and soft target	Low on the aim to include a large set of difficult targets
Test plan		

	Choice of scenarios and objects, reconnecting to Euro NCAP	
Radar simulations report and simulated physical sensor front-end report.	 Verification of models.	
Radar HIL demonstrator	 The demonstrator is useful for verification of radar systems, for example emergency brake	
Evaluate lidar performance in various weather condition	 Good knowledge building to understand impact of water.	Ambition outside simulation was lowered because of cost/time.
Scanned CAD models of objects	 Use of available resources to populate models for simulation	
Simulation model report – Lidar Level 1 & 2	 Scenario simulator useful for lowering cost of V&V	
Lidar demonstrator	 Three different rigs for demonstration of different lidars. Three different lidars.	
Radar and lidar measurement report	 Analysis of sensor data logged at test track. Knowledge building.	Data comparison with multiple dimensions is non-trivial
Project seminar in combination with demonstration	 Sharing results externally	

The project has contributed to FFI 2030 roadmap by working on methods and analysis to improve safety by V&V, and in a long distance also the vision zero goal. By proposing methods and evaluate on soft targets AstaZero receives a tool for future use to clarify that any soft target is adequate for use. This helps strengthen the Swedish automotive industry's competitiveness. Veoneer made a moving platform for sensor and target evaluations and build competence in V&V. Volvo Cars has built knowledge in how wet conditions affect lidar and how to evaluate lidar performance.

6.2 Logging equipment for field tests

The logging of sensors was carried out in measurement campaigns at AstaZero proving ground. One, two or three stations with different targets were set up to optimize time when up to three rigs were used simultaneously. The scenarios, targets, additional equipment and type of test prior to each campaign were planned in advance. Three major types of scenarios existed: 1) detect & recognize for understanding sensor characteristics, 2) signature characterizing the object(s) in front of the sensor, and 3) a Euro NCAP scenario with a moving ego vehicle and a moving target [7].

6.2.1 Ego motion patterns

When it comes to lidar in the project, the focus is on characterizing the targets and detach the effect of the particular lidar system used in the characterization as much as possible. Two measurement scenarios were chosen with the aim of both getting relevant data from the targets as they are most often encountered in traffic as well as getting data that represents different viewing angles and ranges. In the third scenario we have selected to work with the so called CPNC scenario, where an obscured child emerges from a straight crossing path in-front of the ego vehicle. This is the only recorded scenario in the project where a target is moving and is to be used also for SIL and HIL.

The first measurement scenario is a linear approach directly towards the front and rear of the targets, from 300 m down to 5 m, which should start outside of the expected range for the lidars used in the measurements and end close enough so that the target is still fully in the field of view of the lidars. This scenario was chosen since traffic objects are most commonly encountered from the front and rear and those are the viewing angles that the targets are most often encountered at long range during normal driving. Additionally, there are limitations with the second measurement scenario when it comes to gathering data from long range and a variety of angles due to the geometry of the test track used for the measurements. An example of a linear approach test path that is followed by the driving robot can be seen in Figure 1.

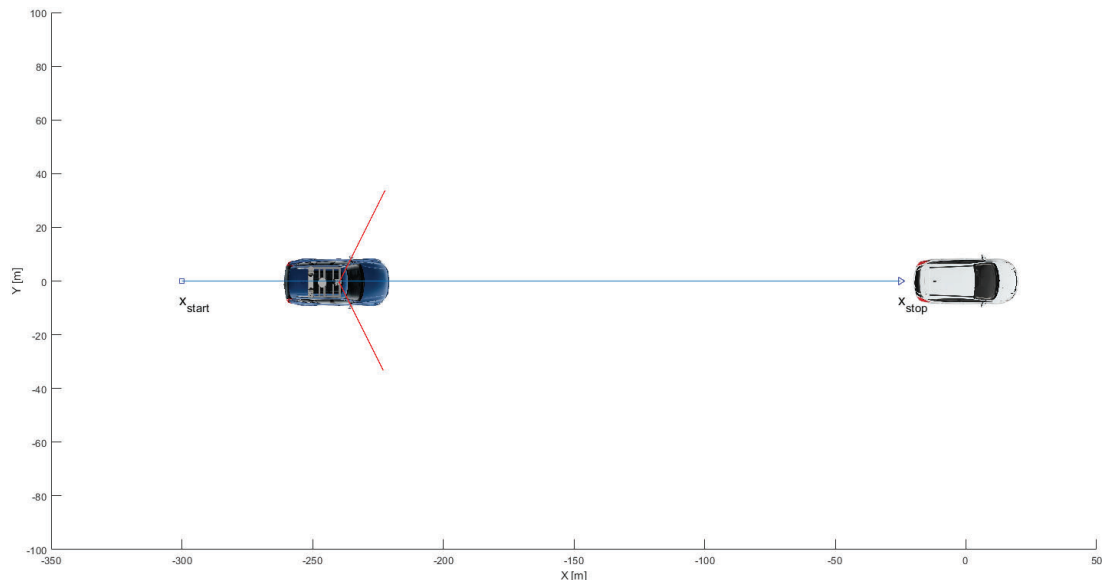


Figure 1 An example of a linear approach towards the rear of a vehicle target from from $x_{start} = 300$ m range to $x_{stop} = 5$ m.

The second measurement scenario is a fixed step spiral starting from 10 m range, ending at 100 m range with an increase of 10 m for each lap. These parameters were chosen to gather data from a variety of viewing angles and range while being able to run the scenario in one measurement on the test track in a reasonable amount of time. The driving robot is set to drive at a fixed velocity of 10 kph to allow the measurement to be run in under 20 minutes, sacrificing some resolution in the robot path to allow the measurement to be run in a short enough. An example of a spiral path driven by the driving robot in the measurement campaigns can be seen in Figure 2.

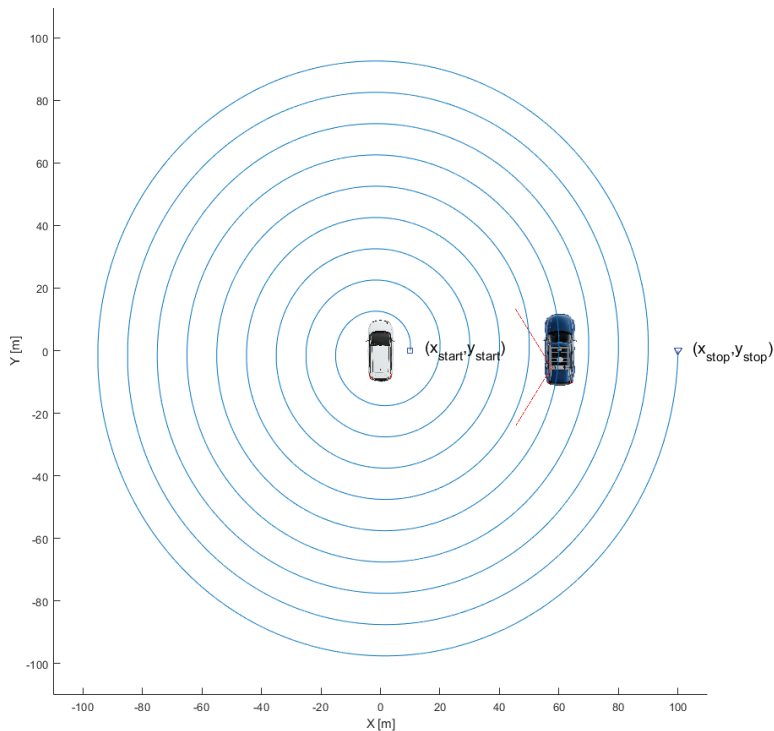


Figure 2 An example of a spiral scenario around a vehicle target from $x_{start} = 10$ m range to $x_{stop} = 100$ m range with a step size between laps of 10 m. y_{start} and y_{stop} are both 0 m.

Euro NCAP is an organisation that publishes test results regarding safety aspects. Asta Zero is a test facility that carries out Euro NCAP testing. One of the Euro NCAP areas for classification deals with unprotected vulnerable road users outside of the car (VRU). Cars with automated emergency braking (AEB) can earn scores.

The CPNC scenario of Euro NCAP is defined in [7] as “Car-to-Pedestrian Nearside Child 50% (CPNC-50) – a collision in which a vehicle travels forwards towards a child pedestrian crossing its path running from behind and obstruction from the nearside and the frontal structure of the vehicle strikes the pedestrian at 50% of the vehicle's width when no braking action is applied.” The child starts to move when the ego vehicles time to collision (TTC) to the crossing path is 4 seconds. The scenario was executed using rigs from VCC and RISE, at different initial speeds ranging from 10 to 50 km/h.

6.2.2 Sensors

This subsection describes the used automotive lidars and radar.

6.2.2.1 Luminar Hydra

The Hydra lidar from Luminar is primarily for testing and development programs and not available as a component off the shelf. A main difference compared to the Velodyne lidars is the use of 1550 nm wavelength. This wavelength permits higher power while keeping the laser safety constraints. A drawback with 1550 nm is the higher cost due to availability electro-optical components for this wavelength.

A major difference to rotating lidars is the sensor's ability to dynamically control the general pattern of laser rays. A typical scanning pattern is a gaussian distribution in the elevation direction, where it is possible to adjust the mean value (the center elevation direction) and the standard deviation (the spread of the rays around the center). Other scanning patterns are also possible, but we have used the gaussian one in the project. Scanning can be seen as horizontal lines from one side to the other for each eye (top down or bottom up), and with the possibility of interleaving lines.

The horizontal resolution can at the best be 0.07 degrees and the vertical resolution 0.03 degrees. The sensor has two "eyes", see Figure 3. The maximum horizontal field of view is 120 degrees, and the configurable vertical field of view is max 30 degrees, resulting in 200 laser points per square degree. The range claim is 250 m for objects of less than 10-% reflectivity and a maximum range of 500 m. It is possible to configure the frame scanning rate up to 30 Hz.

The hardware communication interface is a Gbit RJ45 Ethernet port. The settings of the Hydra can be controlled dynamically by communicating with for example the proprietary EnVision point cloud viewer software. The UDP/IP data can be captured and later converted to a suitable point cloud format. Besides geometrical properties, other information of primary interest are reflectivity and the ordinal of the detected echo for each received ray.



Figure 3 Luminar's Hydra lidar with two eyes slightly tilted down. The physical size is about 1x2x3 decimeters and the roof of a passenger car provides a typical mounting height. Picture borrowed from a datasheet.

6.2.2.2 Two sensors from Velodyne

The Velodyne HDL-64E is a mechanically spinning lidar operating at 905 nm consisting of a base that mounts to the vehicle and a rotating housing that spins at a constant rate. The housing contains four sets of 16 laser transmitters and two sets of 32 receivers arranged vertically to create a fixed vertical field of view from $+2.0^\circ$ to -24.9° , meaning a total vertical field of view of 26.9° . Figure 4 shows the structure of the Velodyne HDL-64E. The horizontal field of view is created by simply spinning the housing containing the transmitters and receivers at a constant speed, resulting in a 360° horizontal field of view. The rotation rate of the lidar can be adjusted to allow for a framerate between 5 Hz – 20 Hz. The default framerate is 10 Hz which corresponds to the housing rotating at a rate of 600 rpm.

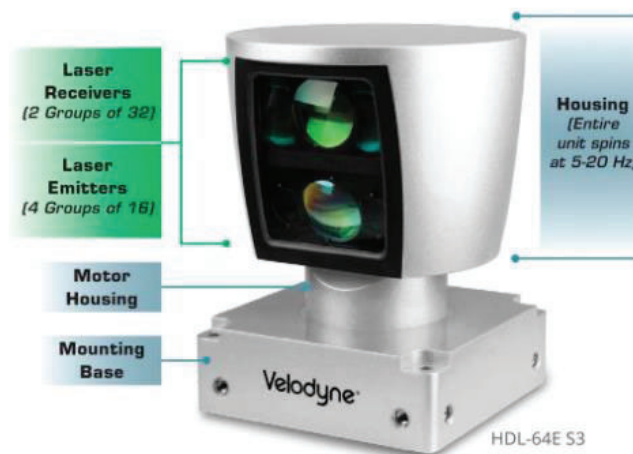


Figure 4 A diagram showing the mechanical structure of the Velodyne HDL-64E. Picture borrowed from a datasheet.

Range accuracy is stated as 2 cm in the datasheet for the lidar and the angular resolution as 0.4° vertically and $0.8^\circ - 0.35^\circ$ horizontally depending on the selected rotational rate. Measured reflectivity is reported as an 8-bit integer in the range 1-255. Timestamps are provided to each vertical slice measured by the lidar by a GNSS puck that is mounted on the roof of the vehicle to ensure satellite availability. The point cloud data, including 3D position of each point, transmitter index and reflectivity is streamed from the sensor's base to a converter box where the timestamps are injected from the GNSS receiver before transmitting the data via UDP over a RJ45 100Mbit ethernet connection to a computer or logger.

The VLP-32C is a time-of-flight rotating lidar sensor with 32 elevation layers of 360 azimuth degrees field of view, see the user manual [30]. It's a class 1 laser product working in 903 nm wavelength. The main interface is UDP/IP over Ethernet. It is possible to attach a GPS or INS over a serial port. The sensor's setting is accessed over a web interface, and as an alternative curl can be used to interact with the sensor. It is possible to configure the sensor to yield the strongest or last return (or both) from all lasers. This is useful when trying to identify objects or disturbances that are sparse, for example trees tops or snowfall. Diffuse reflections give values from 0 to 100% whereas retroreflectors can report values up to 255. It is possible to synchronize multiple sensors to avoid interference.

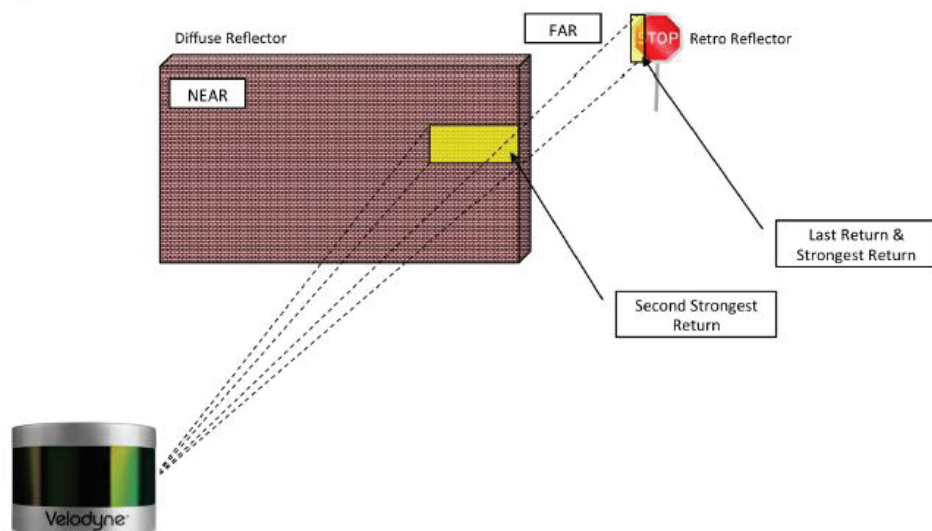


Figure 5 When one ray hits two objects, a near and a far, this can be recorded as two hits, which is useful in some cases. The picture is borrowed from the Velodyne's user manual.

The rotation speed can be chosen between 600 and 1200 rpm, but the firing time of one sensor is fixed to 55 μ s, which for example gives a horizontal resolution is 1,7mrad at the max rotational speed of 600 rpm. The scanning pattern is spread out horizontally in "four columns". The resolution in elevation angle is given by the fixed angles of the 32 layers, where the middle layers are more densely collected with an elevation difference of 5.8

mrad; with increasing angular separation up as well as down. The horizontal beam divergence is 3 mrad and the vertical beam divergence is 1.5 mrad.

6.2.2.3 Ti radar AWR1843

In the previous project HiFi Radar target a commercial off the shelf radar was used. Simplified, it can be said to report a list of object detections or targets, but how those detections are calculated remains a black box. In a normal traffic situation this should not be a problem, but as we are interested in characterizing the targets at a more detailed level, it would be advantageous to have access to the data before it is processed into a list of detections. For this reason, and since we have no real-time requirements on data analysis, the project decided to use an automotive radar development kit from Texas Instruments [21]. With this kit it is possible to device our own detection algorithms and with the right hardware it is also possible to collect raw data. The raw data can be used for analysis of noise characterization, testing of algorithms etc. In the project application it is stated that the project should aim to provide input to standardization of methods for characterization of targets. As such it is likely a good idea to look at possible ways to compare the results with the existing methods. In the currently available methods, radars with access only to higher level data may be used. It should be possible to produce similar data from the low-level data of the radars used within the project, but with more transparency regarding how to reach that higher level data. Methods directly using lower-level data could be developed.

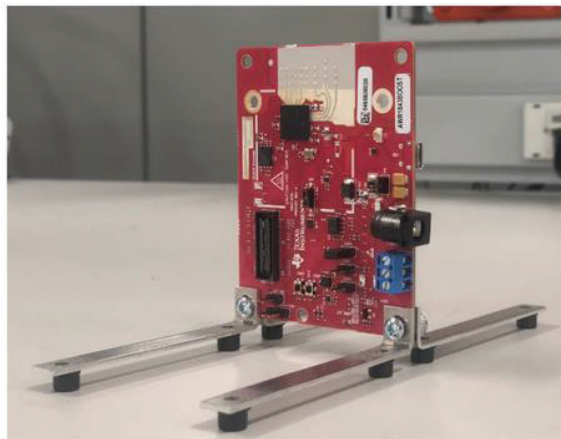


Figure 6 TI AWR 1843BOOST radar development kit with built in antenna arrays visible at the top centre of the card.

In the project the automotive radar kit from Texas Instruments, TI AWR1843, is selected. Together with a data access card, DCA1000, this system is able to provide low level data over Ethernet. The radars are of FMCW type and operates in the 76-81 GHz frequency range with 4 GHz available bandwidth. The built-in antenna array also provides the possibility to determine some angular information.

1. Interface the DCA1000 board with the xWR mmWave sensor EVMs, as shown in Figure 1.

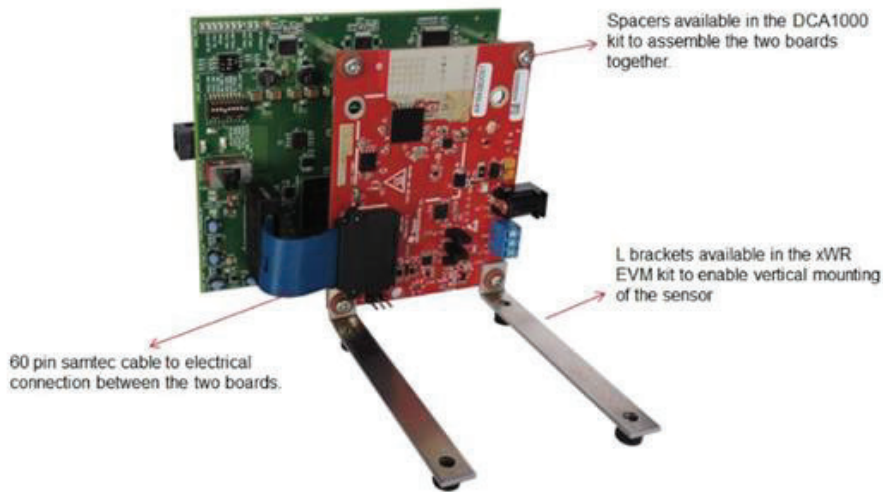


Figure 1. Hardware Connection: DCA1000 With xWR mmWave Sensor EVMs

Figure 7 DCA1000EVM card (green colour) mounted together with a TI radar development card. Picture from the user manual.

We have chosen to sample the frequency region 76.15-77.946 GHz with 512 samples per chirp and a frequency slope of 37.5 THz/s. This gives us a maximum unambiguous range of ~43.17m and a range resolution of ~8.43 cm. To be able to separate scatterers located closer, in terms of range from the sensor, they need to be separated by either velocity or angular position.

The chirp sequence is repeated 32 times consecutively yielding the possibility to separate scatterers based on their radial velocity, relative to the sensor, due to small changes in their phase over time. As we are mostly dealing with either stationary targets or targets moving at very low radial velocities relative to the sensor, the repeated chirps are mainly used for noise reduction. It is however theoretically possible to separate targets with a difference in radial velocity, relative to the sensor, of ~0.245 m/s and the maximum unambiguous relative velocity would be ~7.85 m/s.

The built in Rx antenna array has four elements for which the corresponding signal can be recorded in parallel. For improved azimuth angular resolution, a MIMO scheme is implemented utilizing the different Tx elements. It was decided to limit the project to analysis in the azimuth plane, and for this reason only two of the three available Tx antennas are used. A Time Division Multiplexing (TDM) MIMO scheme is applied producing a virtual array of $4R_x * 2T_x = 8$ elements. Our main angular region of interest is most likely around the center of the field of view of the radar. In this region we can, with the achieved virtual antenna, resolve scatterers which are in the same range and doppler bins, but separated by more than $\sim 14.3^\circ$. If closer than this, they will appear as one if using a simple FFT. The location of the maximum in the azimuth may still be decided with higher precision.

With the DCA1000EVM we can record the intermediate frequency signal at the four Rx chains. This should correspond to the amplitude of the return. The recorded value needs to be related to the actual reflectivity of the targets. This will be done by recording the return related to some objects with well-known RCS. For this we have chosen to use corner reflectors with known RCS. Furthermore, for the calibration the corner reflectors and sensors are to be placed far enough from the ground to be able to separate the signal, taking the direct path between sensor-object-sensor, from the signal taking the indirect way via ground. In this project it is assumed that the calibration curves for amplitude, range, and azimuth are linearly independent so that they can be assessed separately and written as $C(A,r,\theta) = C1(A)*C2(r)*C3(\theta)$

To protect the sensors from the environment at the outdoor test site, a radome has been designed and manufactured by Veoneer. Even though care has been taken in the design process to try to avoid it from affecting the signal, there is still a risk that it will. All the measurements, including the calibration and characterization of the sensors, should thus be performed with the radars mounted in their radomes for consistency. The possible effects of the radome on e.g. angle estimation is likely largest towards the edges of the field of view, and it is recommended that the targets are kept as close to the center of the field of view as possible during most measurements.

6.2.3 Supporting measurements

6.2.3.1 Scanning of targets and equipment

Targets have been 3D scanned in high resolution. Scanned geometry is both an input to building simulation models in PROSIVIC, but also for validation of targets, as for example in Figure 11. The rig from RISE mounted on a car has also been scanned at multiple occasions to record its relative location.

6.2.3.2 Portable spectral measurement device

In addition to the direct measurements with lidar, a portable spectral reflectance measurement device (PSRM) has been further developed. The basis is the device developed in the previous HiFi Visual Target project 2018. For the current project, the wavelength range was expanded to include 1550 nm which is used by some lidars. The PSRM is based on two spectrometers, one VIS-NIR which operates in the wavelength 350 – 1100 nm and one NIR which operates in the range 900 – 1700 nm. The combined range is thus 350 – 1700 nm, which covers both dominating wavelengths for lidars today (905 nm and 1550 nm). The main components in the PSRM purchased from OceanInsight (formerly Ocean Optics) are listed in Table 1

Component	Type	Note
VIS-NIR spectrometer	FX-VIS-NIR-ES	350 – 1100 nm 2048-element Si
NIR spectrometer	NQ512	900 – 1700 nm 512-element InGaAs
Light source	HL-2000-LL	Tungsten Halogen 360 – 2400 nm
Optical fibers	QP1000-5-VIS-BX 1000- μ m diameter for light source QP400-5-VIS-BX 400- μ m diameter for collection of reflected light	Length 1 m inside the box and 5 m outside, to probes. The outside fibers are protected by a stainless-steel sleeve.
Reflection probe 45-deg	Bifurcated fiber Probe holder RPH-1 45° and 90°	The probe is 6,35 mm in diameter and has six illumination fibers surrounding one collection fiber.
Integrating sphere	ISP-50-8-R	50-mm diameter Measures with 8-mm diameter port at 8° angle-of-incidence. Specular reflection may be included or discriminated.
Computer	RISE Laptop	Runs the spectrometer software and saves spectra on local hard disk
Battery	Power bank, 2 pcs @ 26000 mAh	Provides 12-V voltage, hot-swap interchangeable
Remote operation	Apple iPad	Controls the computer via TeamViewer. Allows the box to be closed (weather-proof) during measurements
Software	OceanView	Supplied with the spectrometers

The operation of the PSRM is in brief:

- Determine the spectrometer setup, choose the desired probe and fibers
- Calibrate the setup using first the lit light source and a white tablet (100-% level) and then light source off and a black surface (0-% level)
- Perform measurement of reflectance in selected points on the target

Figure 8 shows a schematic of the components.

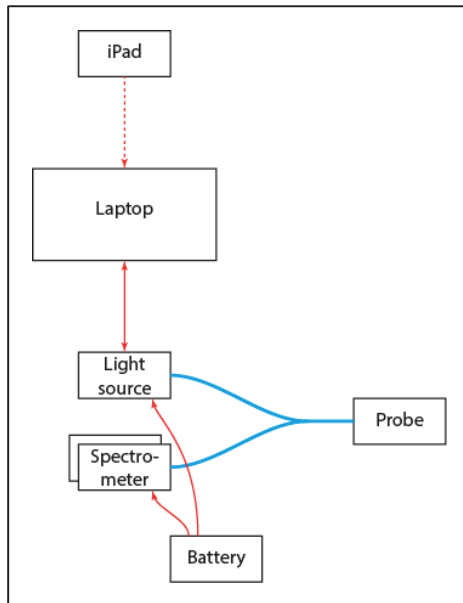


Figure 8. Diagram of the portable spectral reflectance measurement device (PSRM).

Figure 9 shows the PSRM, encased in a PeliCase with wheels for easy transportation.



Figure 9. The assembled portable spectral reflectance measurement device. Blue cables are optical fibers connected to the spectrometers and light source. These are accessible from outside the box via a panel in the lower part of the image.

6.2.4 Target objects

6.2.4.1 Real targets

Besides the real targets below, two-wheeled vehicles can be complemented by a real driver or possibly a soft driver.

Type of target	Info	
Tyre	Dimension: 225/45R17	Summer tyre without a rim
Yamaha MC	Yamaha XJ600, model year 1997	
Suzuki MC	Suzuki RF600R	
Fiesta	Ford Fiesta year 2011, white	
Electrical kick-bike	SoFlow S06 [26]	
Bicycle	Steel frame, 27/28 inch wheels	
Cabriolet	BMW 1-series 2011, metallic	

6.2.4.2 Soft targets

Soft targets are surrogates for hard targets which cause less damage when hit on the test track.

Type of soft target	Manufacturer and Version	
---------------------	--------------------------	--

Adult dummy (EPTa)	4a [22], Version 4	
Child dummy (EPTc)	4a [22], Version 3	
Bicyclist dummy (EBT)	4a [22], Version 5	
DRI-target (GVT)	DRI [24], Hatchback Rev E, upgraded to F* 21w44	
DRI-target (GVT)	DRI [24], Hatchback Rev G	Similar visual as above
MC-dummy	4a [22], "Euro NCAP 2023"	
Electrical kick-bike	AstaZero's design of soft version kick-bike based on SoFlow S06 mention above	

Platforms support soft targets to stand upright but also to give a soft target a trajectory.

Target carrier	Manufacturer and Version	
Guided soft target, GST (for car soft target)	ABD [27], MKII	

Overrunnable robot platform, UFO	Humanetics, [25] UFO Pro	
LaunchPad (for VRU)	ABD, 50	

6.2.4.3 Calibration targets

Calibration targets are well-defined objects with the intention to analyze, and possibly adjust, some quality aspect of a measurement rig. The need for well-defined lidar targets to use at test track for calibration and sensor performance verification drove an investigation into what kind of targets could be accurate as well as being durable enough to withstand use on test track.

The requirements on this kind of reference target become more complicated when they should work for different types of automotive lidar systems that can have a variety of scanning methods and operate at different wavelengths. The most commonly used wavelengths are in the range 850 nm – 1550 nm so the target must produce a uniform reflectivity detection in that range. The size of the target is another requirement that is based on the type of lidar systems that will be used and the use case for such a reference target. The target must be able to give at least one detection at the upper limit of 300 m range that is considered. The beam size of the laser spot size at that distance can vary quite a bit between lidar systems but is generally in the range of 0.5 m – 2.0 m. A target size of at least 1 m is considered a minimum requirement.



Figure 10 The 50% Permaflect target used in the linear calibration method, mounted on a target carrier.

Traditional metal trihedral corner reflectors were considered an option but by testing corner reflectors intended as radar reference targets revealed limitations in measured reflectivity between lidar systems and as a function of range. Prism targets are good candidates as a reference target for lidar but cost and robustness on test tracks are limiting factors. A large prism could be replaced by multiple smaller ones. Reflectance standards have been made for calibrating devices such as spectrometers, but generally these are small pads made of brittle material that are not intended for use on test track. Labsphere is an industry leader for lidar reference targets, collaborating with most lidar suppliers on the market. Their material called Spectralon is a commonly used reflectance standard. In recent years, a more robust reflectance surface coating has been created by Labshpere called Permaflect, specifically designed for robust lidar performance in outdoor usage.

The project had access to a number of trihedral corner reflectors which have previously been calibrated at RISE in Borås. Calculated as well as measured RCS can be seen in Table 2. Their theoretical maximum RCS can be derived from the length L of the side:

$$\sigma_{\max} = \frac{4\pi L^4}{3\lambda^2}$$

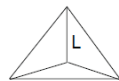


Table 2 Theoretical and measured RCS of trihedral corner reflectors available to the project

Theoretical RCS [dBm ²]	Measured RCS [dBm ²]	Difference theory- meas. [dB]
---	--	--

14.4	<i>Ref.*</i>	
-6.6	-6.5	0.1
4.0	4.9	0.9
9.4	10.2	0.8
14.4	14.5	0.1

Influence from the ground can be decreased or avoided by mounting the reflectors sufficiently high.

In the project we have had access to two copper spheres of different size, one larger with a radius of 38 cm and a smaller with radius 25 cm.



Figure 11 Large copper sphere close and smaller copper sphere in the distance. A selfie is inevitable when taking a picture of a reflecting sphere.

The spheres are electrically conductive, and the free space RCS is theoretically well defined as

$$\sigma = \pi r^2$$

where r is the radius. This assumes a perfect sphere, but unfortunately there are some visible dents in them and the stand, as well as the ground, will also have an influence on the radar signal. For calibration of radar's attenuation, a set of corner reflectors are more suitable.

We have investigated the shapes of copper spheres by 3D scanning and conclude that the variance compared to a perfect sphere is small in relation to its radius.

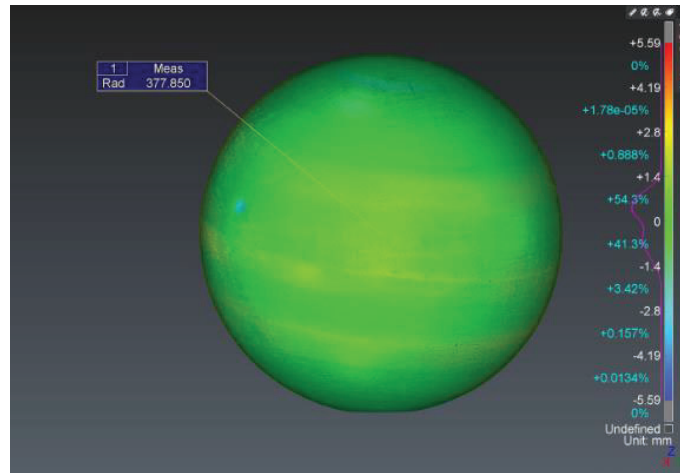


Figure 12 Deviation from a perfect sphere. The radius is about 378 mm with a variance of about 1 mm.

The drawback with a copper sphere on an outdoor test track is that they are rather fragile and also sensitive to moisture which slowly destroys its surface. As a complement to the copper spheres, we built a similar setup with a radar reflective pole inside and fibreglass sphere of 25 cm radius. The drawback here is that they are rather small compared to the capability of lidar at a long distance. The concept can be improved.



Figure 13 Plastic sphere and threaded on radar reflective pole.

By arranging multiple spheres these can be used to align lidar, radar and camera. It is a well-known problem how to find the centre of a sphere (where the radius is known) in a point cloud and the centre of it in an image. This can be compared to radar distance and angle.

6.2.5 Measurement platforms

Three different platforms were used at the test track. They partly shared the same class of sensors, auxiliary systems, type of logging strategies and post processing.

6.2.5.1 VCC

For the project, VCC has decided to use a test vehicle normally used for testing different prototyping solutions and therefore allowing a lot of flexibility in mounting location and orientation of sensors. Since VCC is not participating in the radar measurements planned in the project, the focus is put on the lidar sensors and an INS (inertial navigation system) to ensure that the lidar data can be used for the required analysis. The INS reference system used is OXTS RT3000 that is also being used to control the driving robot. On top of the 3 accelerometers and 3 angular rate sensors, the RT3000 has a GNSS antenna that is corrected in real time using a radio connection to a base station [20].

The main test vehicle used in the measurement campaigns is a Volvo V90 with a modular roof rack that allows for mounting of different lidars at a variety of locations and angles. The default sensor set used on the car is a forward looking Luminar Hydra mounted on the front of the roof rack, two side looking Luminar Hydra lidars facing left and right and a Velodyne HDL-64 S3 that is mounted on the top of the roof rack's center. A reference camera is mounted in the windshield of the car, it is only used for viewing the scene and understanding the lidar data, not for analysis. A photo of the test vehicle that was captured during the first measurement campaign at AstaZero proving grounds can be seen in Figure 14.



Figure 14 A photo of the V90 test vehicle used by VCC in the measurement campaigns

Logging and PTP time synchronization of the lidars is handled by a desktop Linux PC running Ubuntu 18.04. Time synchronization packages are forwarded via a AVB Ethernet switch from Motu. The Linux PC and the switch are powered by a 12V to 220V inverter and the inverter along with the rest of measurement equipment is powered by a relay box that runs from an auxiliary battery in the trunk with a control pad for the relays by the

passenger seat. A photo showing the measurement and logging equipment in the trunk of the car can be seen in Figure 15.

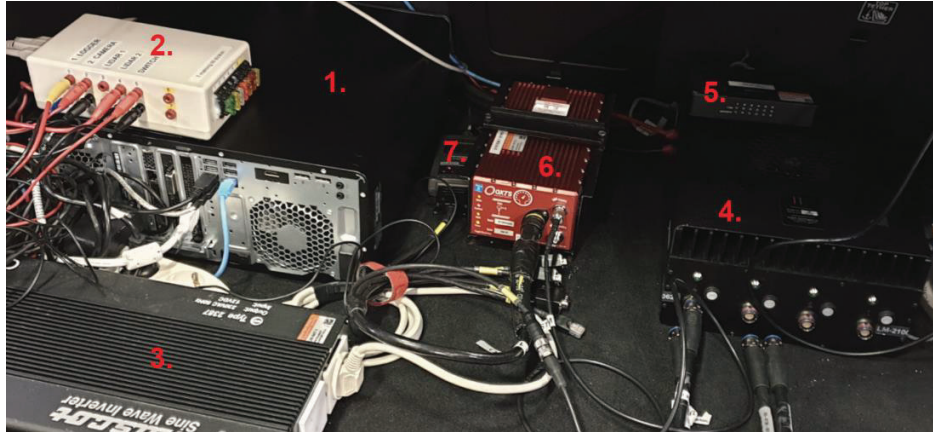


Figure 15 A photo of the measurement equipment in the trunk of the V90 test vehicle. 1. Linux logging PC, 2. Relay box, 3. 12V to 220V inverter, 4. Luminar electronic interface unit, 5. AVB Motu switch, 6. OXTS RT3000, 7. Basestation radio for real time corrections for the OXTS RT3000.

The Velodyne HDL-64 S3 has a vertical field of view of $+2.0^\circ$ to -24.9° (26.9° total) and a 360° horizontal field of view. The expected maximum range of the lidar is around 120 m and the selected frame rate set for the lidar was chosen as 10 Hz. The Luminar Hydra has an adjustable vertical field of view, allowing for distributing the vertical points across the usable vertical field of view of $+15.0^\circ$ to -15.0° (30° total). The expected maximum range of the lidar is around 250m. The distribution of points across the usable field is defined by a scanning pattern which can be defined as various mathematical functions. Along with the distribution of points it is possible to adjust the center of the used field of view (V_{center}) and how far down and up from the defined center the field of view stretches (V_{min} , V_{max}). Additionally, the center of the scan pattern distribution function (θ) and in the case of a gaussian scan pattern, the standard deviation of the gaussian (σ) can be defined. A diagram explaining the parameters defining the scan pattern can be seen in Figure 16.

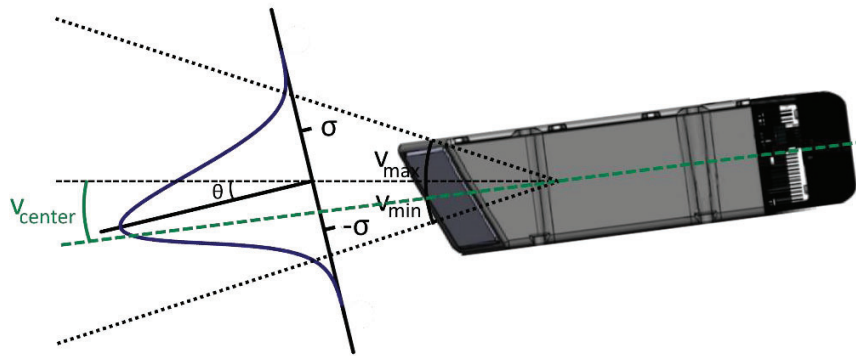


Figure 16 Definition of the vertical field of view for the Luminar Hydra. V_{center} is the center of the used field of view, V_{min} and V_{max} define how far down and up the field of view stretch from V_{center} respectively. θ is the center of the scan pattern distribution function and σ is the standard deviation to define a gaussian scan pattern.

For the measurement campaigns in the project, a gaussian scan pattern was selected with the parameters seen in Table 3. Both the Velodyne HDL-64 and the Luminar Hydra are set to capture point cloud data at a 10Hz framerate and the data is captured in a combined .pcap packet capture file using Wireshark. The Velodyne data is decoded using a built-in function in Matlab called *velodyneFileReader* and the Luminar data is decoded using a proprietary developed Matlab script based on the data packet format described by Luminar's documentation.

Table 3 The selected parameters defining the Luminar Hydra scan pattern that is used in the measurement campaigns.

V_{center}	0°
V_{min}	-15°
V_{max}	15°
θ	-1°
σ	3.5°

To be able to do accurate point cloud analysis, it is important to know the mounting locations and orientation of each lidar relevant to the test vehicle. Accurate estimations of the relative position and orientation are derived from a calibration measurement that is done at each measurement campaign to ensure that the locations have not changed due to vibrations or when a lidar must be dismounted. The calibration sequence for the forward looking lidars is done by a linear approach using the driving robot towards the 50% Lambertian reflectance targets. The target is placed stationary at the origin of the robot's coordinate system and the driving robot is set on a path from $X = 300$ m to $X = 3$ m away along the Y axis. A bounding box is then placed around the target location in the robot's

coordinate system and the detections from the target are tracked over the measurement duration and the path of the detections from the target are used to determine the location and orientation offsets using the robot path as reference.

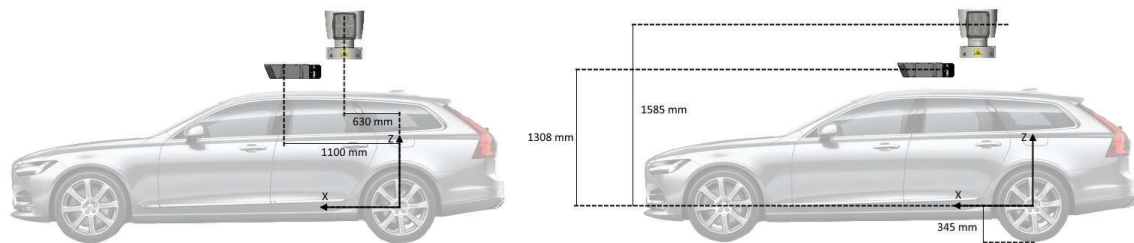


Figure 17 The mounting locations of the forward looking lidars relative to the center of the rear axle. Offsets in Z are seen on the left and offsets in X are seen on the right.

For the side mounted sensors, a similar procedure is followed but instead of the linear approach, a circular robot path with 25 m radius is followed around one of the spherical copper targets in the origin of the robot coordinate system. Since the forward-looking set of sensors is used for different test cases than the side looking set of sensors, the calibration is considered separate even though the Velodyne is in both the forward and side looking sets.



Figure 18 The mounting locations of the side looking lidars relative to the center of the rear axle. Offsets in Z are seen on the left and offsets in X are seen on the right.

The two different measurement scenarios, linear and spiral respectively, use a subset of the sensors on the roof-rack, the linear approach uses the forward looking Luminar Hydra and the Velodyne HDL-64 while the spiral path uses the left side looking Luminar Hydra along with the Velodyne HDL-64. For this reason, the calibration of the lidars is split into two and a calibration is run for each at every measurement campaign to ensure that the pose of the lidars is up to date in case of slight changes in the mounting.

The forward looking lidar set is calibrated by a 50% 1m x 1m Permafect target mounted on a target carrier. The target is filtered over the measurement and using the detections gather over the measurement log compared to the robot path, the mounting location and pose of each lidar can be inferred. The side looking calibration method uses one of the

spherical copper targets placed at the origin of the coordinate system with a circular path of 25 m radius around the target. The mounting location and pose of the lidars is inferred using the same method as the forward looking lidars.

6.2.5.2 Veoneer

Veoneer has developed an automated measurement rig with the goal to enhance the process of scanning and collecting data from radar and lidar sensors. The measurement rig is a self-driving robot based on a RC-car that pulls a trolley, see Figure 19. The RC-car runs by following specified drive files. By utilizing GNSS with RTK and IMU-sensor it can run in specified motion patterns with centimetre position accuracy and within 1 km/h speed accuracy.

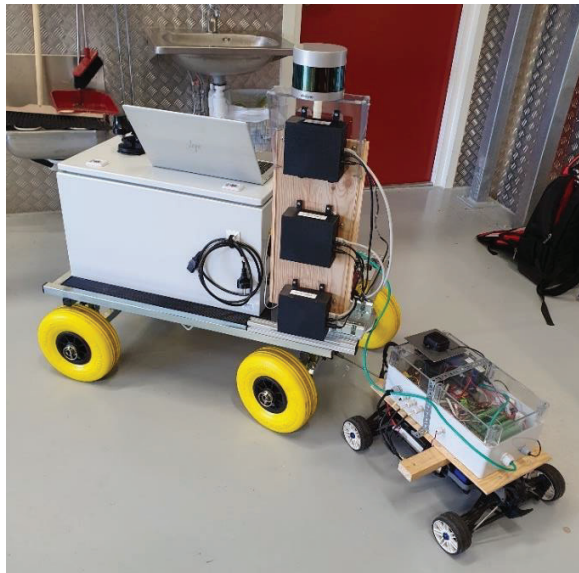


Figure 19 Automated measurement rig

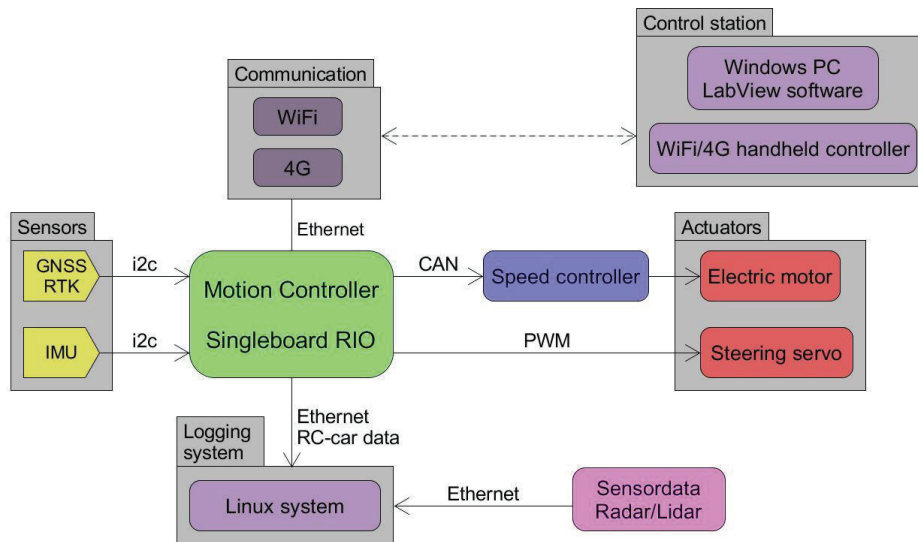


Figure 20 Overview of Veoneer's measurement system

The measurement system also contains a logging system that records the data from the sensors. Through a network switch the sensors are connected to the logging system and the RC-car. The diagram in Figure 20 shows an overview of the measurement system. Communication between the RC-car and the logging system is done through both WiFi and 4G-connection. A specifically developed user interface is based on LabView for creating drive files, for monitoring performance and to control the RC-car when conducting measurements.

The radar sensors TI AWR1843 and the lidar sensor Velodyne VLP 32C are used in the data collection campaigns. The setup with three radars of the same type but on different heights 47 cm, 67 cm, and 87 cm above ground. The lidar sensor is mounted on the top of the sensor setup at a height of 103 cm above ground. The sensors are mounted on a pole that can be rotated, for the radars to be able to measure on the side as well as straight ahead. Pictures in Figure 21 show the sensor setup and placement of the sensors measured from the position of the GPS-antenna as well as height above ground.

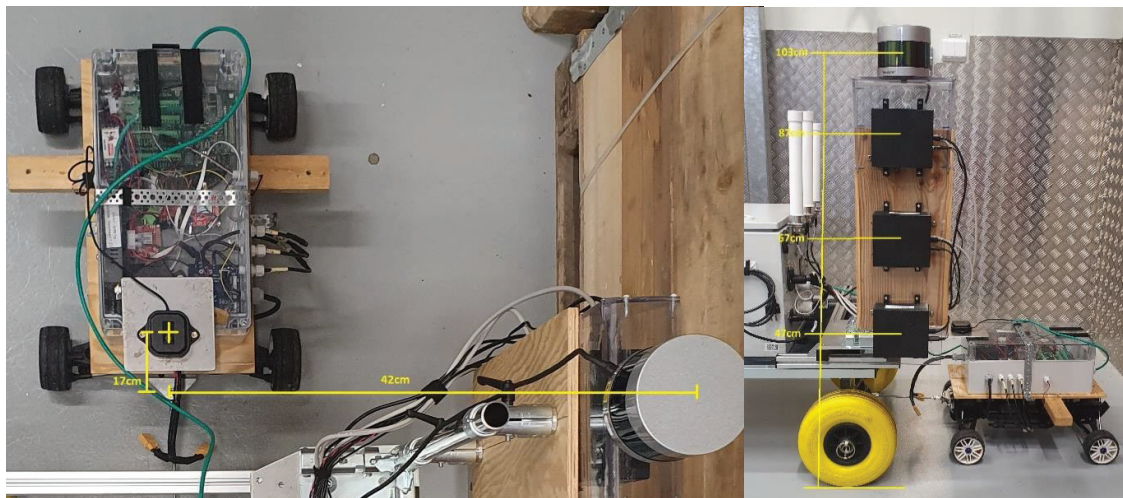


Figure 21 Placement of the lidar and radar sensors on the measurement rig

When running the logging program on the Linux system all the incoming packets are recorded with a timestamp for every packet. All recorded files are saved in the pcap file format. The files are then converted to the hdf5 file format using a python script. Data from the sensors in the RC-car is also recorded in the pcap file format and can be used to correlate with other sensor data. The data recorded from the RC-car contains position, speed and heading information from the GPS, accelerometer- and gyroscope data from the IMU.

6.2.5.3 RISE

The rig from RISE is based on two sensor brackets of aluminium designed to be mounted to a robot car. The idea is to mount the rig on a robot car from AstaZero which can be programmed to follow a specific trajectory. For linear approach to an object the sensors are mounted at the front, and for circular motion around an object e.g. with constant radius, the sensors are mounted on the side. The primary side mounting position of the vertical aluminium bar is outside the rear axle since it simplifies coordinate transformations when encircling a target. The front mounting frame consists of another set of aluminium rods and sensors can be mounted on any height on its vertical bar. The car provides a stable motion platform for low and medium speed. The robot car has a GNSS positioning instrumentation for driving in predetermined trajectories is needed when the measurement task does not require a moving base.

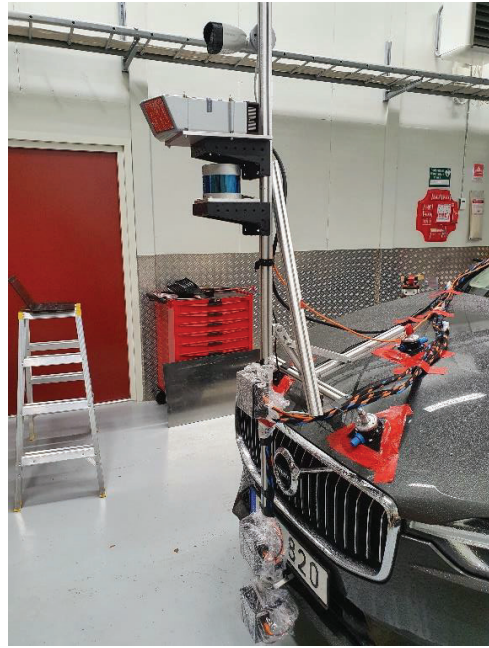


Figure 22 The figures show a camera for annotating recording, two lidars and three radars mounted on the front of a robot vehicle

Figure 22 shows a side mount and front view. The three radars are placed low above each other and are temporarily covered in plastic for rain protection. The lidars are placed at roof height. A web camera at the top of the bar is added to help remember details in the scene for later analysis. An advantage with this rig setup is the flexibility repositioning sensors. A drawback is that the exact positioning and orientation of sensors relative the car's coordinate system is likely to change inadvertently from one mounting time to another. The spherical reference targets were developed to enable post logging alignment of data. A logging session always include those targets for calibration.

Figure 23 shows the box containing the power supply, logger computer and other electronics. The system setup is sketch in Figure 24. Central to the data management in the rig is the logger, which is an industrial grade box PC running a Linux operating system. The high bandwidth data communication from sensors to the logger goes via separate gigabyte Ethernet ports. The logger provides NTP and PTP for time synchronization. The main communication channel is Ethernet, and for the GPS receiver and for synchronization of the radars, serial communication is used. The motion and position data from the robot car is logged over Ethernet.



Figure 23 The figure shows box with battery power supply, fuses, converters, switches and a computer for logging that is accessed via a laptop. Orange cables are for Ethernet. Blue cables are for serial communication to the radars.

The logger is accessed remotely with only soft real-time requirements both to parameterize and control some of the sensors but also to start and stop logging to its attached hard drives.

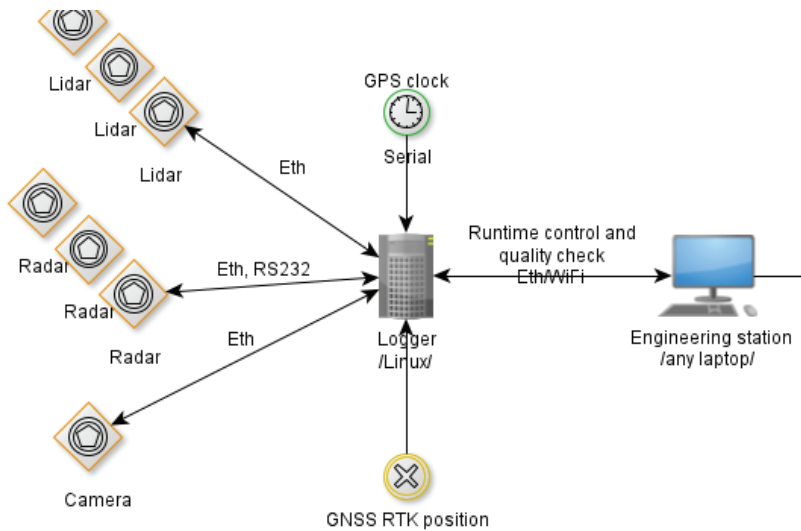


Figure 24 The Linux based logger is controlled from an engineering station

The sensors used in the RISE rig are: VLD32C, Hydra, three TI AWR1843 radars and an ordinary outdoor web camera. The purpose of the camera is to verify in the postprocessing what has been logged; no analysis based on the image data was planned. Selection and exact mounting position/orientation of the sensors depend on the aim of the

current measurement and can vary from one measurement session to the next. The motion of the robot car is recorded by a GNSS RTK positioning device integrated with an IMU from Oxford Technical Solutions [20]. It is placed in the trunk close to the rear axle and the centre line of the vehicle. In order to avoid interference between the three radars, the triggering of frames for each individual radar is done in sequence. Large effort has been devoted to the design and implementation of the real-time sequential cyclic activation of the radars. The compiled program RadarCommander was developed in the project for this purpose. From this program, the radars are discovered, configured and operated.

The engineering station is the primary way to access the logger remotely to perform calibration, start and stop logging and to perform a quick verification of the acquired log data. The engineering station is an ordinary laptop from which we can do SSH and RDP with the logger for script control and supervision and settings of the sensors. The logging scripts also invoke control of the TI radars and the camera.

The GPS based clock is connected via an Ethernet port or via serial communication to supply NMEA sentences and PPS. The system time of the logger is adjusted using NTP based on the GPS clock listening also to the PPS signal. From the logger, time is distributed to the sensors capable of receiving clock updates over Ethernet. There is also a possibility to distribute time over the serial interface to multiple receivers. The time accuracy needed in the experiments is < 1 ms, to account for low and medium speed of sensor platform or target. The Hydra has an implementation for PTP instead of NTP. PTP makes sense to use for an embedded system. A main difference between these two protocols of distribute time is how the global time “the correct time” is determined. Resolution and accuracy are comparable.

The power supply in the box is two 12V lead batteries. One of the lidar sensors is supplied by 12V whereas the other sensors and auxiliary equipment runs on 5V. The other lidar sensor has 24V supply, for which we use another 12V battery in series. Converters from 12 to 5V as well as a 240V battery charger to 12V have been installed in the grey box in Figure 23.

The rig needs to be calibrated to verify that sensors are positioned and oriented as intended to achieve repeatability between two measurement sessions. Sensors of different modalities must refer to one object as being located at the same world fixed coordinates or rig fixed coordinates. Also, sensor coordinates do change over time, because of unmounting and remounting sensors on the aluminium profiles. It is good practice to verify calibration each time the rig position or sensor positions are changed. The calibration procedure, to verify alignment of sensors and repeatability over time and to enable adjustment of sensors, is to measure against well-known objects, in this case the copper spheres. The calibration result is used when unpacking the logged data and storing it in the HDF format ready for analysis.

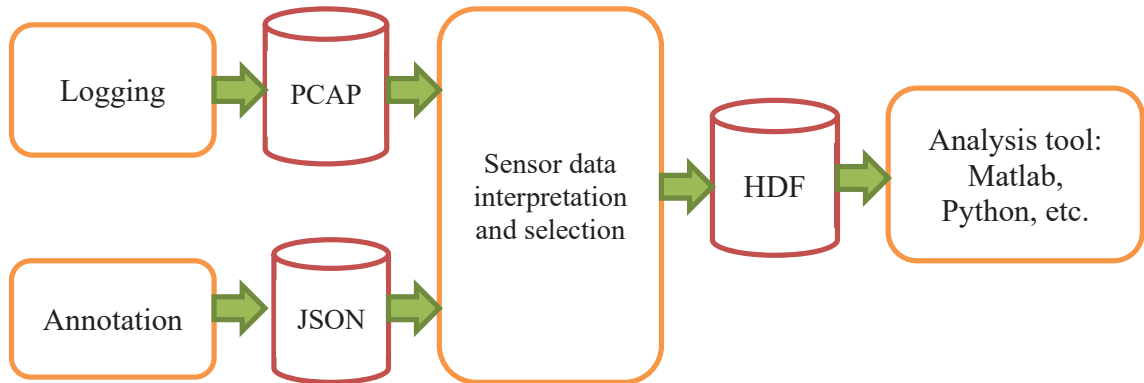


Figure 25 Tool chain from logging to start of analysis

The software logging is based on the open-source software libpcap (akin to Wireshark) for Linux and complemented by scripts for handling the logs. The logging is a recording of the communication devices with timestamp from both the logger and possibly all the sensors, and no processing of its contents is done until logging has stopped. The tool chain to get data ready for analysis starts with recording PCAP files. In parallel to logging, an annotation file for each logging session is written manually from a template. The annotation file guides the conversion and provides information useful for a later filtering and analysis of the data. The next step, see Figure 25, is to interpret the sensor data from UDP packets to time series, frames, scans and images. The converted data is augmented with the annotation and saved to a file format called HDF, hierarchical data format [28]. The tool chain can be used while on the test track to make a first check of the collected data. The radar control program RadarCommander and large parts of the tool chain are also used in Veoneer's platform.

The HDF is suitable for big data and also allows for use of meta data and with an additional explanation of variables that should be all that is needed to interpret the data log properly. A combination of Python scripts and c/c++ compiled sensor interpreters have been assembled into this tool chain to fill the HDF files with data and annotation. Many common analysis tools such as Matlab or Python have interpreters for HDF. The HDF format also allows for compression of individual variables, which could prove handy considering the potential large amount of data. The format has been used by for example the L3pilot project [19]. Selected logging data from the RISE platform was shared across the partners of the project.

6.3 Simulation models and results

6.3.1 Lidar simulation

The major objective of the simulations is to produce digital twins of sensors and targets. To achieve this the following steps were planned and executed:

- First analyze the lidar point cloud from the experimental data.
- Second, we extract the relevant parameters that affect lidar data such as variation of cloud point density and material reflectivity.
- Third, we first simulate the experiments without improving the lidar and target models and compare with experimental data.
- Finally, depending on the gap between simulation and experiment result, we adjust the numerical models of lidar and material properties to reduce the gap between the simulated and experimental data.

The lidar model in the simulation tool PROSIVIC [8] allows to simulate a typical lidar sensor used in automotive applications. It makes depth images of the environment of the sensor. The lidar Field of View (FOV) can go up to 360° in horizontal and up to 180° in vertical, and it supports multiple scan layers. Each scan layer corresponds to a given vertical angle, defined in spherical coordinates. This means that if the lidar is facing a vertical surface, all points of a layer are at the same height level. The lidar model considers laser physics propagation and covers a large part of the lidar data-sheet parameters such as: beam divergence, initial laser beam power, wavelength, detector surface area, and number of layers. The objects lighting by the lidar reflect totally or partially the laser energy. The collected laser intensity by the detector depends on the laser beam divergence, incidence and reflection angles, FOV of the detector. It also depends on the geometry, material composition, and the color of the objects under lidar FOV. The lidar model correctly estimates the material reflectivity and laser energy attenuation caused by weather effects such as fog, rain and the detector glare by sunlight.

Data from Velodyne's VLP32C and Luminar's Hydra have been taken from manuals and open sources.

6.3.2 Comparison experimental and simulated data

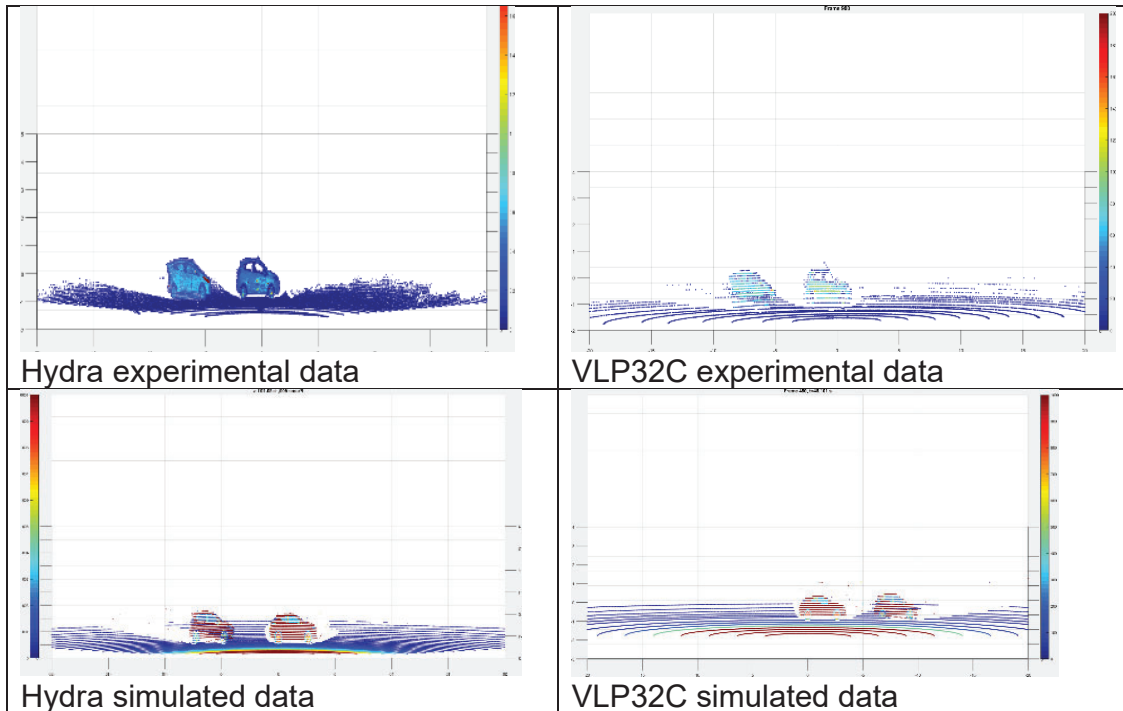


Figure 26 Hydra and VLP32C comparison real versus simulated data. Left car is a soft target, right car is a Ford Fiesta.

Both lidars Hydra and VLP32C detect the soft and real car with different intensity. We see in experimental data that the headlights and ID plates and car body are the most reflective while the windshield, lateral and rear windows are transparent for the two lidars. These observations are reproduced by virtual sensors in PROSIVIC. On the other hand, the detection of the soft car seems identical to real car except the windows which are detectable by the two sensors for the soft car.

6.3.3 Ideal and physics-based sensor model

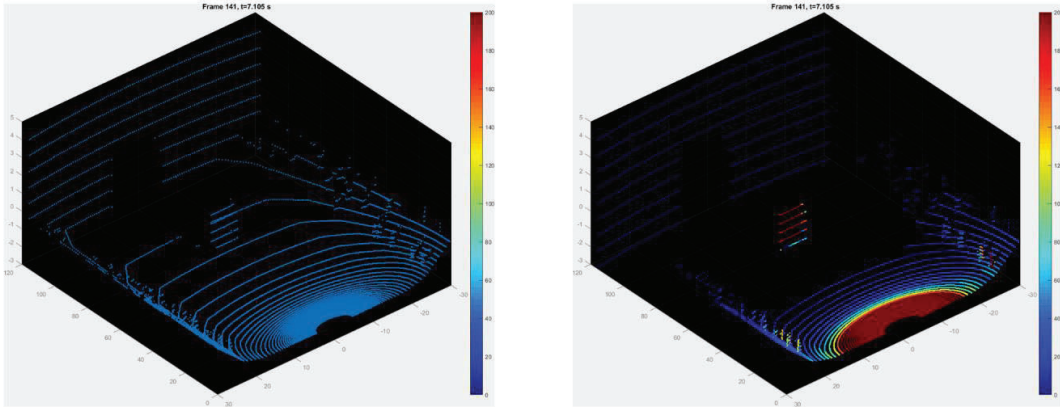


Figure 27 Simulation of truck detection by ideal sensor (left) and physics-based sensor (right).

Figure 27 shows the detection of truck by lidar. The left image corresponds to the simulation with Ideal sensor while the right image with physics-based sensor. Ideal sensor models are often described as sensor models without errors. They detect every object in their specific FOV without false positives or false negatives. Ideal models can also be used for producing ideal sensor raw data (radar data cubes, point clouds, and images). Physics-based sensor models describe the sensor based on physical and mathematical descriptions of the measuring principle and information processing. Physics-based models are the most detailed models.

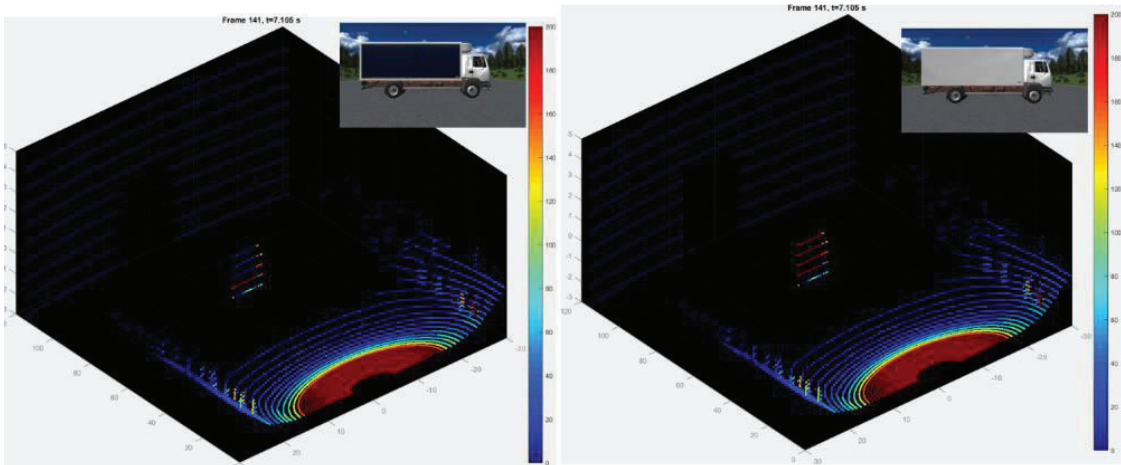


Figure 28 Reflectivity of tarpaulin and metal truck

From the lidar's perspective, the real-world traffic can be seen as a mixture of different objects which have their own geometry, a given incident angle and a specific surface material composition. An object of the scene – for example a truck from the side in Figure 28 – is composed by different materials: metal for body, plastic for bumper, glass

for windows, tarpaulin or metal for the container. The different materials of the truck will reflect the laser light with different intensities. It is then necessary to consider the laser-matter interaction in order to estimate the energy returned to the detector.

6.3.4 Simulation in rain and fog

Figure 29 and Figure 30 are simulation results in medium rain density (around 20 mm/h) and medium fog density (visibility a few hundred meters). The clear weather image is taken as reference. This image is used for comparison when the sensor is disturbed rain or fog.

We can see from all images that the moist air acts as a screen for the infrared radiation. Both fog and rain reduce laser intensity by absorption and diffusion phenomena of the laser beam by the small water droplets. Fog and rain act then as a screen on lidar sensors that limit their capabilities and detection range. It is important to consider the attenuation factor to adapt speed, braking distance and stability control systems accordingly.

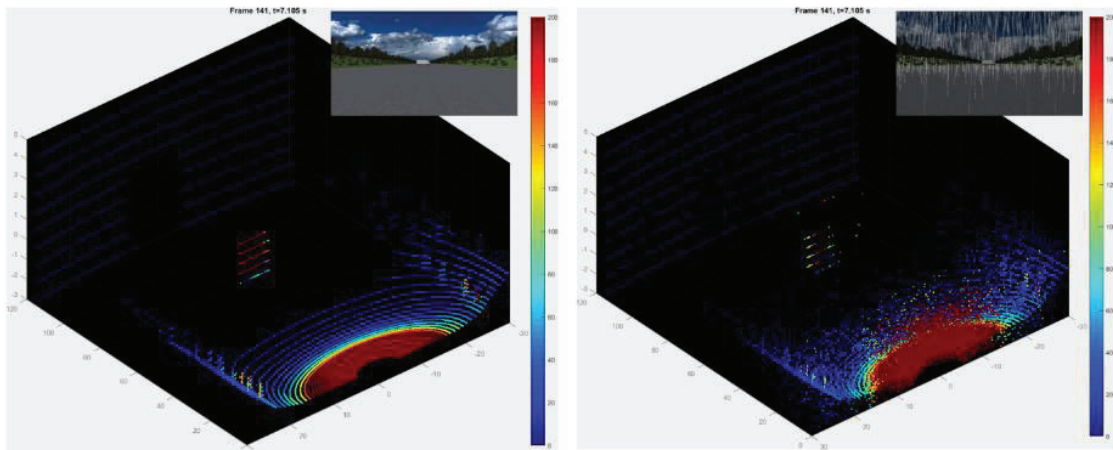


Figure 29 Simulation in clear weather (left) and medium rain (right)

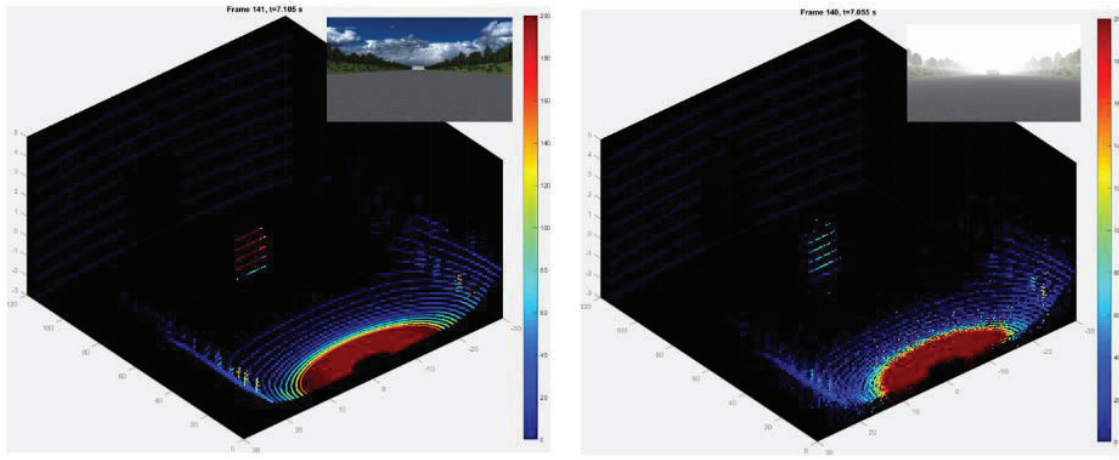


Figure 30 Simulation in clear weather (left) and medium fog density (right)

6.3.5 Radar hardware in the loop simulation

There is a need to test radar sensors under different scenarios and conditions and being able to reproduce the tests. In-lab radar testing clearly stimulates definable targets in a scenario. The radar targets can be simulated at different speeds, distances and sizes using Radar Target Simulator (RTS) technology which enables ADAS/ADS applications to be tested quickly, effectively and most accurately.

6.3.6 Radar HIL over the air system setup

The ASGARD1 system by UniqueSec creates target perception in terms of range, speed, and RCS for the radar under test (RUT) to evaluate its performance. With this setup, it is possible to generate targets with arbitrary range, speed, and number of targets for testing radars in different use cases.

According to the block diagram, the hardware components of ASGARD1 includes an RF front-end, a digital back-end, and a DAC (Digital to Analog Converter), see Figure 31. The digital back-end includes signal processing unit and DAC. In-phase (I) and Quadrature (Q) inputs to the RF front-end are provided by this module. The RF front-end component mixes I and Q signals generated by DAC adapter module with the received radar signal. The RUT should be placed in front of RF front-end at a distance of about 15 cm where the radar antenna is positioned in front of RF front-end antenna.

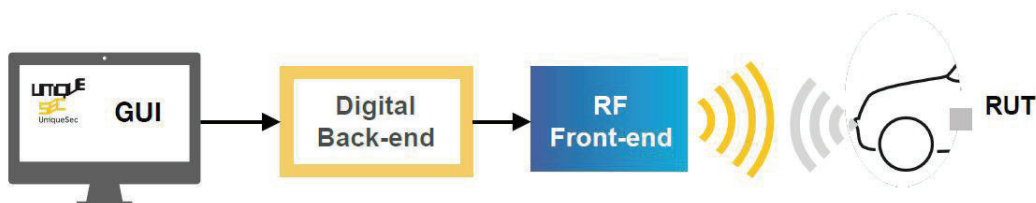


Figure 31 Block diagram of ASGARD1 hardware

The radar system is placed in front of ASGARD1's antenna and creates the perception of different targets. The digital back-end consists of signal processing and controlling unit which is generating the signals corresponding to the target information. The essential software is an FPGA-based program running over the digital back-end and controlled via a user interface running on a PC.

6.3.7 ASGARD1 and PROSIVIC integration

The radar model in PROSIVIC by ESI, simulates a radar sensor that can deliver information of distance, relative speed and angular position. It makes use of radar characterizations of objects according to their radar cross-sections (RCS), and evaluates the energy reaching and departing from objects in the propagation channel. The radar model represents the sensor system itself, including the antennas, the signal generation and the signal processing. Its output is a list of radar targets.

The ESI CEM One in the field of computational electromagnetics has been used for ADAS radar target characterization through RCS. The CEM One software offers all major simulation techniques in both time and frequency domains. Within the Visual-CEM user environment, various 3D methods are made available with the classical Finite Difference Time Domain (FDTD), with the Method of Moments optimized using the Fast Multipole technique (MLFMM), Finite Elements or Physical Optics for high frequency scattering problems. The geometry input is typically given in the form of faceted surfaces with different electromagnetic properties depending on the type of material, e.g., metal, rubber, glass etc. In the project, several objects have been scanned, see example of a bicyclist in Figure 32 computed by ESI CEM One.

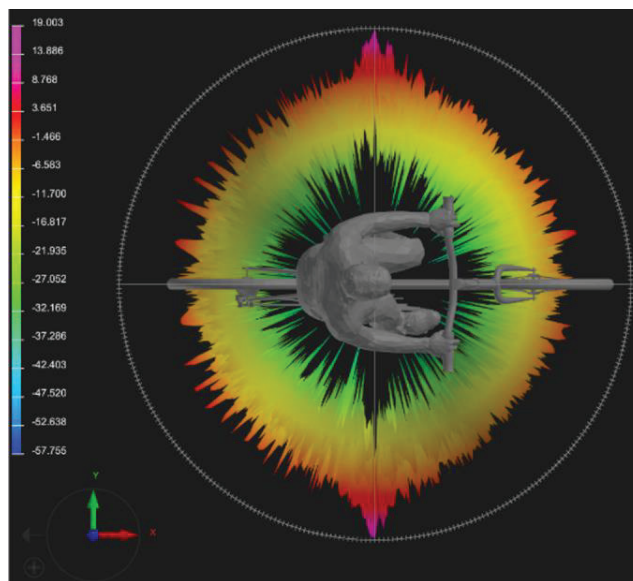


Figure 32 Bicyclists RCS at 77 GHz

The block diagram in Figure 33 shows how a driving scenario is generated in a typical vehicle simulator and our suggested API to ASGARD1. In this solution, first the vehicle simulator builds up a scenario, then the target information needs to be post processed based on radar detection properties and prepared to be sent. The post-processed radar targets are sent to a UDP server to encapsulate UDP messages and send them over Ethernet to a UDP client in ASGARD1 side. Basically, the post-processing of targets is very important to choose right targets located in radar's FOV and find the reflection points targets or point-scatterers. To do this processing, it needs to use radar model parameters used for the scenario. On the other side, every time the UDP client provides the information of targets to ASGARD1 system to verify the radar under test according to the generated scenario. The proposed API is a one-way communication from the vehicle simulator to ASGARD1. All simultaneous point targets in the radar's FOV should be included in the UDP packet.

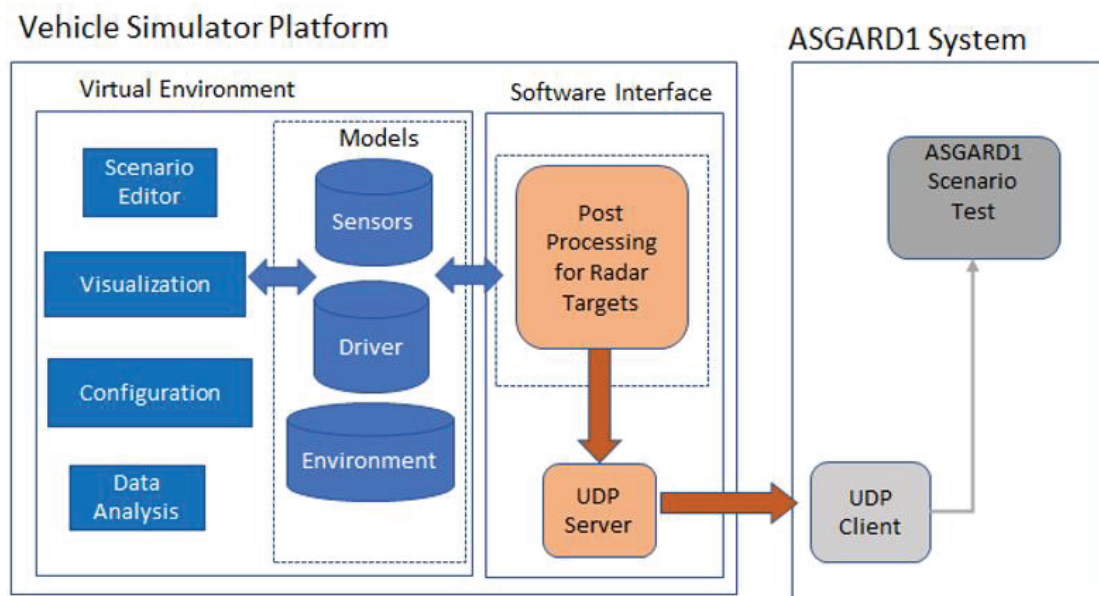


Figure 33 Block diagram of ASGARD1 with PROSIVIC.

6.3.8 Case study: Euro NCAP CPNC scenario

We have chosen the Euro NCAP CPNC scenario for demonstration of simulation. Details for running the test can be found in [7]. Car-to-pedestrian impacts are one of the most frequent accidents happening on the roads due to driver distraction or misjudgment. Typical accidents between cars and pedestrians occur at city speeds where the pedestrian crosses the path of the vehicle. These types of accidents with vulnerable road users usually coincide with severe injuries and leave the driver with very little reaction time to apply the brakes. The objective of the simulations is to show the parameters which can

influence the child detection by radar sensor, for example the ego-vehicle speed radar resolution and obstruction of the child by stationary cars.



Figure 34 CPNC-50 scenario, Running Child from Nearside from Obstruction vehicles in PROSIVIC software. A parked SUV closest to the observer (ego vehicle first view perspective). In front of the SUV a parked sedan. A child moves from right to left perpendicular to the parked cars along the road. When the child first starts to move it is typically completely obscured by the cars.

FMCW radars perform differently when they have been configured with different chirp parameters. The chirp length or chirp period, chirp slope and sweep bandwidth are some of important parameters for these radars. For the simulations we configure radar AWR1843 for these parameters for the expected performance. Figure 35 presents one of the scenarios with a specific radar profile (parameters) we ran through ASGARD1 and PROSIVIC, and it shows the real radar outputs after the simulation.

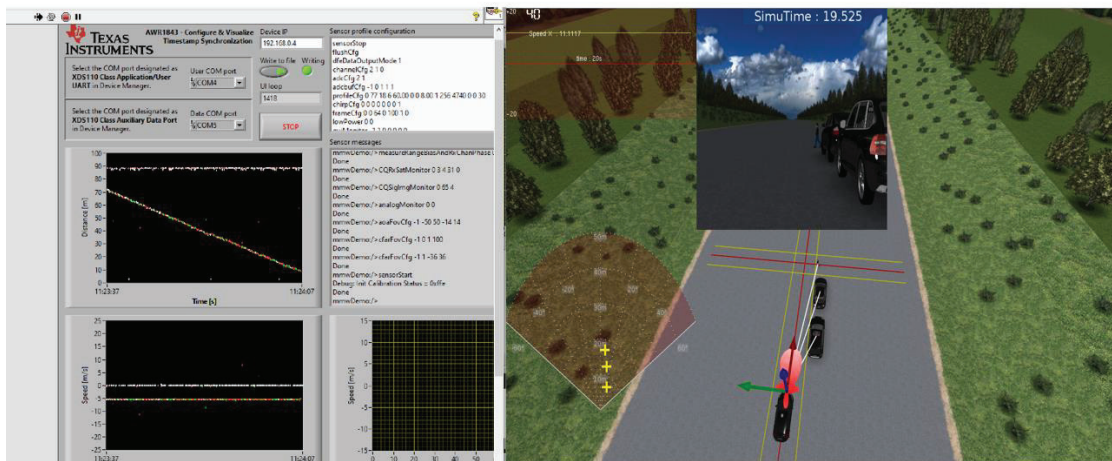


Figure 35 Radar simulation in HIL setup running ASGARD1 and PROSIVIC

We demonstrated and analyzed the results of radar simulation with CPNC scenario for different speeds of the ego vehicle. These test cases are clearly showing the effect of ego vehicle's speed and radar performance for detecting the child. The child can be detected

by the radar at lower speed, but when the speed is increasing it becomes more challenging for detect the child in the good time. At higher speed, the child either is occluded or partially confused by another target (the parked car) and therefore the radar is not capable of detecting the child.

The detection criteria are comparing the targets position obtained by real radar and radar level 1 with the ground truth data. The ground truth data from the simulator is provided through multiples distance observers between radar position and RCS position of SUV, Audi A4 and pedestrian child. The ground truth data are represented by blue curves in Figure 36.

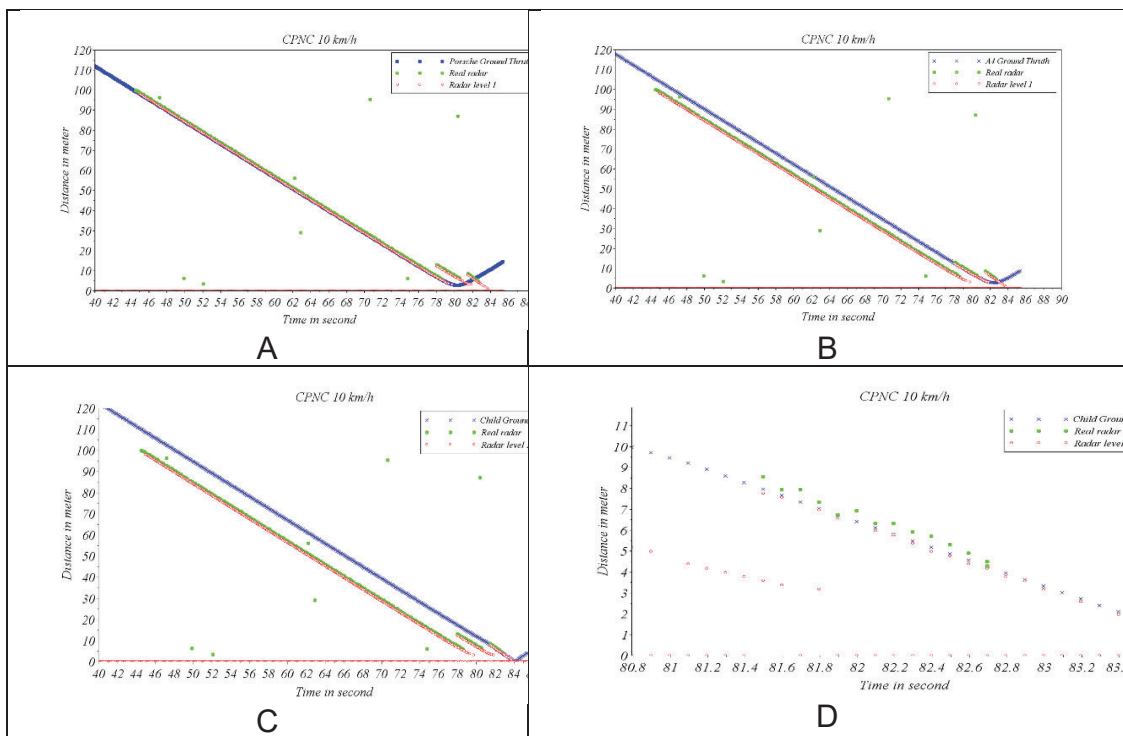


Figure 36 Measured distance in time. Ego vehicle speed 10 km/h. A) comparison with ground truth of SUV target. B) comparison with ground truth of the sedan car. C) comparison with ground truth of child target. D) Zoom of figure C. Blue curve: ground truth, green curve: real radar data, red curve: radar level 1 data

With the proposed radar HIL test, we can score different radars under the same conditions for a specific scenario or use case. These trustworthy tests can help OEMs to understand and judge confidently on different radar performance according to their safety requirements.

6.3.9 Theoretical study: water on objects

The topic in this subsection is lidar beam interaction in adverse weather conditions including rain, fog and wet targets. Scientific literature has been studied and used as a basis for development of a mathematical model and to create detailed simulation using Zemax OpticStudio [9] for a set of specific cases. The mathematical model presented in this report is based on radiometry; a generalized lidar equation has been derived. The model includes atmospheric conditions by numerical calculation of the Mie scattering coefficients from first principles by assuming log-normal particle size distribution. The bidirectional distribution function (BRDF) describes the reflective and absorption properties of the target. In the mathematical model the BRDF includes water film and water droplets on the target surface.

6.3.10 Mathematical model of lidar beam interaction

In this section we derive the lidar equation from first principles of radiometry. Radiometry is a discipline of optics that treats the flow of energy between spatial regions [11]. A typical question is: given a specific type of light source and a specific type of detector, how much optical power can be measured if the source and detector are, for example, 50 m apart and configured in a specific geometry?

Assume that the lidar (laser and sensor) is located at $z = 0$, the range is the distance to the target $r = z_{\text{target}} - z_{\text{lidar}}$ and θ is the tilt angle. The target will reflect a laser beam into a specular and a diffuse component. The lidar and the target is entirely immersed in an atmosphere that may contain scattering particles (e.g. rain, fog).

A distinguishing feature of a laser beam is its ability to be and stay shaped as a beam over long distances. In other words, the energy emitted by the laser will be identical to the energy that hits the target. Of course, this is only a valid assumption under ideal circumstances when there are no scattering particles in the propagation path. If the beam is diverging so that the beam spot is larger than the target a part of the energy will be lost. To include this the overlap function O_{LT} is included in the model. The reflection of the illuminated target is then a secondary light source and the detector collects a fraction of this energy. The reflectivity property of a material is described by the bidirectional reflectance distribution function (BRDF) which is defined as,

$$f_{\text{r}} = \frac{\text{reflected radiance}}{\text{irradiance}}.$$

The BRDF contains two vectors (therefore the name bidirectional) and is in general a complicated expression. Of the nine different types of reflection factors that can be calculated we are interested in the so-called biconical reflectance which basically is the outgoing reflection 'cone' as a function of the incoming illumination 'cone' [11]. In the classic lidar equation one assumes that the target is lambertian and thus only have a diffuse BRDF component. As a first generalization we assume that the BRDF can be

separated into a diffuse part and a specular part in a treatment similar to Steinvall [12]. This is the simplest non-trivial approach for treating specular and diffuse reflection, for a more general and complex approach see [13]. In the formalism that we use we make frequent reference to the projected solid angle,

$$\Omega_{a \rightarrow b} = \frac{A_b \cos \theta}{r^2}.$$

Hence, the projected solid angle is the two-dimensional angle that spans an area $A_b \cos \theta$ as seen from location a at a range r . In terms of the projected solid angle the lidar equation for a tilted target with diffuse and specular reflection is,

$$P_D = P_L O_{LT} \Omega_{T \rightarrow D} \left[\frac{R_d}{\pi} + \frac{R_s}{\Omega_s} \Pi_s \right].$$

Π_s is a distribution function with the property that it is one inside the scattering divergence angle and zero outside. It can be noted that the π in the denominator corresponds to the projected solid angle of the entire hemisphere. This is the first generalization of the classic lidar equation.

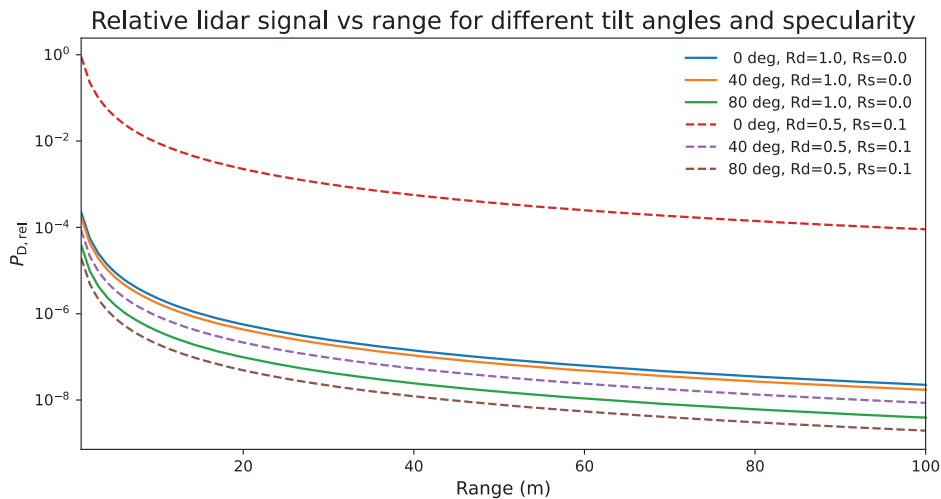


Figure 37 Detector signal as a function of range. Solid curves are for a perfectly reflecting diffuse target. The dashed curves show the detector signal for a target that has 50% diffuse reflection and 10% specular reflection. The specular component gives a signal that is orders of magnitude larger than the diffuse component.

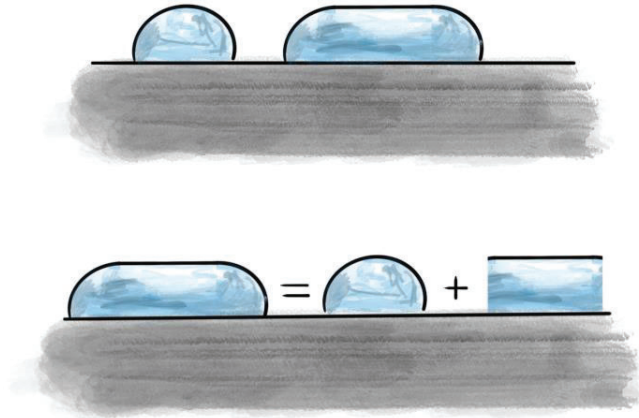


Figure 38 Water drops are considered to be perfectly spherical potentially with a flat central section. In the model the perfectly spherical droplet is treated separately to the flat 'film' part.

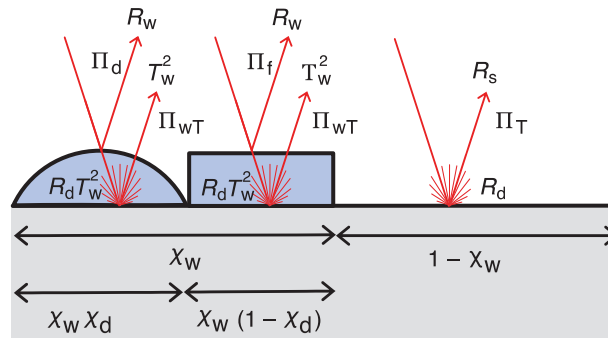


Figure 39: The wet target BRDF is composed of four distinct components. Here the specular and diffuse part of the dry target is shown together with wetting ratio and drop ratio for the specular and diffuse reflection of the water drop and the water film.

For a wet target the effective reflection will be affected, and it is necessary to generalize the classic lidar equation to predict the lidar performance. In addition to the dry target BRDF three BRDF components can be identified by studying Figure 39.

The wet target BRDF is

$$f_{wT} = \frac{R_{d,T}}{\pi} + \frac{R_{s,T}}{\Omega_{wT}} \Pi_{wT} + \frac{R_{s,f}}{\Omega_{sf}} \Pi_{sf} + \frac{R_{s,d}}{\Omega_{sd}} \Pi_{sd},$$

where the Π_k are distribution functions with the property of being one inside the scattering divergence angle and zero outside. The effective reflection coefficients are reported elsewhere. Having defined the BRDF it is straightforward to calculate the power in the detector. The generalized lidar equation form a wet target is,

$$P_D^{wT} = P_L \Omega_{T \rightarrow D} O_{LT} f_{wT}.$$

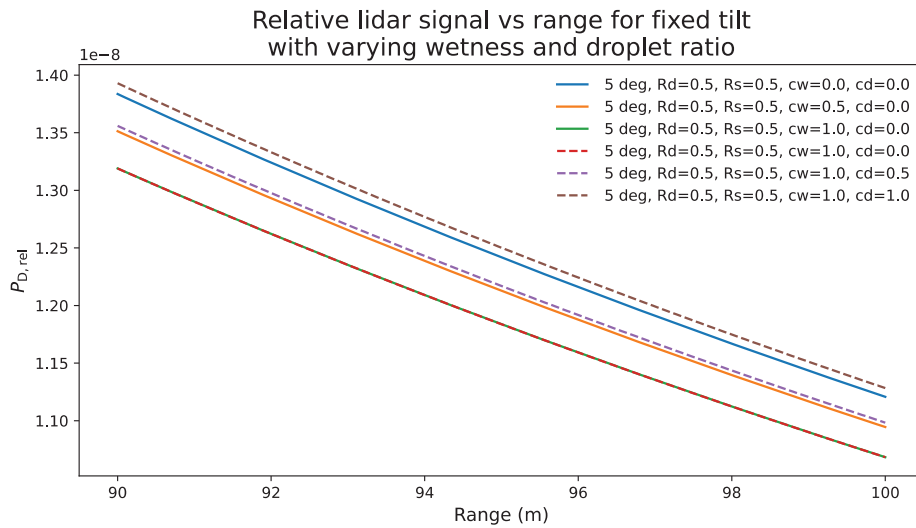


Figure 40 At a fixed tilt angle of 5 deg the detector sees the diffuse reflection from the dry target and from under the water film. If the water film ratio is increased there will be a power drop of approximately 5%. If the part of the water that are water drops is increased, the resulting detector signal will be increased due to the specular part of the drops.

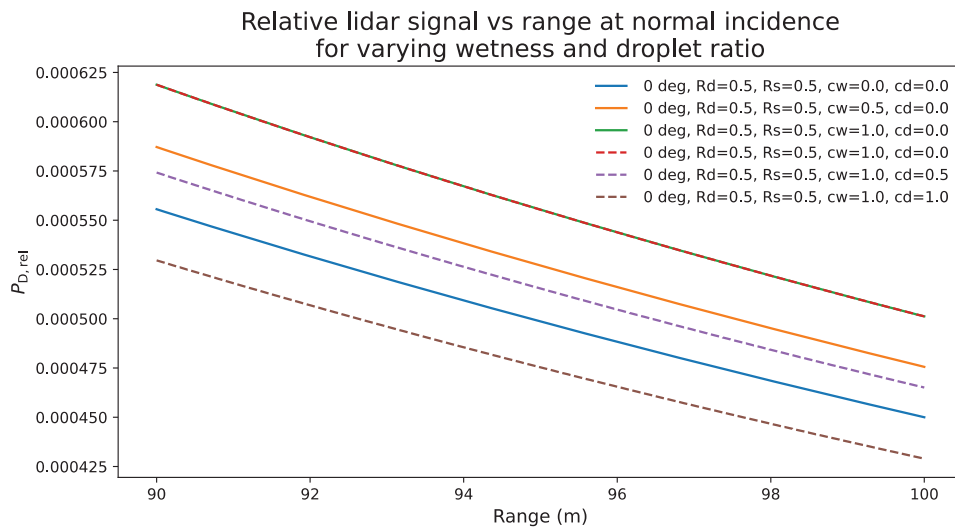


Figure 41 At normal incidence we seen that increasing the water film ratio yields a power increase of approximately 10%. If the water droplet ration is increased the power will be decreased. The later shows that water droplets are effective scatterers of the lidar beam.

When a lidar beam propagates through rain or fog the useful lidar signal will be attenuated. Assuming the atmosphere to be continuous the attenuation is given by the Beer-Lambert law and the resulting lidar equation is given by,

$$P_D^{WT} = P_L \Omega_{T \rightarrow D} O_{LT} f_{WT} e^{-2\gamma_{ext} r},$$

where γ_{ext} is the extinction coefficient and is calculated using Mie scattering theory. This is the generalized lidar equation for wet targets in an attenuating atmosphere.

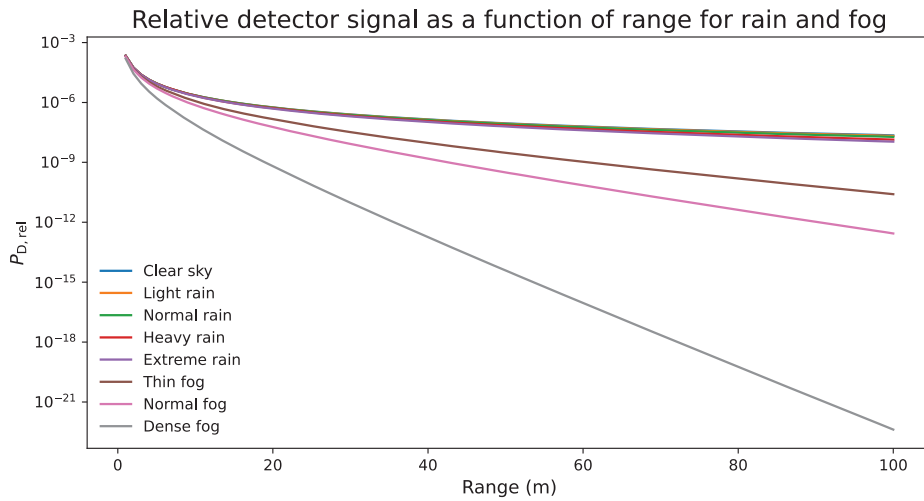


Figure 42 Plot of the relative lidar signal as a function of range for rain and fog. Fog is decreasing the lidar signal much more than rain.

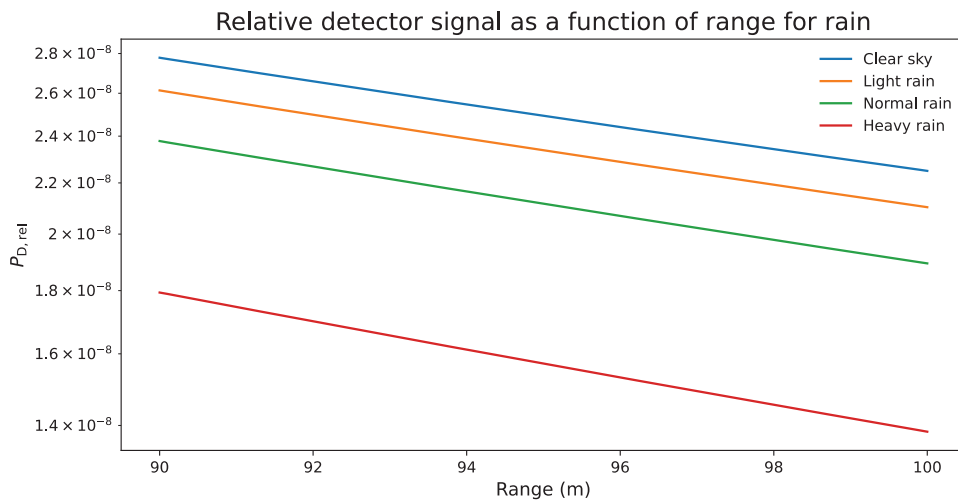


Figure 43 Plot of the relative lidar signal as a function of range for rain. For heavy rain the lidar signal loss is approximately 50%.

In addition to the general lidar equation above we have to consider the fact that the atmosphere contains small scattering particles the lidar signal will be affected. Small

particles are effective scatterers of the lidar beam which will be scattered into all directions. The back-scattering contribution to the lidar signal is,

$$P_D^{bs} = P_L \Omega_{p \rightarrow D} \frac{c\tau}{2} \beta e^{-2\gamma_{ext}r},$$

where c is the speed of light, τ is the pulse duration and the factor $1/2$ comes from the fact that, at a given time the thickness of the volume element contributing to scattering is that of a folded pulse [14]. For short ranges and long pulses, the back-scattering coefficient β can be very large.

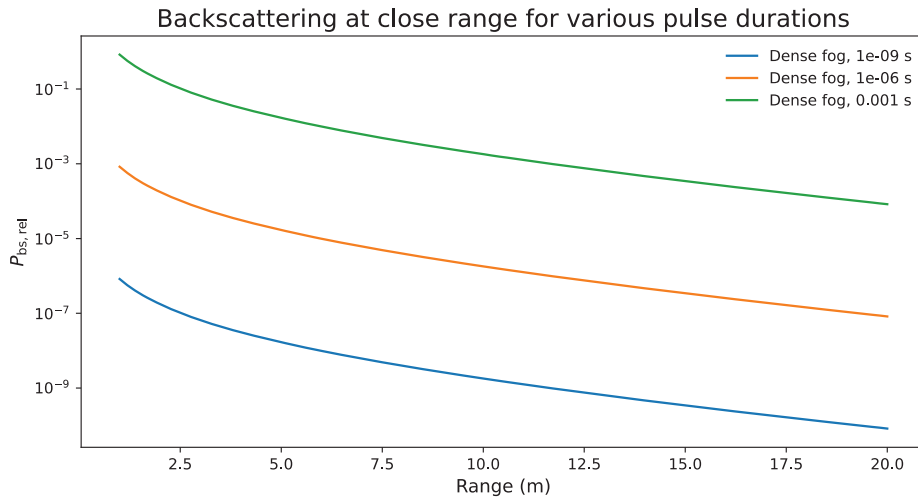


Figure 44 Back-scattering. The curves are orders of magnitude apart due to the pulse duration.

In summary, the lidar equation for adverse weather conditions is given by,

$$P_D = P_D^{wT} + P_D^{bs} + P_D^{noise},$$

where we also added noise for the sake of completeness. The useful lidar signal is

$$P_{SNR} = \frac{P_D^{wT}}{P_D^{bs} + P_D^{noise}},$$

where the backscattering is effectively considered as noise. Assessment of the P_{SNR} is specific to noise properties of the lidar system and the pulse dynamics of the laser and outside the scope of this project.

6.3.11 Extinction and back-scattering

To implement the lidar equation in adverse weather conditions it is necessary to calculate the extinction and back-scattering coefficients,

$$\begin{aligned}\gamma_{ext} &= N\sigma_{ext} = N(\sigma_{abs} + \sigma_{sc}), \\ \beta &= \frac{N\sigma_{bs}}{4\pi}.\end{aligned}$$

N is the particle density in m^{-3} , σ_{ext} , σ_{abs} , σ_{sc} and σ_{bs} are the extinction, absorption, scattering and back-scattering cross-sections, respectively. The extinction and back-scattering coefficients have unit m^{-1} and the cross sections m^2 . In general, it is an elaborate task to calculate the cross sections and in many cases, it is not possible to formulate an analytical solution. But for plane waves and perfect spheres Gustaf Mie derived analytic solutions. The physical cross-sections are often expressed in terms of capitalized dimensionless cross-sections,

$$\begin{aligned}\sigma_{sc} &= 2\pi a^2 Q_{sc}(x), \\ \sigma_{ext} &= 2\pi a^2 Q_{ext}(x),\end{aligned}$$

where a is the particle radius and $x = 2\pi a/\lambda$ the size parameter where $\lambda = n/\lambda_0$ and n the complex refractive index of water, see Figure 45. Data for water comes from [15].

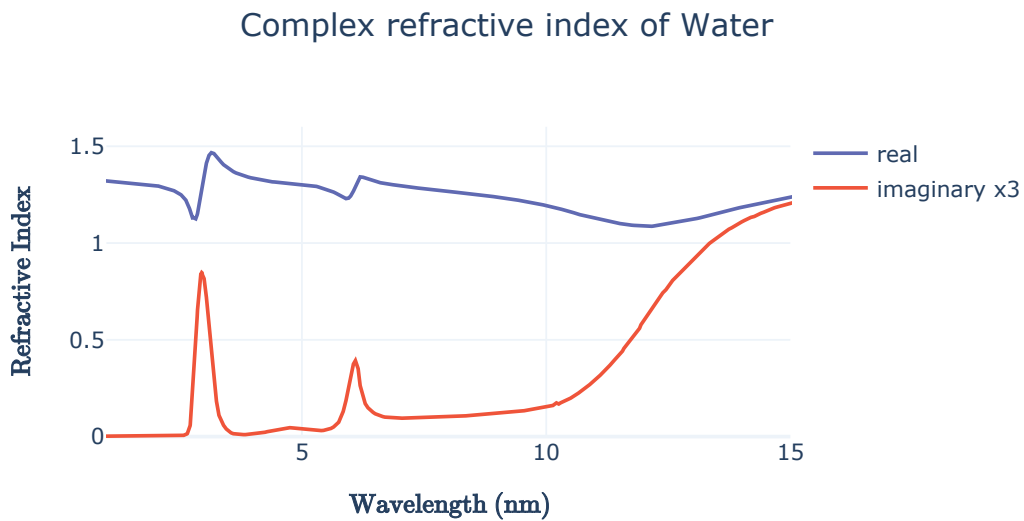


Figure 45 Refractive index used in the calculation of the Mie scattering coefficients.

It should be emphasized that the Mie solution is exact and that there are no constraints on the size of the particles. This means that the solution describes small particle scattering as well as large particles scattering. The intermediate realm where $a \sim \lambda$ is often referred to as Mie scattering. The analytic solutions involve infinite sums and have to be truncated. For example, if only the first component is retained the exact solution of Rayleigh scattering is recovered. Rayleigh scattering is valid for small particles. The extinction and back-scattering coefficients are,

$$\begin{aligned}\gamma_{ext} &= \frac{\pi}{4} \int_0^{\infty} N(\mathcal{D}) \mathcal{D}^2 Q_{ext}(\mathcal{D}) d\mathcal{D}, \\ 4\pi\beta &= \frac{\pi}{4} \int_0^{\infty} N(\mathcal{D}) \mathcal{D}^2 Q_{bs}(\mathcal{D}) d\mathcal{D},\end{aligned}$$

where \mathcal{D} is the diameter of the particle. To perform the integration it is necessary to use a particle size distribution function. Several distributions are proposed in the literature. Examples are the single parameter exponential distribution and the modified gamma distribution. However, drawbacks with those distributions are that they are not physical in the small size limit, and it is difficult to relate the parameters to physical quantities and one loses insight into the physics behind the phenomena. In this study we use the lognormal distribution,

$$N(\mathcal{D}) = \frac{N_{tot}}{\mathcal{D}\sqrt{2\pi}\ln(\sigma_g)} \exp\left[-\frac{1}{2}\left(\frac{\ln(\mathcal{D}/D_m)}{\ln(\sigma_g)}\right)^2\right],$$

since it is straightforward to relate the parameters to physical quantities. N_{tot} is the total particle density, D_m is the average particle diameter in terms of the geometric mean and σ_g the geometric standard deviation of the particle diameter. The lognormal distribution gives a better fit to rain data [16] compared to the modified gamma and the exponential distribution. Furthermore, the lognormal distribution is also used to describe haze and fog [17]. We infer that it is preferred, on physical grounds, to use the lognormal distribution to represent particle distribution.

6.3.12 Rain

In practice weather is measured and quantified in terms of macroscopic parameters. Visibility is used to characterize fog and rainfall rate is used for rain and snow [10]. However, to calculate the signal attenuation we only need to know the size distributions and the refractive index of the particles of different kind of weather. Here we relate macroscopic weather parameters to the lognormal distribution. Feingold and Levin [16] showed that the rainfall rate can be related to the parameters of the lognormal distributions through the following empirical relations. The dimensionless geometric standard deviation is given by

$$\sigma_g = 1.43 - 3 \cdot 10^{-3}R,$$

where R is the rainfall rate in mm/h. The number density of particles in m^{-3} is given by,

$$N_{tot} = 172R^{0.22},$$

and the geometric mean diameter,

$$D_g = 0.72R^{0.23},$$

in mm. For the calculations we use $R = 2.5, 10, 50, 100$ mm/h as standard rain rates. See table for values of the resulting extinction coefficients.

Table 4 Calculated extinction coefficients for the various atmospheres. γ_{1k} is the power-loss after 1 km in dB.

Type	rate (mm/h)	visibility (m)	γ (m^{-1})	γ_{1k} (dB)
Clear sky	0.0	-	0.0000	0.0
Light rain	2.5	-	0.0003	1.5
Normal rain	10.0	-	0.0009	3.7
Heavy rain	50.0	-	0.0024	10.6
Extreme rain	100.0	-	0.0036	15.7
Thin fog	-	500	0.0339	147.3
Normal fog	-	300	0.0565	245.5
Dense fog	-	100	0.1696	736.6

6.3.13 Fog

Fog is a meteorological term describing low visibility condition (less than 1 km) and a relative humidity close to 100% caused by small water droplets in the atmosphere. Fog is closely related to mist (1–5 km visibility, 95%–100% relative humidity) and haze (≥ 5 km visibility, $\leq 80\%$ relative humidity) which typically also include dust, smoke, pollutants and other micro-particles. However, it should be noted that there many ongoing debates on how to differentiate fog from haze and the definitions from the World Meteorological Organization is criticized [17].

The formation of fog can be vastly different from one case to another, and it is common to classify fog in accordance with this process. Examples of the normal fog classes are; radiation fog, advection fog, steam fog, stratus-lowering fog, precipitation fog, upslope fog, see [10] for more details. In some situations, it is more convenient to characterize fog in terms of its geographic location. For example, 'Monte di Procida' fog which we in this report consider to be 'normal fog' [18]. The formation of fog is complicated and the state of a fog is dynamic, its characteristics may change during a few minutes. Together with the fact that the particles are small and evasive it is quite demanding to measure fog and to accurately estimate the microscopic parameters.

For calculation of the Mie-scattering coefficients the normal fog classification is useless since it does not uniquely connect a given type of fog to the microscopic parameters. Moreover, fog is commonly referenced to in terms of its visibility and different types of fog may have the same visibility. In this report we side-step the complications imposed by the taxonomy and visibility reference. We assume the validity of the log-normal distribution and use the estimates of the log-normal parameters reported in [18]. Hence, for a given particle density N_{tot} the visibility is then the result of the calculation.

In the calculations we use the log-normal coefficients of 'Monte di Procida' which we consider to be 'normal fog'. The particle density is then changed to yield visibilities 500, 300 and 100 m which we classify as normal, thick and dense fog in accordance with what

is typically used in [10]. Values the calculated extinction coefficients are presented in the table.

6.3.14 Simulation model: water on objects

Figure 46 shows the setup of a laser beam directed towards the target along the z-axis and being scattered off the target at a specific tilt angle. There are altogether four different detectors capturing the reflected and scattered rays. The first two small detectors are one placed in a direction collinearly with the incoming beam and one placed in a direction of the specularly reflected beam. The collinear detector corresponds to the true lidar detector, seeing the exact backreflected light from the laser hitting the target. These detectors are named LIDAR DETECTOR COLLINEAR and LIDAR DETECTOR SPECULAR. The third detector is a slightly larger detector to enclose more of the diffuse scattered light, named MEDIUM DETECTOR, and the fourth detector is large enough to capture more or less all light diffusely scattered off the target, named LARGE DETECTOR. Both are centered collinearly with the incoming beam. The target is tilted with respect to the incoming beam (z-axis). The detector aperture has the same size as the laser beam. The larger detector is the last detector that absorbs all backwards propagating rays.

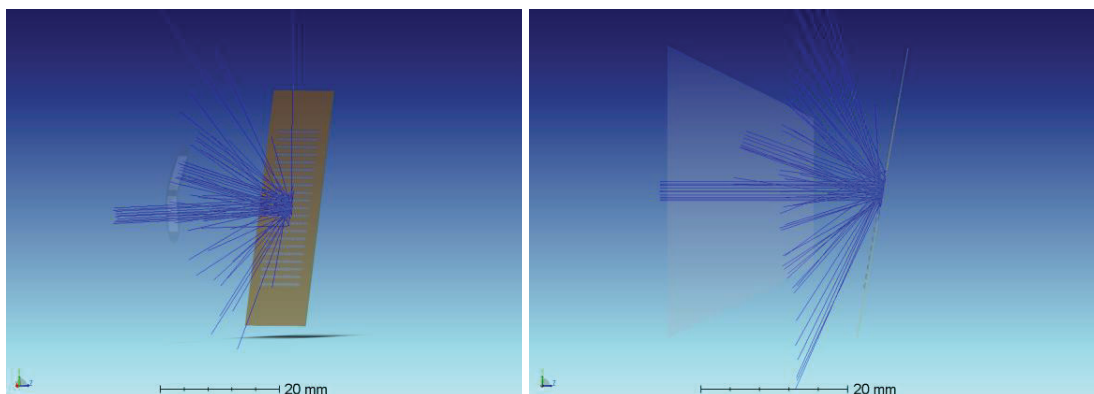


Figure 46 Physical simulation model for water on object

The normally large distance between target and detector together with the small detector aperture will create a narrow detection cone angle. A proper simulation would require setting up the model with true distances, hence leading to a great number of missing rays. One idea we tried was to move the detector close to the target (10 mm) to receive more ray hits, but virtually simulating placement at a far distance by filtering out rays of narrow angles to count as detected. However, this filtering also limits the number of rays to a corresponding degree and thus does not help. Instead, with the detector still being placed somewhat close to the target (near-field) we determined that it was better to receive a sufficient number of rays to limit simulation time by accepting rays with unrealistically large detection cone. We assume that the detected optical power will give us sufficiently accurate results on the behaviour of target reflections, while keeping the dimensions of the system smaller and simulation time shorter.

Each of the detectors are set to detect either coherent or incoherent light. Since the light source of a lidar system is normally a laser it will always provide some degree of spatial and temporal coherence in the system. Coherent light will show interference patterns and speckles due destructive and constructive interference between rays to a degree determined by the coherence length of the light. A coherent detector takes into account both the real and imaginary parts of the light field and presents the optical power as the square of the sum of the field amplitudes of each ray, whereas an incoherent detector sums all optical powers of each ray after taking the square of the field of each ray to get the power. We have seen clear differences in how the optical power adds up using these two cases between specular and diffuse components, depending strongly on the coherence length that is nominally set to 10 mm. In order not to lose any insight into what can be the true representation of the light, both the coherent and incoherent detectors are presented in the following plots. Both types of detector are normalized to represent the same total optical power.

Figure 47 shows a closeup of the target model, including the model for the wet condition with water droplets in an array configuration.

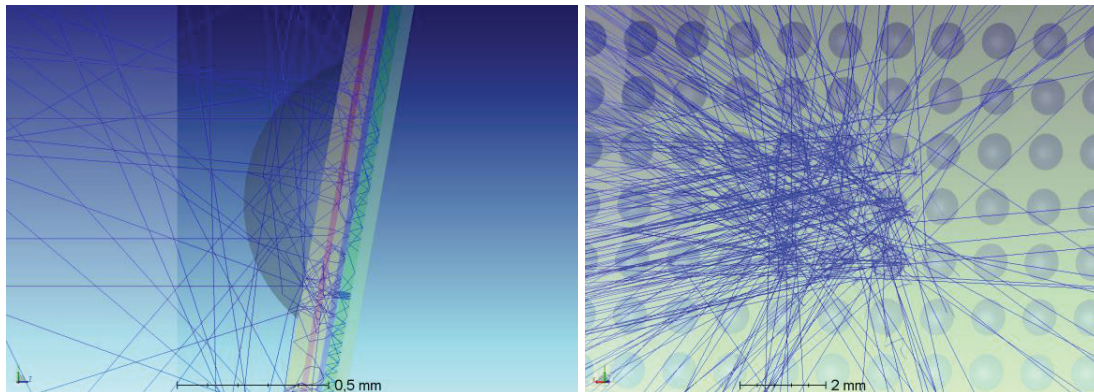


Figure 47 Close up of simulation model

6.3.15 Scenarios and materials

In the following simulations we consider a number of scenarios where the material is completely dry, completely wet or has a number of water droplets on the surface as determined by a wetting ratio χ and droplet radius r . The wetting ratio is defined as the area of water droplets to the total area, per unit area. Three different materials are investigated. The first material is a car lacquer made from PMMA (plastic acrylate), where the first surface layer is modelled as being plain reflective and transmissive. The second material is cloth made from PMMA (similar refractive index as many textiles) and modelled as a 100 % lambertian scatter. The third material, made of soft plastic PMMA is modelled as an 80 % lambertian scatter with 20 % specular reflection. The target is tilted with respect to the z-axis.

The optical power of the laser is set to 1 Watt and the received optical power is in the order of tens of mW in the current near-field configuration. The electrical output of the lidar detector will be proportional to the total optical power received including any noise components. Hence, the useful lidar signal will in reality be determined by the SNR (signal-to-noise ratio). In the following we do not distinguish between the signal and noise components since all light existing in the system will contribute to the signal. In a realistic environment, optical noise will originate from other light sources than the lidar laser. Also, the real detector consists of a single pixel and will not capture any information of the irradiance, only its integral, the total optical power.

From a theoretical viewpoint at normal incidence angle, the reflection coefficient in the air-to-PMMA interface (with PMMA having refractive index $n_2 \approx 1.5$) become $R = (n_2 - n)/(n_2 + n) = 4\%$ where $n = 1$ for air. In air-to-water (with $n_1 = 1.3$ for water) it becomes $R = (n_1 - n)/(n_1 + n) = 1.7\%$. Water-to-lacquer becomes $R = (n_2 - n_1)/(n_2 + n_1) = 0.5\%$. Thus, with water film on top of lacquer the reflection coefficient is approximately $R = 0.017 + (1-0.017)^2 \times 0.005 = 2.2\%$. Wet lacquer thus has about 55% of the reflection of dry lacquer.

Figure 48 presents the result of a simulation with nominal parameter values. The irradiance plots show clearly the effect of water droplets reflecting off rays in all directions, manifesting as dark spots in the specular lidar detector. For tilt angles larger than zero, the collinear lidar detector will only show the diffusely scattered light off the water droplets and the material behind. The coherent detectors clearly show speckle patterns with varying irradiance, whereas the incoherent detector is significantly more uniform. The medium and large detectors capture much more of the diffuse light and the angle of the specular reflection can also be seen as twice the tilt angle.

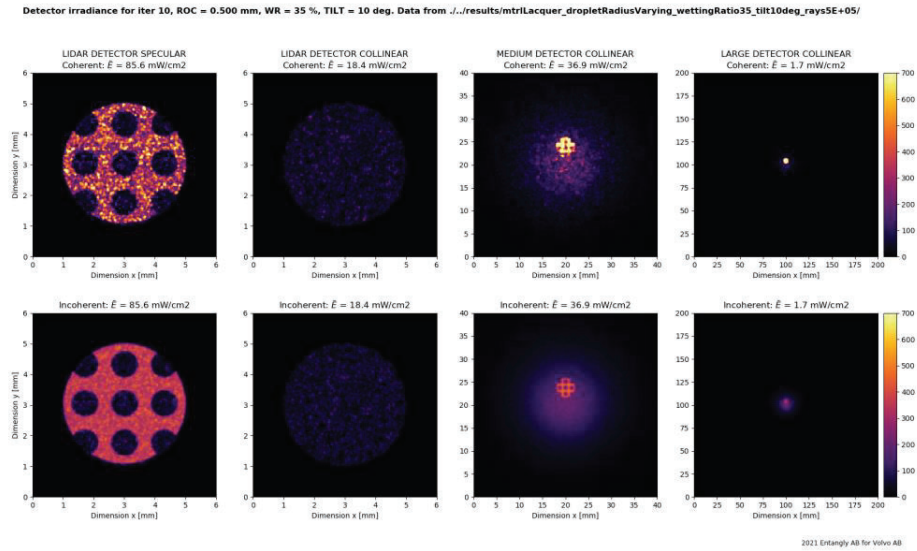


Figure 48 Irradiance plots for all four detectors with nominal parameter values. Radius of curvature 0.5 mm, wetting ratio 35 % and tilt angle 10. \bar{E} denotes the average irradiance level in the image. All images have the same scale in the colored dimension (irradiance).

6.3.16 Varying wetting ratio

Figure 49 to Figure 51 show the simulation results after varying the wetting ratio of the material surface. It is clear that lacquer and soft target material provide much stronger signal in the specular detector than cloth in dry conditions (lower wetting ratio). In wet condition (larger wetting ratio) all three materials give similar levels in the specular detector and diffuse light in the collinear detector. It is expected that there should be 4 % of the reflection from dry lacquer, which is confirmed by the detected 43 mW optical power out of 1000 mW. With water film on top of lacquer (right most end of plot) this value should be 55 % of 43 mW which is 24 mW. From the simulations we have only 10 mW, which is due to that we are not modelling a perfect water film at 100 % wetting ratio. Rather, each of the droplets sits adjacent to each other and still creates a scattering droplet surface similar to a rounded stone paved street.

The wetting ratio is varied between 0 – 100 % and has a nominal value of 35 % when kept constant. Figure 52 corresponds to data in Figure 49 and shows the result for lacquer material at 90-% wetting ratio. The specular detector has information of the specular reflection inbetween the water droplets. For cloth material, as in Figure 53 corresponding to data in Figure 50, there are no specular components and only diffuse scattered light is observed in all detectors for any wetting ratio.

Lidar detector power for ROC = 0.500 mm, TILT = 10 deg. Data from ./../results/mtrlLacquer_dropletRadius500µm_wettingRatioVarying_tilt10deg_rays5E+05/

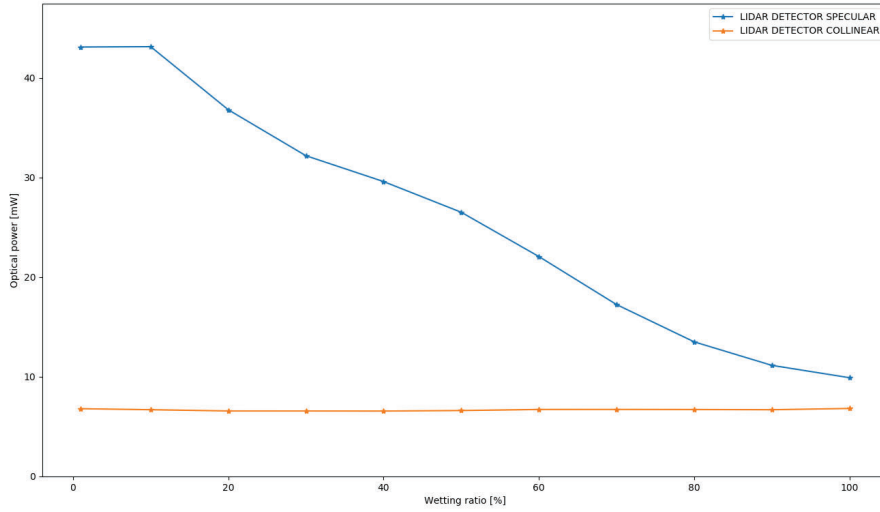


Figure 49 Data for lacquer material with pure reflective and transmissive properties. The specular detector (blue curve) gets a much stronger signal than the collinear detector (orange curve) in dry conditions. Nominal values for droplet radius of curvature 0.5 mm and tilt angle 10.

Lidar detector power for ROC = 0.500 mm, TILT = 10 deg. Data from ./../results/mtrlCloth_dropletRadius500µm_wettingRatioVarying_tilt10deg_rays5E+05/

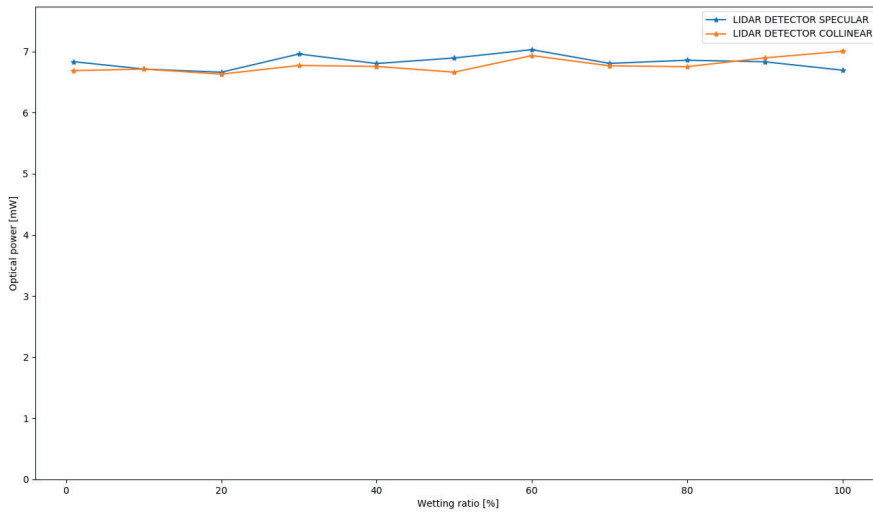


Figure 50 Data for cloth material with 100% lambertian scatter properties. As the cloth material has no specular component, the specular detector (blue curve) gets a similar signal as the collinear detector (orange curve) in both dry and wet conditions. Nominal values for droplet radius of curvature 0.5 mm and tilt angle 10.

Lidar detector power for ROC = 0.500 mm, TILT = 10 deg. Data from ./../results/mtrlSoft_dropletRadius500µm_wettingRatioVarying_tilt10deg_rays5E+05/

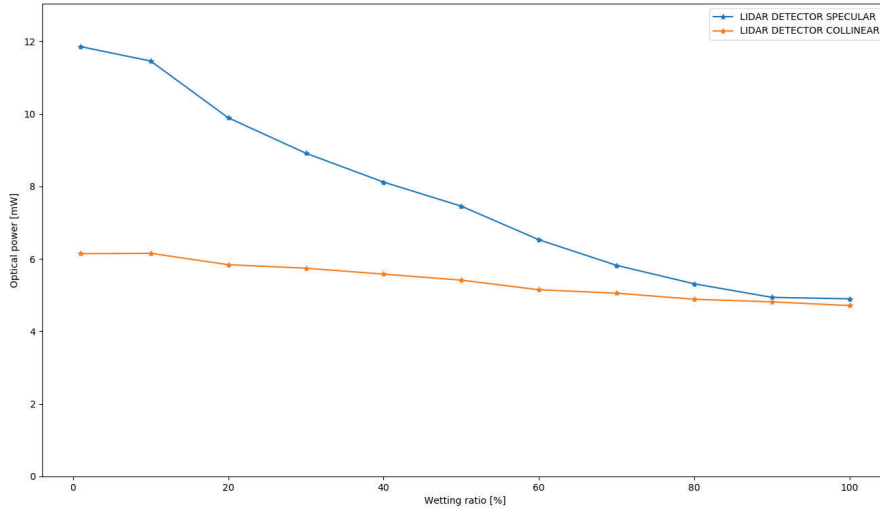


Figure 51 Data for soft plastic material with 80% lambertian scatter properties and 20% specular reflection. The specular detector (blue curve) gets as much signal than the collinear detector (orange curve) in dry conditions. Nominal values for droplet radius of curvature 0.5 mm and tilt angle 10.

Detector irradiance for iter 9, ROC = 0.500 mm, WR = 90 %, TILT = 10 deg. Data from ./../results/mtrlLacquer_dropletRadius500µm_wettingRatioVarying_tilt10deg_rays5E+05/

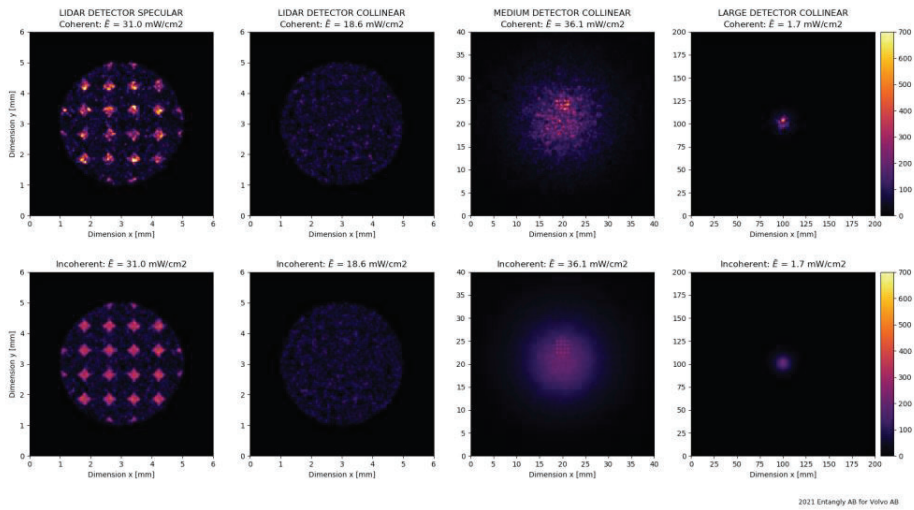


Figure 52 Irradiance plots for all four detectors with wetting ratio 90 % and lacquer material, showing the artistic effect of light being specularly reflected inbetween droplets. Radius of curvature 0.5 mm and tilt angle 10. \bar{E} denotes the average irradiance level in the image. All images have the same scale in the colored dimension (irradiance).

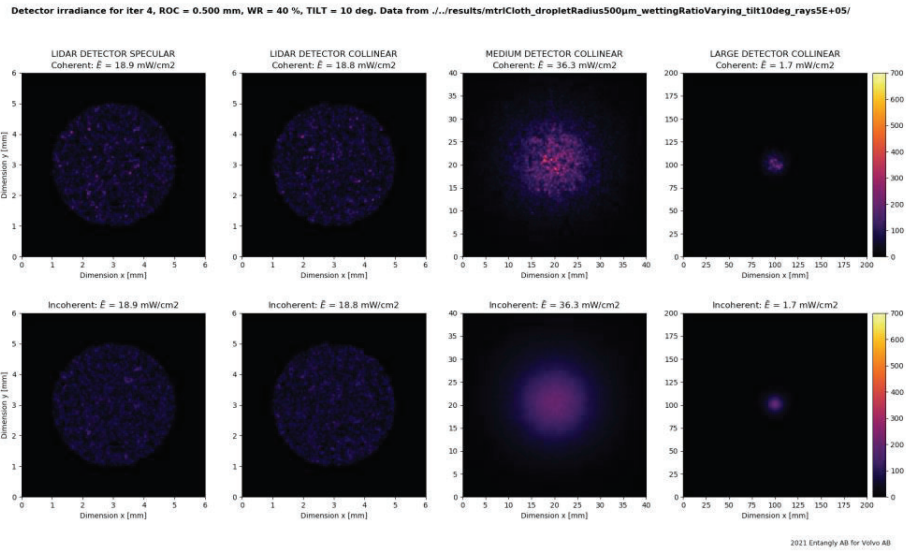


Figure 53 Irradiance plots for all four detectors with wetting ratio 40 % and cloth material, without only diffuse scattered light seen in all detectors since there the material is a completely lambertian scatterer without any specular reflection property. Radius of curvature 0.5 mm and tilt angle 10. \bar{E} denotes the average irradiance level in the image. All images have the same scale in the colored dimension (irradiance).

6.4 Calibration for field measurement

In this section aspects of data logging, calibration, alignment, post processing connected to the field measurements are explained.

6.4.1 Calibration of radars used

To be able to separate the target from the background noise and measurement site and attempt to achieve more detailed target characteristics, circular measurements of the site, without any target present, was performed.

The radars were calibrated against a trihedral corner reflector with well-known RCS to make it possible to relate the recorded signal to an independent physical value. Calibration was performed for range and azimuth separately and it is assumed that they are independent variables. For the calibration measurements the radar under calibration and corner reflector were placed at the same height and adjusted using a simple spirit level. To avoid large influence of multipath via ground they were placed at a height which ensured the signal path via ground would end up in a separate range bin, thus possible to isolate from the desired signal.

The range calibration used a setup, similar to that used for the linear measurement, letting the radar on a sensor carrier slowly close in on the corner reflector.

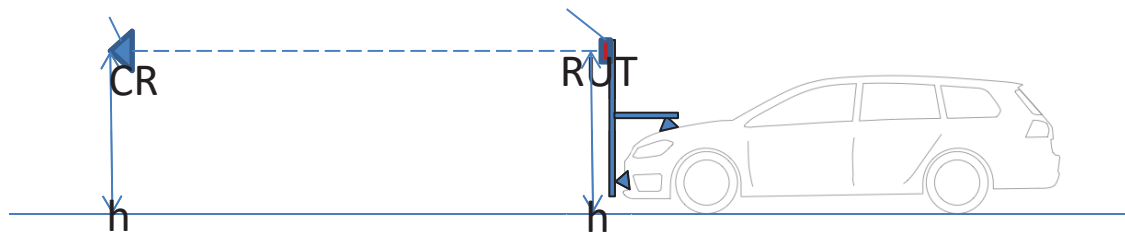


Figure 54 Radar calibration using the motion rig

For the azimuth calibration the radar was instead placed on a turntable rotating it along its antenna plane, thus placing the corner reflector at different known angles relative to the radar. The turntable was rotated stepwise, and the data collected for each measurement point with the radar/turntable at stand still.

All signal processing done on the radar data is based on the assumption that the system noise is due to thermal effects and has a white Gaussian noise (WGN) distribution. To verify this assumption and also check the radar amplifier noise figure, data from a drive with a known target size RCS have been evaluated.

Test with and without radome indicates a loss of 4 to 6 dB over the target azimuth angle because of the radome.

In summary, the noise levels and figures, system gain, and processing gains are in accordance with the theoretical values.

6.4.2 Adjustment of radar and lidar

6.4.2.1 Alignment of radar sensors

For analysis intended at locating radar scattering centers it is likely important that the sensors are properly aligned. We here present one way to assess the mounting error for the circular measurements so that they may be compensated for in the post processing. This method assumes the recorded frames are (fairly) evenly distributed over an entire circulation around the target. These steps are performed for each radar separately.

1. Generate the range-angle fourier transform for the recorded frames of one complete circulation
2. Average the amplitude of all frames into one compound 2D-matrix
3. If the sensor is properly aligned, the resulting image should show a symmetry centered around 0° (at the range of the target).

4. The offset from 0° corresponds to the mounting error of the sensor in the azimuth plane

6.4.2.2 Adjustment of radars

Measurements of the calculated signal strength from a known reference object (trihedral corner reflector with both radar and target at a large height) was taken with the reference object located at a well-known azimuth angle relative to the radar boresight. The signal recorded at boresight was taken as a relative reference. A calibration curve to compensate for the divergence from that reference value at different azimuth angles was deduced from this. An example of such normalized data can be seen in Figure 55. There only the data in the azimuth range $\pm 30^\circ$ is shown. Beyond this the gain of the antennas fall rapidly and thus the compensation factor increases correspondingly. It appears the radome used within the project generates some unforeseen effects which limits our trust in the data from far outside the vicinity of the boresight. Luckily, the methods used in this project generally places the target close to boresight and we can thus safely, mostly ignore data and signals appearing to originate outside a field of view as narrow as approximately $\pm 10^\circ$.

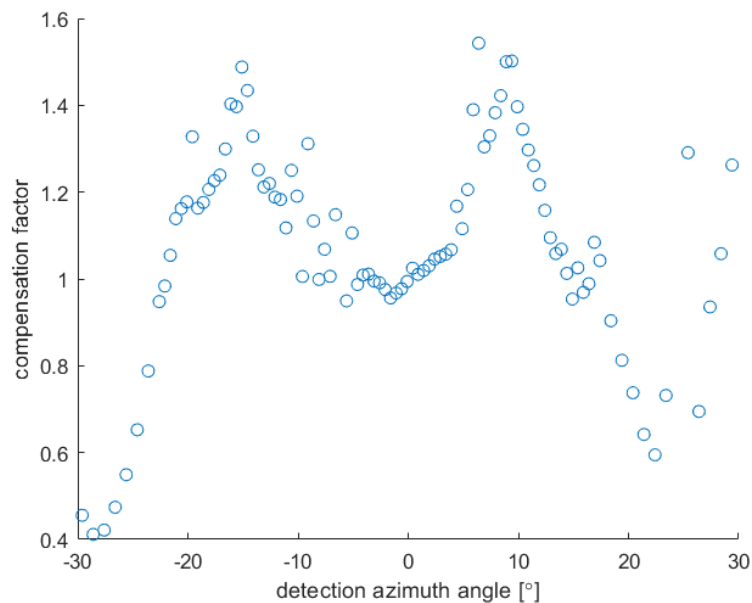


Figure 55 Example of data/compensation factor used to generate calibration curve over azimuth. Y-axis is the compensation factor and x-axis is the detection azimuth angle.

For the range calibration the radar and reference object (trihedral corner reflector) were both placed at a large height, with the reference object in boresight of the radar, and the signal at the radar was recorded at several points during a slow approach towards the reference object. The resulting calculated signal amplitude was compared to the known

RCS of the object and a curve for the amplitude compensation factor could thus be calculated from this data. Each channel was treated separately as they showed slight differences in amplitude. Possible phase errors have not been compensated for as the calculated azimuth angles have proven to very consistent with ground truth for the reference measurements.

6.4.2.3 Alignment of lidars

To be able to properly filter and use the collected lidar from the test vehicle, an extrinsic calibration must be performed to align the reference coordinate systems of each lidar to the vehicle reference frame. This calibration is purely geometrical to account for tolerances in the mounting brackets. Since the lidars occasionally need to be dismounted between measurement campaigns, the exact mounting pose can change between campaigns and impact the filtering required to backproject the detections from the target into a bounding box. This ensures that the point cloud data can be used to compare features of the targets in the closest way possible by keeping the target aligned to the bounding box.

6.5 Results from field experiments

In this section results from the sessions of logging data at AstaZero will be presented. The section starts with a guide how to read the plots. It is natural to present results as plots, due to the high dimensionality data from the sensors.

6.5.1 Interpretation of RCS and heatmaps

A simple way to assess the expected radar reflectivity of a target from a variety of view angles is to look at the maximum of the RCS as a function of view angle. As the targets most likely have multiple scattering centres that will interact there will be rapid variations in the recorded RCS over angle. The same effect is likely present also for the elevation angle, but our sample density in that direction is much lower (partly because we generally expected smaller variations in the aspect angle in the elevation direction as we are moving in one plane). As the ground essentially may act as a mirror there will very likely be a pronounced effect similar to that from multiple scattering centres. For this reason, we present data from three different radars located at different heights.

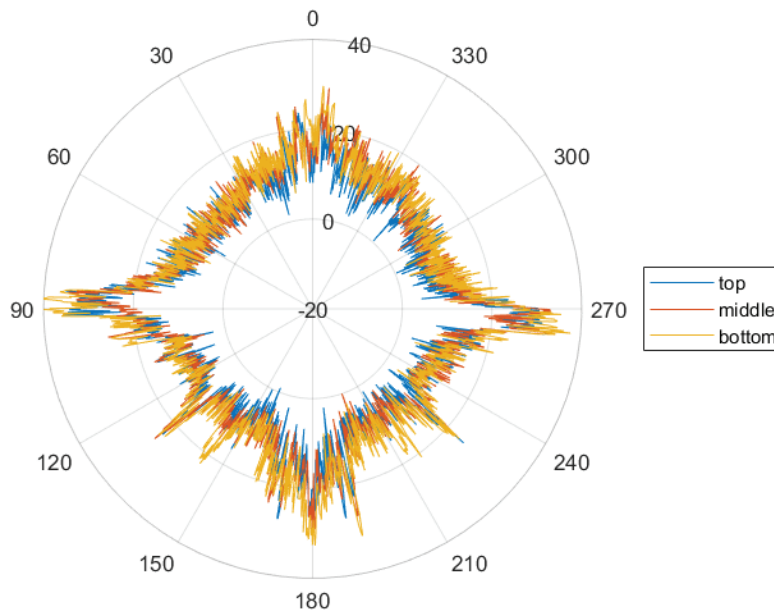


Figure 56. Target RCS [dBsm] over angle. The maximum at each measurement point is shown. Target is a Ford Fiesta and the range to center of rotation is 30 m.

Something alike to an estimate of the far field scattering diagram, where these rapid variations should be less visible, can be achieved through low pass filtering over angle, e.g. by applying a moving average.

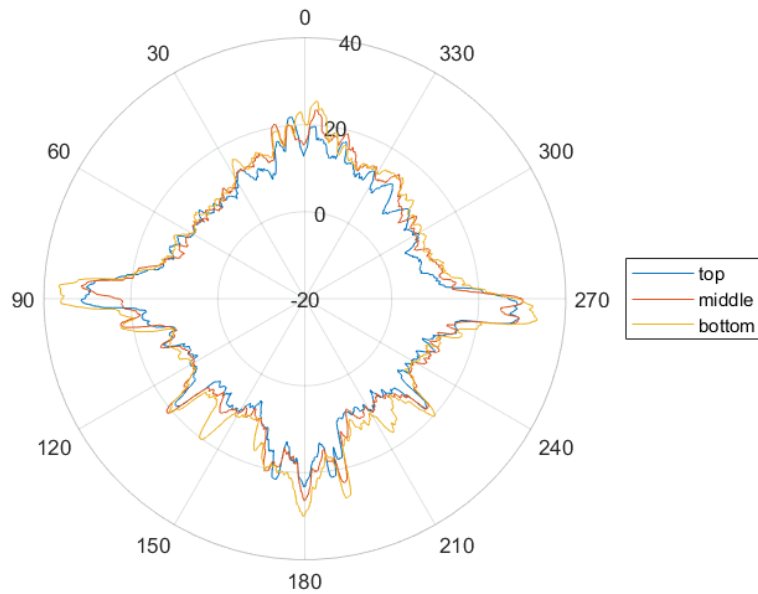


Figure 57. Target RCS [dBsm] over angle with a 5 degree wide moving average filter applied to the data shown in Figure 56.

For the measurements that generate the results seen in Figure 56-Figure 57 it appears the target was misplaced from the centre of rotation with about 1 m to the right. This may be one reason for the asymmetry seen between the left and the right side.

In Figure 58 and Figure 59 the orientation of the target is the same as in Figure 56, i.e. the front of the target is supposed to point straight up or towards 0° respectively. A small rotational error of the target can also be seen in both types of graphs.

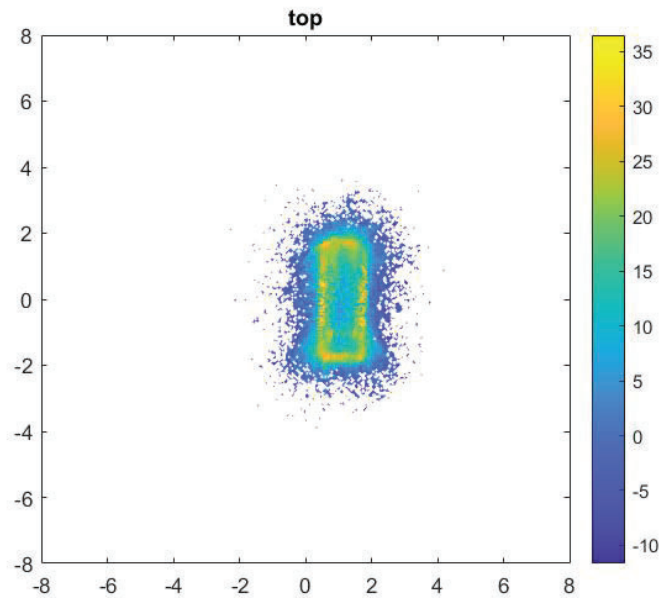


Figure 58. RCS weighted backprojection occupancy grid of measurements from all angles. Target is a Ford Fiesta and the range to center of rotation is set to 30 m. Axis is x-y grid [m]. Center of rotation of measurement rig is at (0,0). Color indicate accumulated RCS [dBsm]for each grid point. Grid resolution is 5 cm.

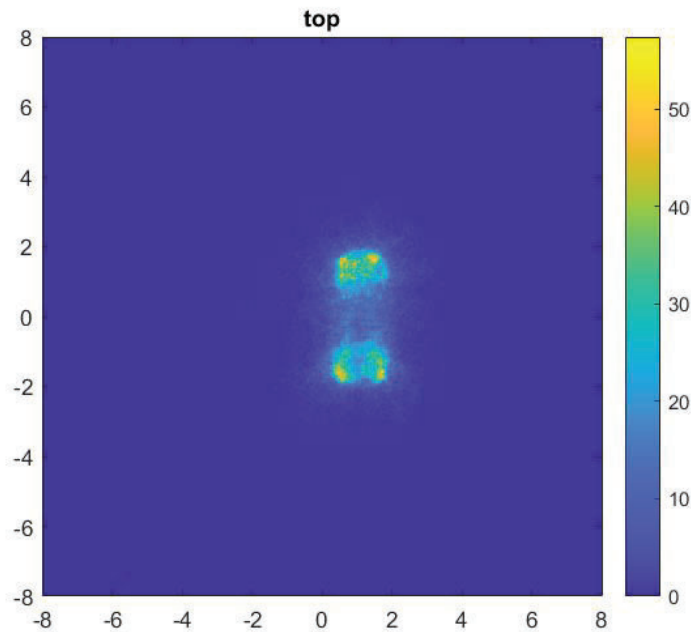


Figure 59. A non-weighted backprojection occupancy grid of measurements from all angles. Target is a Ford Fiesta and the range to center of rotation is set to 30 m. Axis is x-y grid [m].

Center of rotation of measurement rig is at (0,0). Color indicates accumulated detection count for each grid point. Grid resolution is 5 cm.

It is not only the magnitude of the reflected signal that may be of interest, but also the perceived origin. There may be several scattering points on a target that could simultaneously be detected and contribute to the perception of the target. The signal reflections from these could also interfere and interact with each other resulting in perceived fluctuations in resulting perceived signal strength as well as origin from frame to frame. For this reason, it can be of interest to try to locate major as well as minor scattering centers. We here do that by inspecting the signal for all range bins that show a signal strength above a threshold decided by inspecting recordings of the background (an empty measurement site). The resolution over angle is unfortunately quite poor, but by evaluating over a large number of angles/angle bins the maximum peak over angle can still be decided with high precision. For each range bin above the threshold, we then let the maximum over angle represent the angular location for the reflected energy of that specific range bin. By using the GNSS data, the resulting list of points with range, angle and RCS can then be backprojected onto an occupancy grid at the location of the target. Figure 58 shows the data, from all frames in one revolution around the target, backprojected and added on the grid weighted by their RCS.

While the additional method used to generate Figure 58 will likely emphasize the most prominent scattering centers, in the sense of signal strength, that may not necessarily reflect what points on the target most commonly appear above the threshold level, and/or minor scattering centers may be hidden behind the energy of the more dominant. As these other reflection points likely influence the overall behaviour of a target, they are still of interest. Figure 59 shows the same occupancy grid as in Figure 58, but is in contrast unweighted, and thus only count the number of points above the threshold without any other respect to their signal strength. It paints a slightly different picture which may also be important to take into consideration when constructing High fidelity surrogate target (soft or virtual). One way of explaining the difference between the two occupancy grids is that the RCS-weighted can be seen as an indicative reflectivity heat map, while the unweighted functions as a heat map for another detectability variable.

6.5.2 Voxel based point cloud comparison

The voxel-based comparison method (3D grid) was applied to the linear measurement scenarios. By applying the method to each frame of the approach at 10 kph, the gradual change in observed visible characteristics such as the highly reflective licence plate and taillights can be seen as a function of detection range.

After calibration and filtering has been applied the contents of the lidar frame are reduced to only the points inside the filtered bounding box. A voxelization algorithm is then applied to the contents of the bounding box and different KPIs are generated for each

voxel depending on the number of points per voxel, intensity statistics within the voxel. Future work would be to expand the list of KPIs and in the end generate parameters that describe the geometry and reflectivity contents of the voxel grid as a whole.

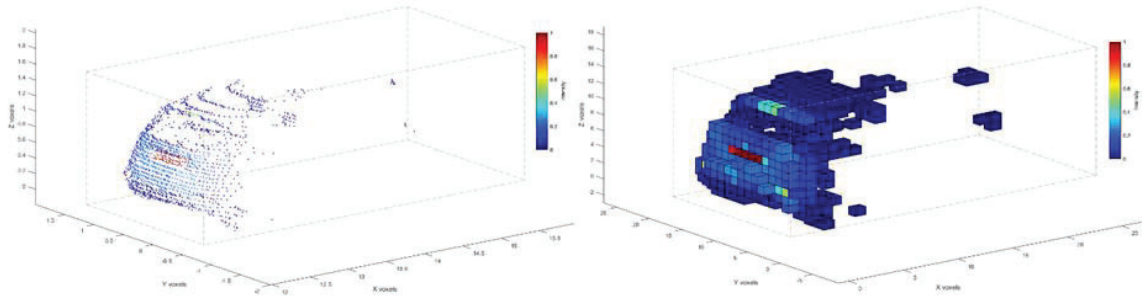


Figure 60 shows an example of a filtered point cloud of a target from a linear approach measurement before and after voxelization is applied to it.

Figure 60 shows an example of a filtered point cloud of a target from a linear approach measurement before and after voxelization is applied to it. The measured reflectivity, often referred to as intensity, differs between lidars due to the difference in reflectivity measurement resolution and dynamic range of the lidar receiver. Therefore, the intensity is normalized to a range between 0 and 1 for each lidar.

A Matlab tool was created to allow for higher visibility and ability to step through the measurement log during analysis while being able to look at different voxel KPIs as well as the original point cloud and at what range the target is in each frame. The tool allows the user to change the view of the filtered object, step through the point cloud as well as playing through it in forward and reverse at different speeds. Additionally, the tool allows the user to change between voxel view and the original point cloud view and even see the parts of the original point cloud that have been filtered out to better see where the object is in the original point cloud. Finally, the tool allows the user to choose whether to plot only one of the lidars at a time or both to allow comparisons.

Example results for application of the voxelization method on the linear approaches toward the rear of the real car target and the softcar can be seen in Figure 61 and Figure 62 for the Luminar Hydra and Figure 63 to Figure 64 for the Velodyne HDL-64, both with the target at 12m range. The examples shown here consider the mean reflectivity measured in each voxel as the distance to the target changes. Other metrics considered in the method are maximum reflectivity, minimum reflectivity and number of points in each voxel.

An important factor in this analysis method is to choose the size of the voxels that the target is split up into. If the voxels are too large, the attempt of the voxelization to extract defining features of the geometry of the filtered object will be reduced due to features like the sloping shape of the trunk and the high reflectivity of the licence plate will blend

together into a single voxel that contains information from too many features. If the voxels are too small, the voxel grid will start resembling the original point cloud and no new information is inferred in the voxel grid. After experimentation with voxel sizes of between 8 voxels per side to 64 voxels per side, the voxel size was decided by considering the difference in length, width and height of the vehicle target and defining the voxel grid as an array of 28x18x16, respectively.

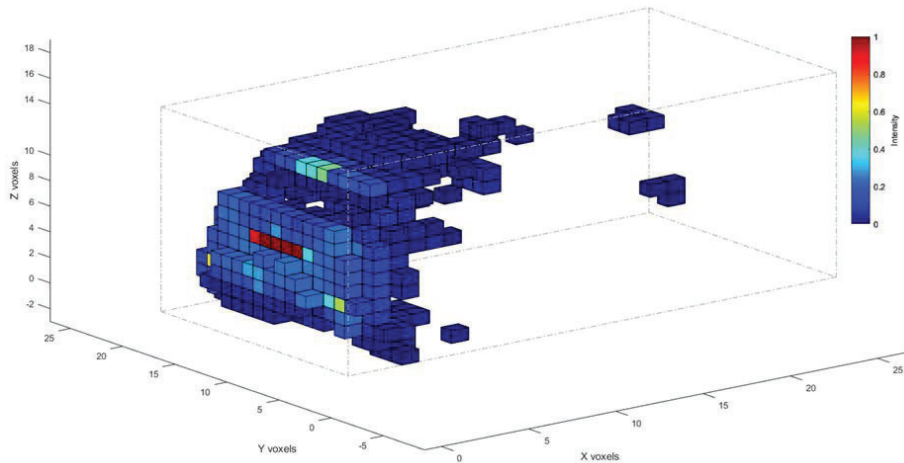


Figure 61 An example of the voxelization method applied to a point cloud from the Luminar Hydra of a Ford Fiesta.

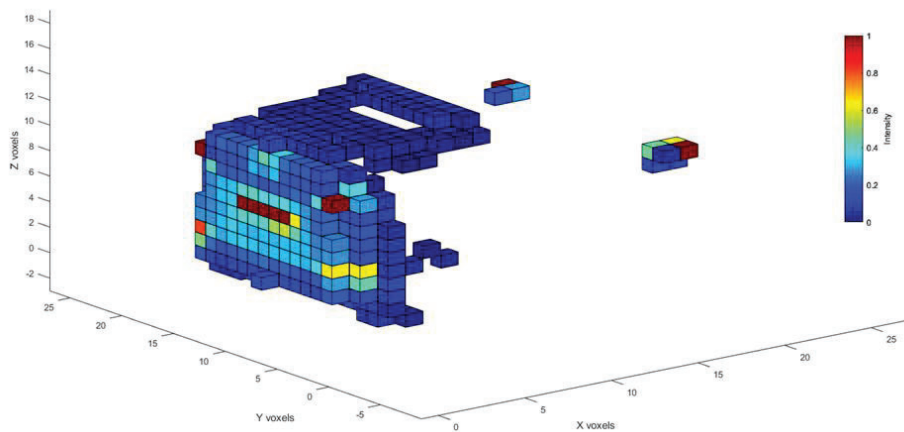


Figure 62 An example of the voxelization method applied to a point cloud from the Luminar Hydra of the soft car target.

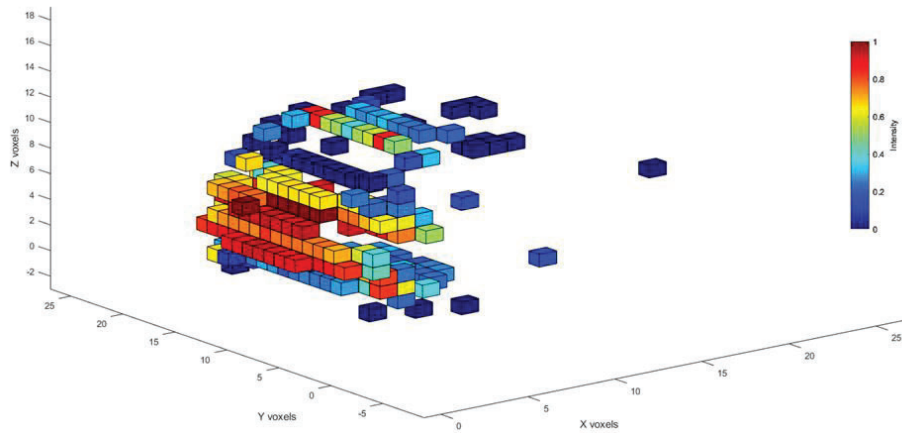


Figure 63 An example of the voxelization method applied to a point cloud from the Velodyne HDL-64 of a Ford Fiesta.

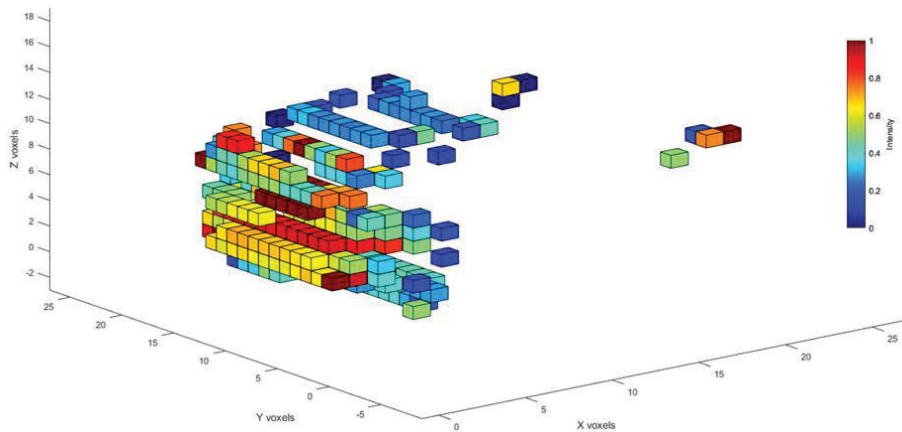
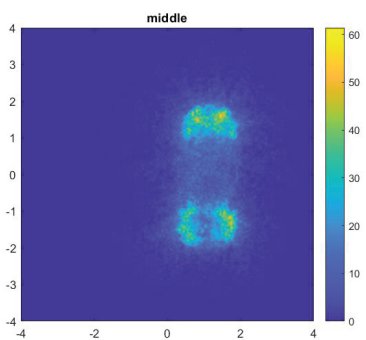
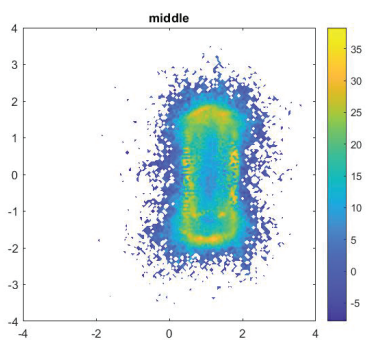
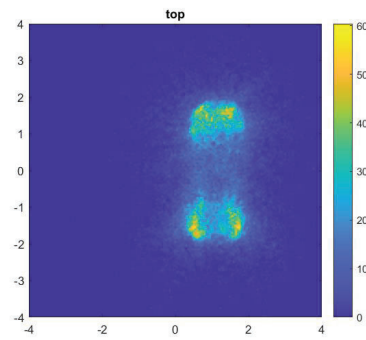
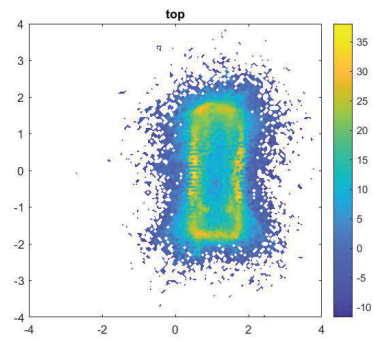
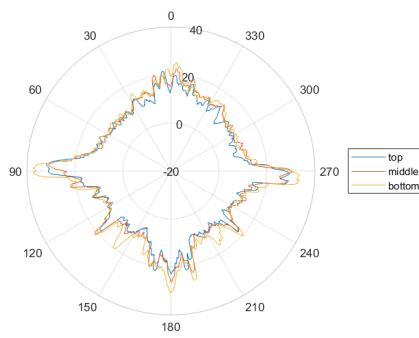
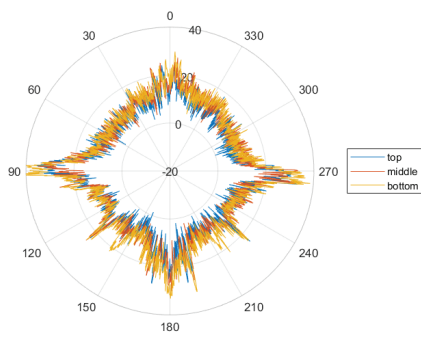


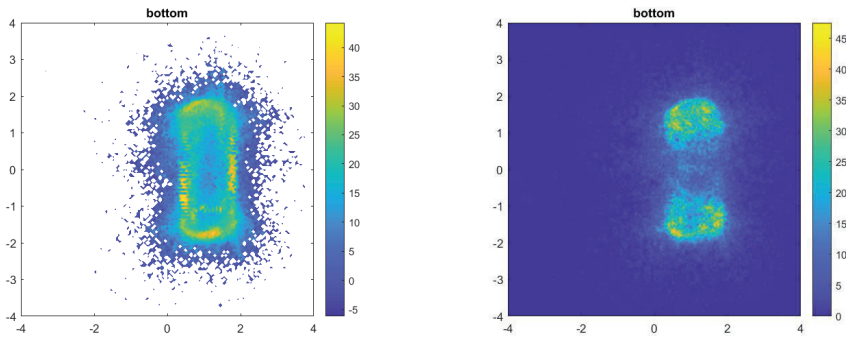
Figure 64 An example of the voxelization method applied to a point cloud from the Velodyne HDL-64 of the soft car target.

As can be seen in the examples in Figure 61 to Figure 64, the difference in dynamic range between the Luminar Hydra and the Velodyne HDL-64 means that there is a difference in how well features can be identified in the voxelization outputs. For the Luminar lidar, features such as the licence plate, taillights and rearview mirrors can be identified and compared between the real car and soft car targets but from the Velodyne lidar it is more difficult to distinguish certain features although the licence plate can be seen as a highly reflective group of voxels.

6.5.3 Ford Fiesta and surrogate

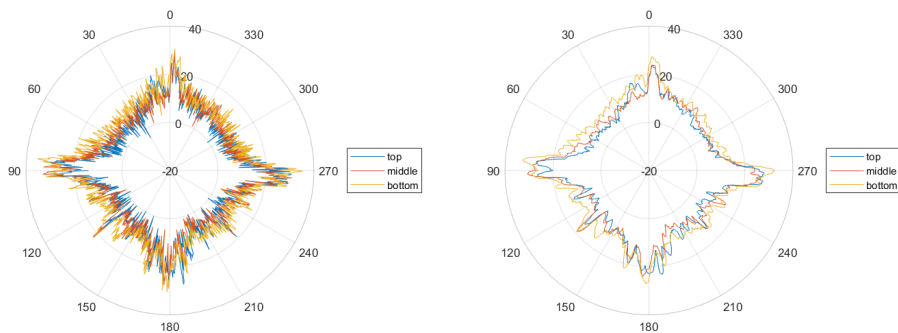
6.5.3.1 Ford Fiesta (30 m)

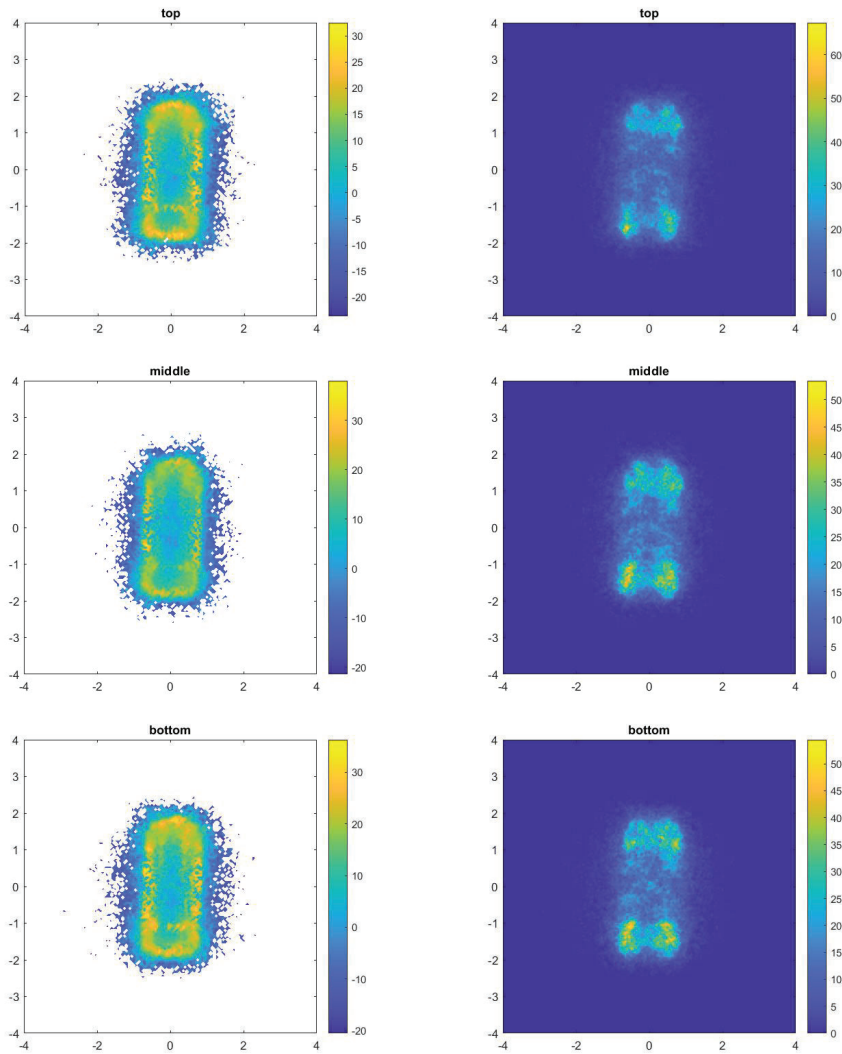




The weighted occupancy grid figures show that, in addition to the surface of the target, the rear axis should be viewed as a point of high reflectivity. The unweighted occupancy grid however appears to put emphasis on the corners of the target as points that can frequently be detected from many different view angles. The wheels and/or wheelhouses also appear to be visible from many different directions. Center regions of the sides can give very strong reflections but can only be seen from a limited number of angles.

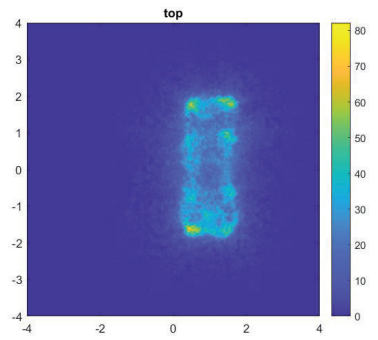
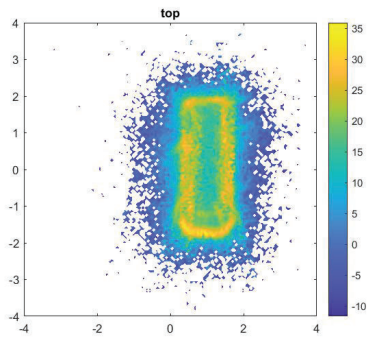
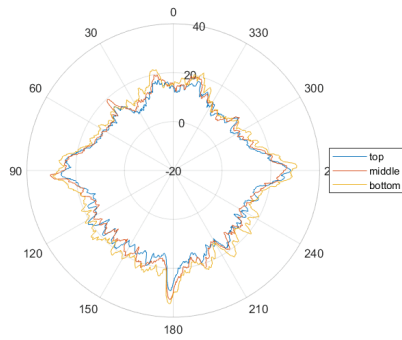
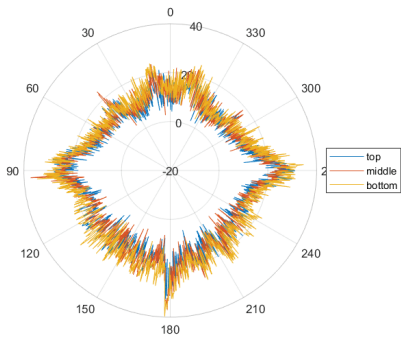
6.5.3.2 Ford Fiesta (15 m)

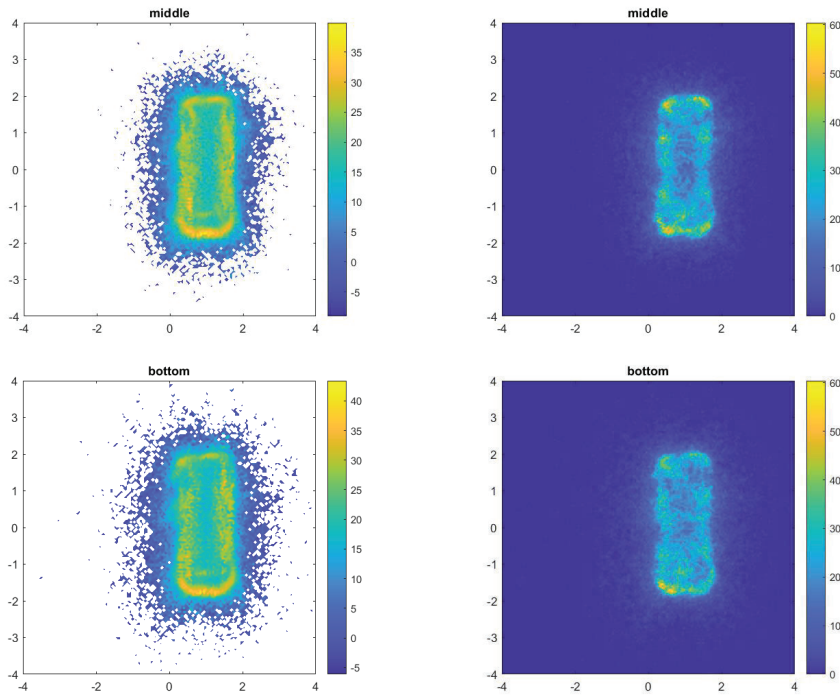




At the shorter distance, it appears the reflectivity peak of the target as seen from the front (0°) is sharper in contrast to the surrounding angles when comparing the RCS diagrams with the corresponding diagrams for the longer distance. The occupancy grids could perhaps be said to show a little bit more detail at the shorter distances, but the difference is not obvious.

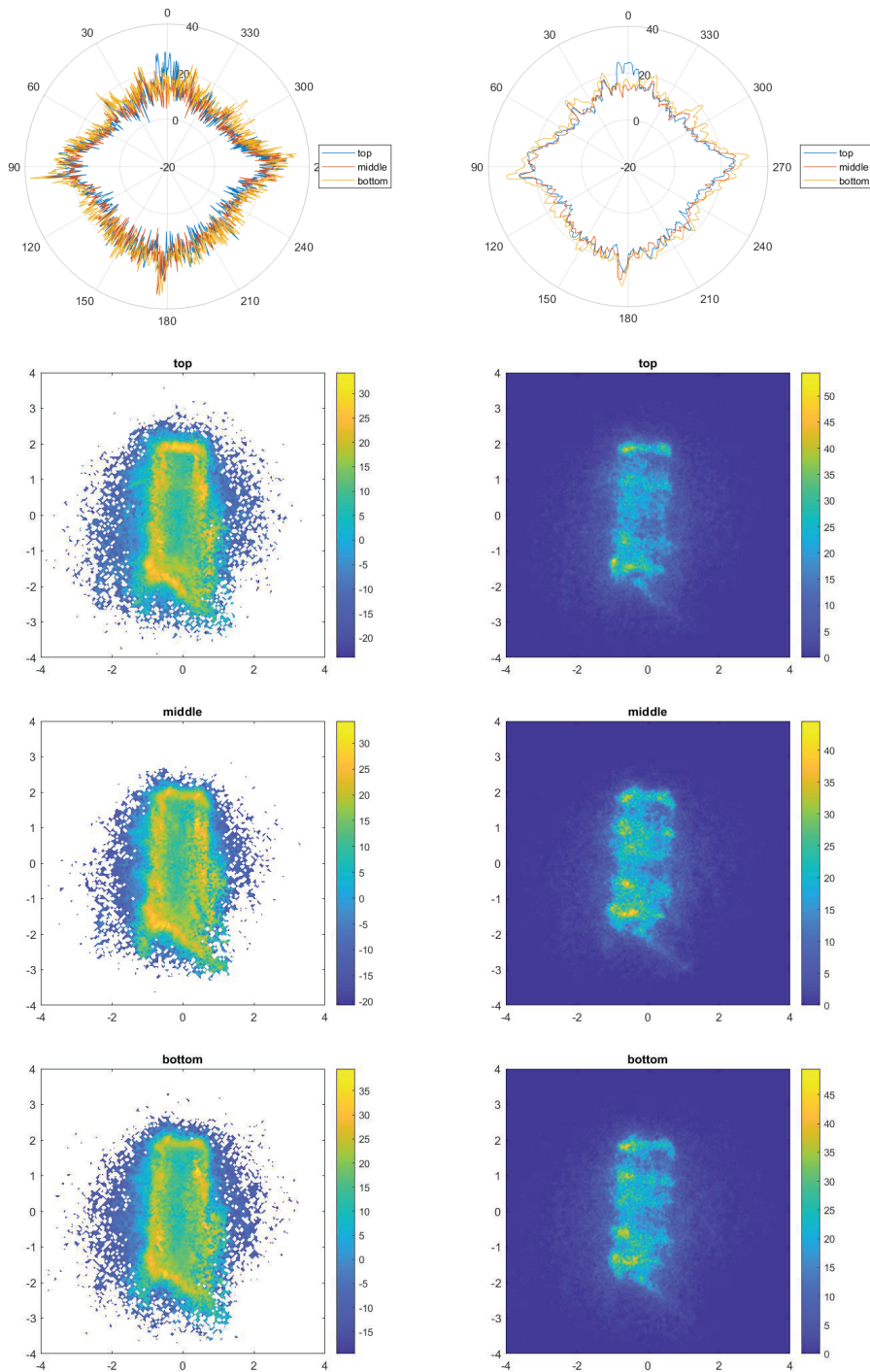
6.5.3.3 Soft Car 360 (30 m)





The figures generated for the soft surrogate target reveals some differences between it and the real counterpart. The RCS diagrams shows a similar shape and levels for the soft as for the real target. The soft target does show much less symmetry, but this would not necessarily pose a problem as a radar mounted on a vehicle would not be able to see both sides at the same time anyways. It is thus likely more important that the levels detected appear reasonable for the type of target the surrogate is to represent. As can be seen in the RCS-weighted occupancy grid figures the strongest detections are at the surface of the target also for the surrogate car target and there is even a strongly reflective feature going from side to side close to the rear of the target, similar to what was seen for the rear axis in the real car, but perhaps a little too far back. The more frequently detectable regions seen in the non-weighted occupancy grid figures are not as concentrated to the corner regions. It even appears possible to make out the skeleton of the target as lines going from side to side in the target. This is even more pronounced for the measurements at 15 m.

6.5.3.4 Soft Car 360 (15 m)



For the measurements at the closer range the inside structure of the soft surrogate car target becomes even more visible. The skeleton to hold up the visible canvas consists of a

dozen of plates threaded into each other perpendicularly. Some error also appears in the lower right corner of the occupancy grid figures (rear right side of the target) where the figures become less clear. It is proposed that this could be due to some error when mounting the target.

In the previous project, HiFi radar target, it was noted that the signal had a larger tendency to bounce around, inside the surrogate car targets than what could be seen in the real counterparts, resulting in a multitude of small detections reported behind the target measured. This effect has not been noted in the measurements results within the CONVICTION project. We are not able to judge if this is due to the efforts that has been made to improve the targets or if the new methods simply cannot provide us with the same information in their current state. One way to evaluate this could be to use the new measurement methods to evaluate the old target with the known issues.

6.5.4 Linear approach to real and soft car

Here a comparison of real and soft car at various distances with two lidar sensors will be shown.

Results of applying the voxelization comparison method with mean intensity per voxel on the **Ford Fiesta real target** from a linear approach with the Luminar Hydra at 10m, 30m, 50m and 100m can be seen in Figure 65 to Figure 68.

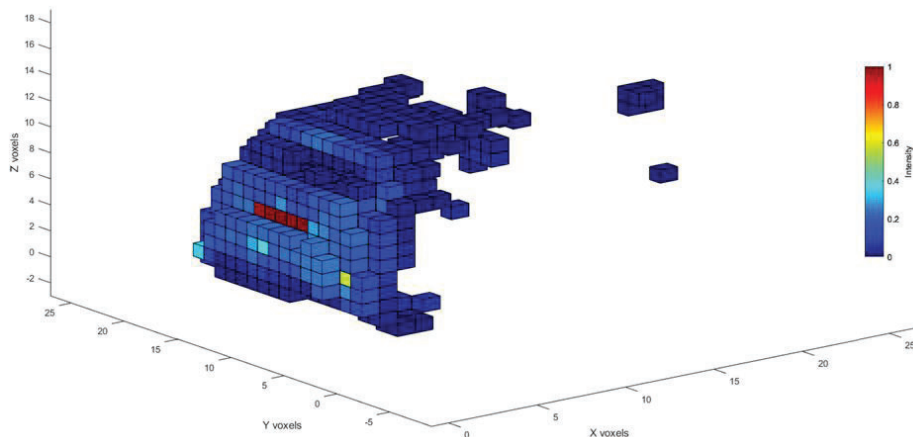


Figure 65 Real car voxelization results for Luminar Hydra point cloud at 10m range during a linear approach.

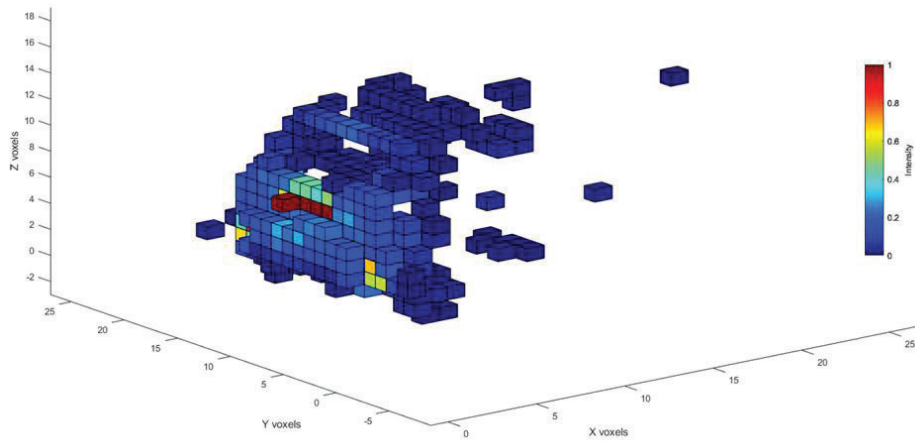


Figure 66 Real car voxelization results for Luminar Hydra point cloud at 30m range during a linear approach.

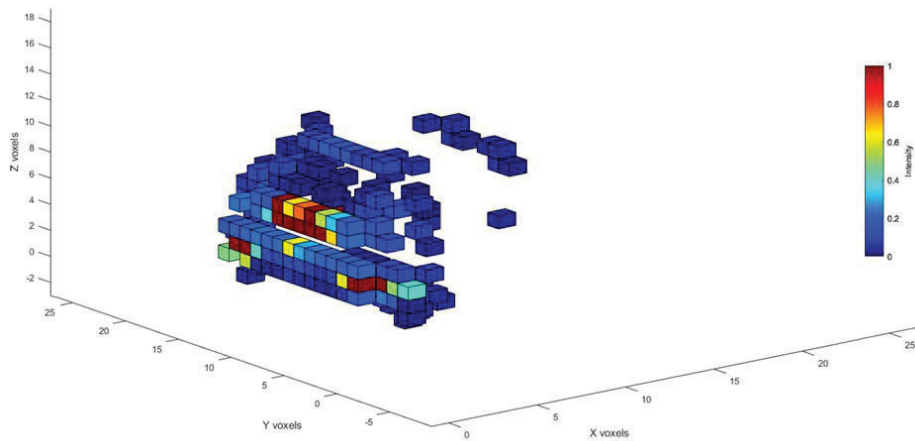


Figure 67 Real car voxelization results for Luminar Hydra point cloud at 50m range during a linear approach.

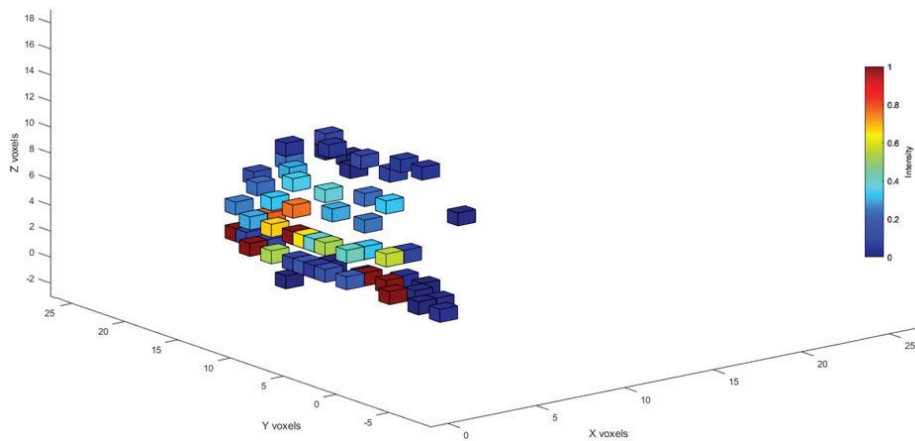


Figure 68 Real car voxelization results for Luminar Hydra point cloud at 100m range during a linear approach.

Results of applying the voxelization comparison method with mean intensity per voxel on the **soft car target** from a linear approach with the Luminar Hydra at 10m, 30m, 50m and 100m can be seen in Figure 69 to Figure 72.

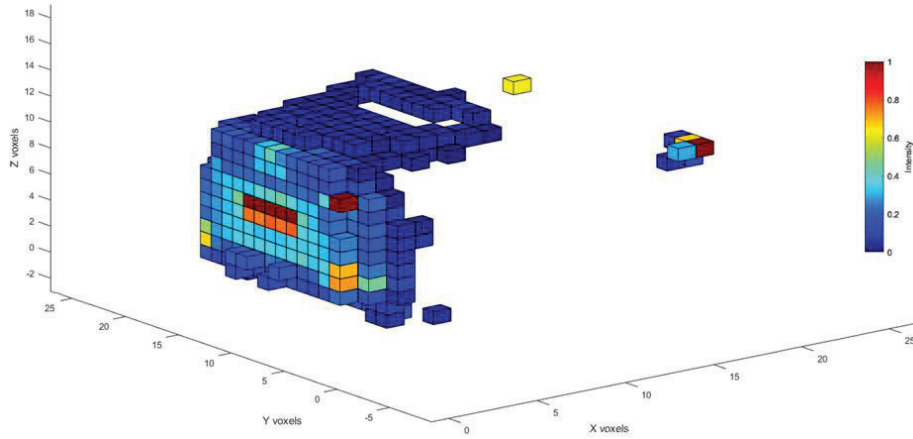


Figure 69 Soft car voxelization results for Luminar Hydra point cloud at 10m range during a linear approach.

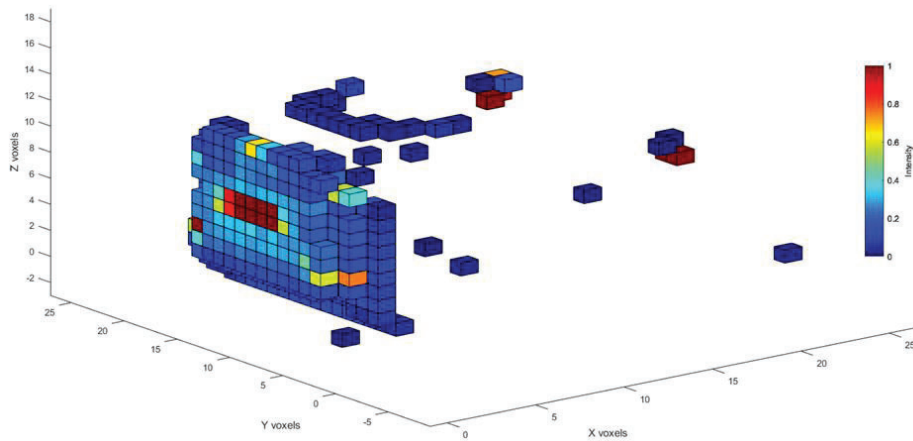


Figure 70 Soft car voxelization results for Luminar Hydra point cloud at 30m range during a linear approach.

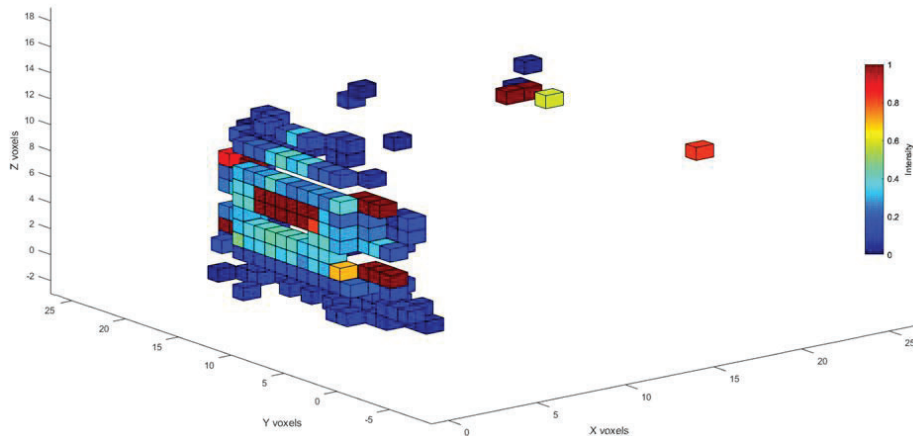


Figure 71 Soft car voxelization results for Luminar Hydra point cloud at 50m range during a linear approach.

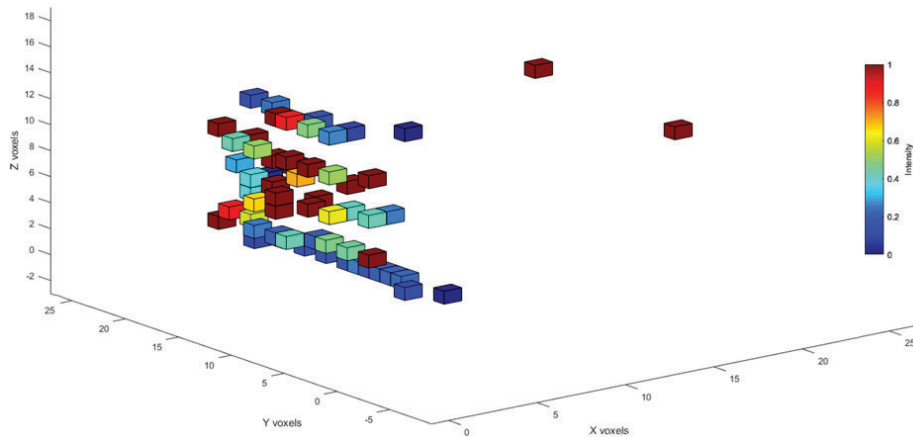


Figure 72 Soft car voxelization results for Luminar Hydra point cloud at 100m range during a linear approach.

From comparing the voxel grid outcome of the real car and soft car targets, a few characteristics can be seen that behave differently in the Luminar Hydra point cloud between the two targets. The rear shape of the soft car is flat and vertical enough to make the voxel grid resemble a flat wall with a flat roof while the real car's curved trunk and bumper makes the voxel grid contain steps between Z voxel layers.

Another noticeable difference is the hole in the voxel grid where the rear window of the real car is due to the lidar beams hitting the glass providing only a limited number of detections that are registered at the range of the window. This is not the case for the soft target since there is nothing to represent the rear window other than a different colour of the vinyl cover that comprises the soft car body and instead of the hole in the voxel grid, the rear of the target consists of a continuous layer of filled voxels.

The reflectivity of the license plate on the soft target seems very representative to the real target, especially at closer range but since the soft target's rear is more vertical and flatter than on the real car, a wide area of spectral reflections can be seen on the soft car in a radiant pattern around the license plate.

Another interesting difference are the exterior rear-view mirrors. On the real car these have relatively low reflectivity and at long range they stop providing detections all together. On the soft target however, the measured reflectivity is significantly higher and remain a high intensity detection at longer range. One explanation for this behaviour is that the real car's mirrors are angled in towards the cabin so reflected light is directed there instead of reflecting straight back towards the lidar. The mirrors are represented by reflective material on the soft car target, but the angle seems to not fully represent the angle seen in real cars. Another explanation could be that the reflective material on the soft car's mirrors gives off too much of a diffused reflection that scatters more light back towards the lidar.

Results of applying the voxelization comparison method with mean intensity per voxel on the **Ford Fiesta real target** from a linear approach with the Velodyne HDL-64 at 10m, 30m, 50m and 100m can be seen in Figure 73 to Figure 76.

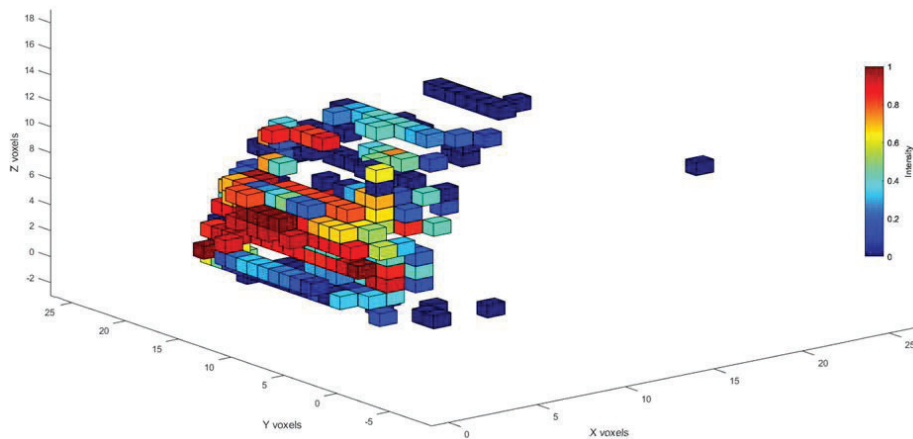


Figure 73 Real car voxelization results for Velodyne HDL-64 point cloud at 10m range during a linear approach.

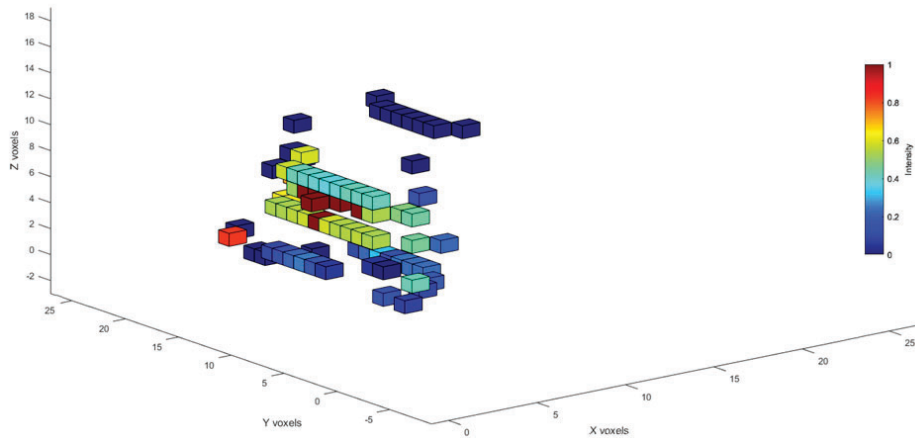


Figure 74 Real car voxelization results for Velodyne HDL-64 point cloud at 30m range during a linear approach.

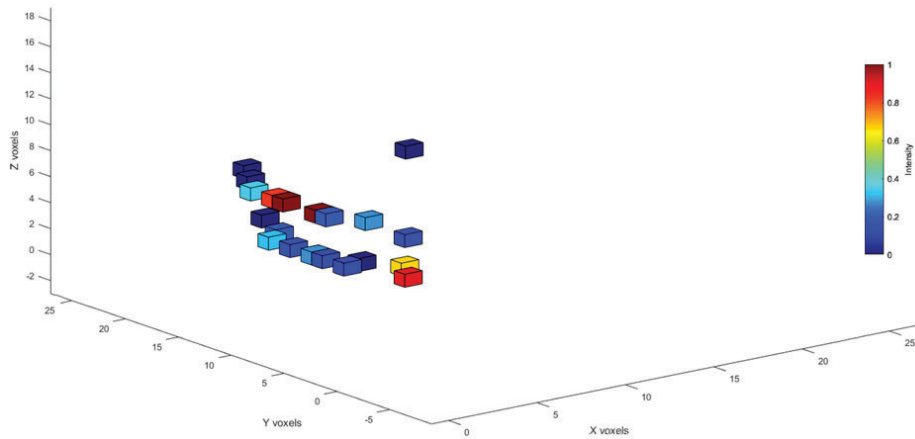


Figure 75 Real car voxelization results for Velodyne HDL-64 point cloud at 50m range during a linear approach.

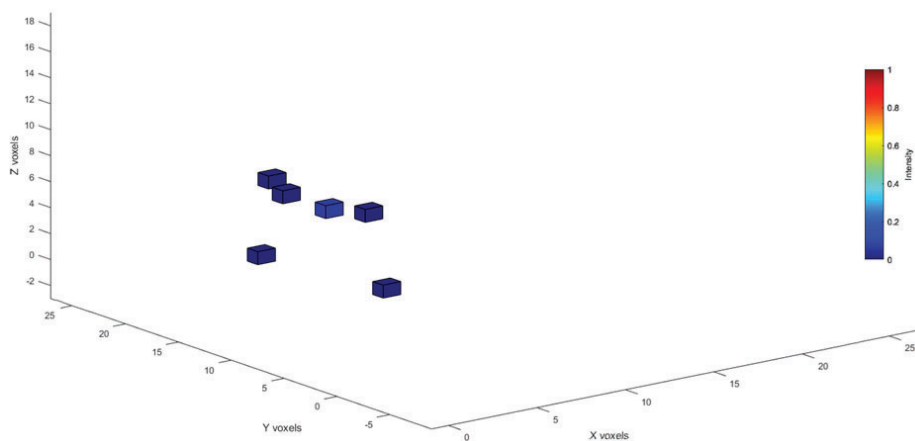


Figure 76 Real car voxelization results for Velodyne HDL-64 point cloud at 100m range during a linear approach.

Results of applying the voxelization comparison method with mean intensity per voxel on the **soft car target** from a linear approach with the Velodyne HDL-64 at 10m, 30m, 50m and 100m can be seen in Figure 77 and Figure 80.

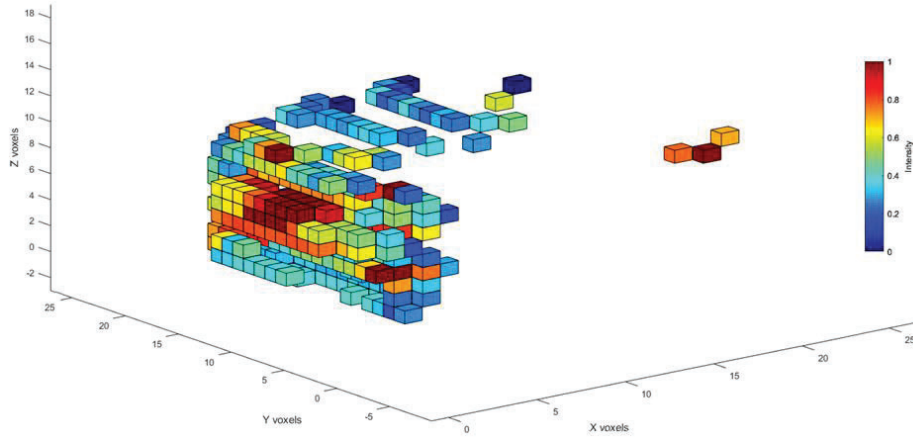


Figure 77 Soft car voxelization results for Velodyne HDL-64 point cloud at 10m range during a linear approach.

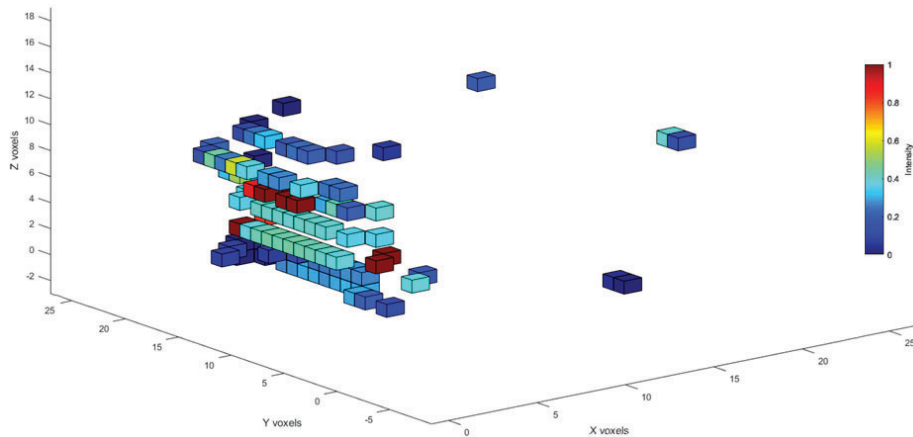


Figure 78 Soft car voxelization results for Velodyne HDL-64 point cloud at 30m range during a linear approach.

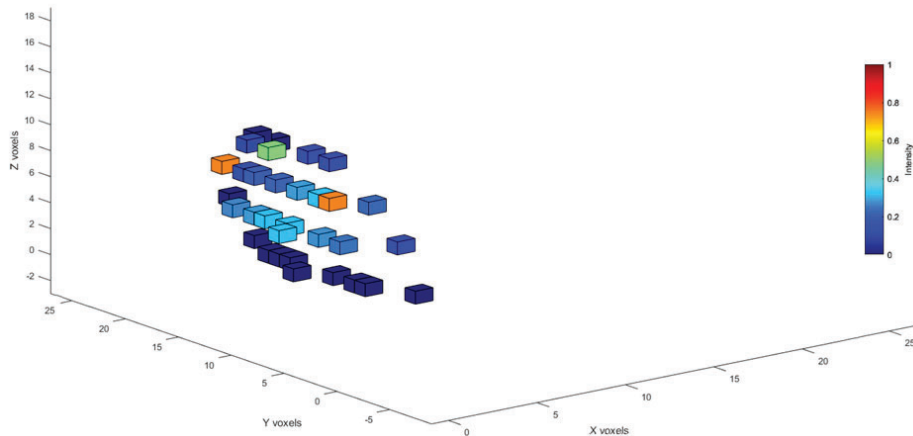


Figure 79 Soft car voxelization results for Velodyne HDL-64 point cloud at 50m range during a linear approach.

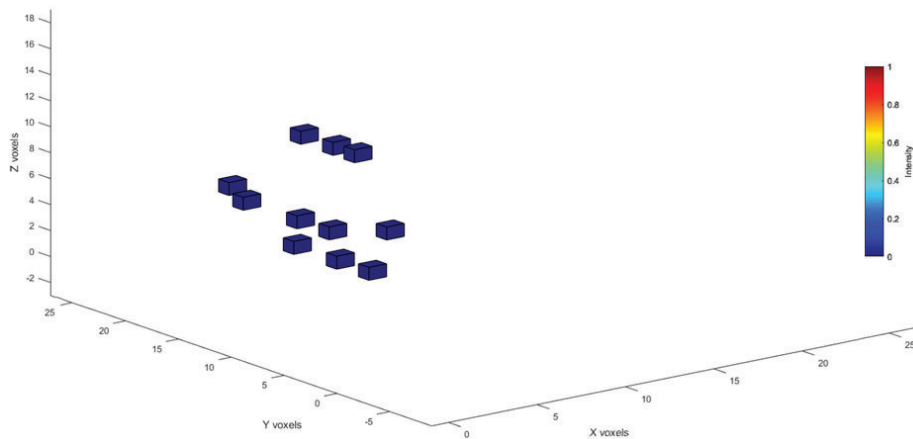


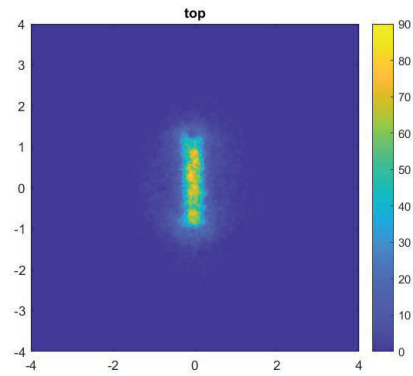
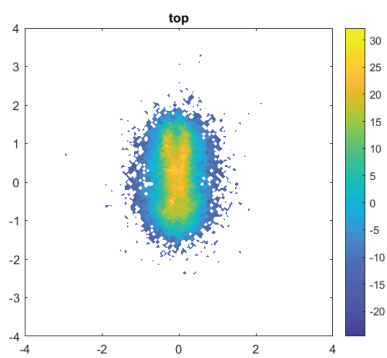
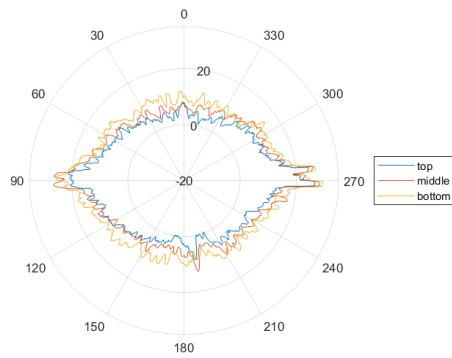
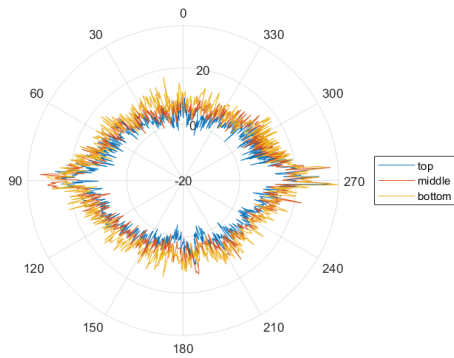
Figure 80 Soft car voxelization results for Velodyne HDL-64 point cloud at 100m range during a linear approach.

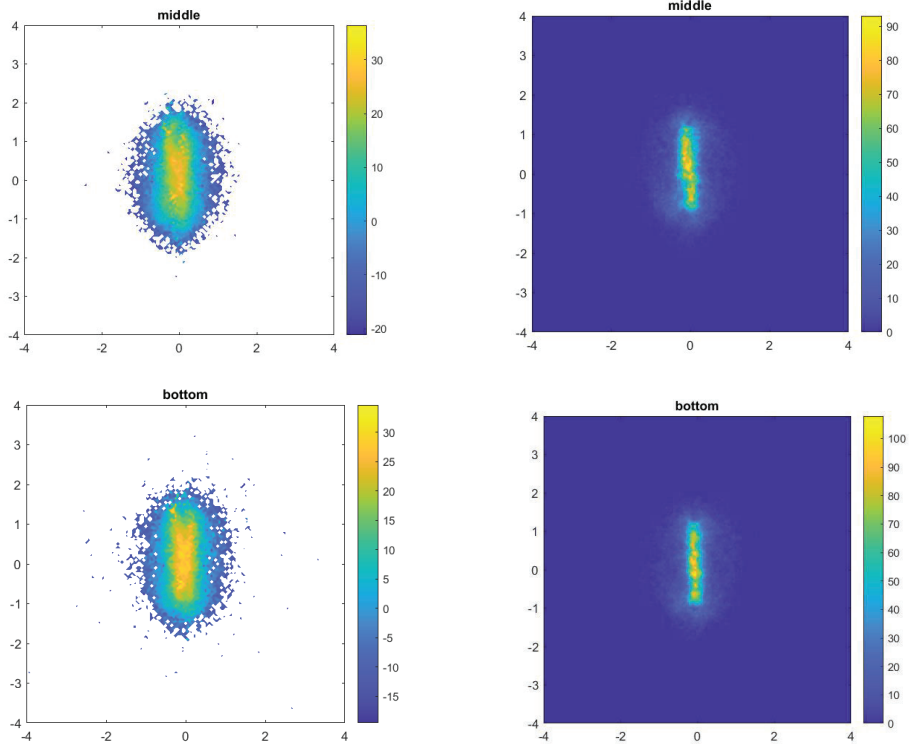
The first thing that is noticed when looking at the results of voxelization with mean intensity per voxel from the Velodyne HDL-64 data is the overall difference in dynamic range over the target surface compared to the Luminar lidar. This makes it more difficult to distinguish between different characteristics of the targets, even at close range. However, some of the same characteristic differences that are seen in the Luminar Hydra can be noticed, especially with the previous knowledge from that comparison.

This seems to indicate a downside of using this method for comparing between different lidars but more measurements with different lidars will have to be made to confirm. Using a lidar with more comparable specification to the Luminar Hydra would probably minimize the gap and allow for a more constructive comparison.

6.5.5 MC upright, leaning, and surrogate

6.5.5.1 Motorcycle – upright (15 m)

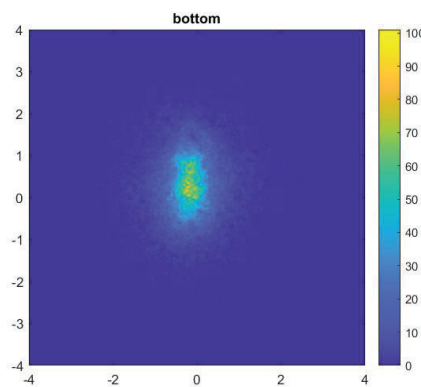
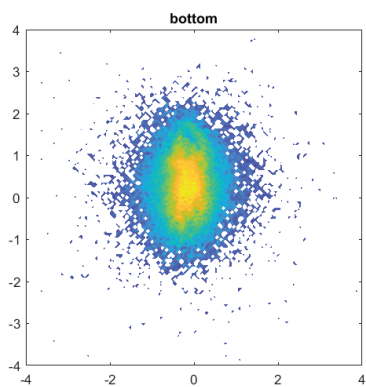
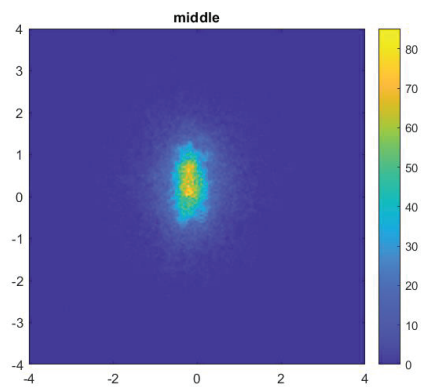
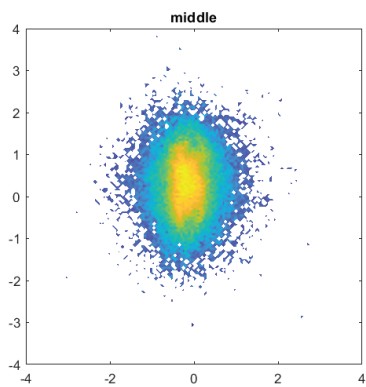
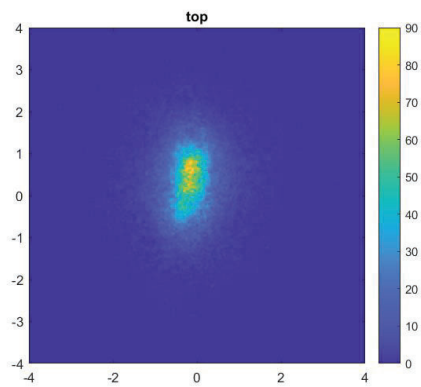
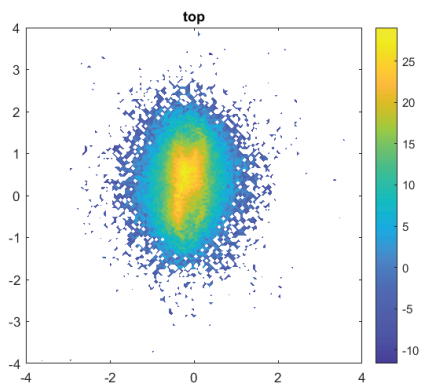
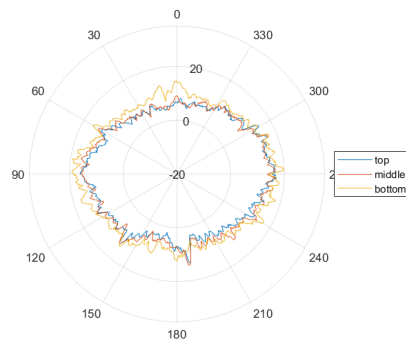
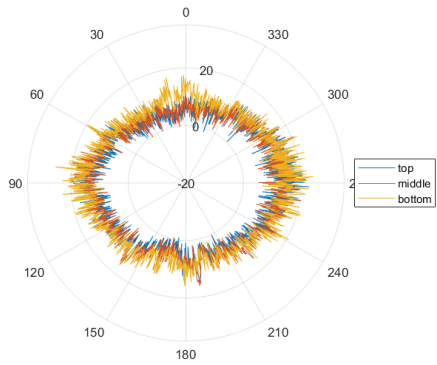




From the RCS diagrams there appears to be a slight asymmetry in the view angle as to where the peak RCS is found from the rear. It could perhaps be that this is due to the placement of the exhaust pipe. In the weighted occupancy grid the front of the target appears split into two “arms” of higher reflectivity. This is not visible in the unweighted occupancy grid, indicating that they are likely strongly reflective from only a limited number of view angles. They could perhaps be attributed to the rear-view mirrors and/or instrument panel.

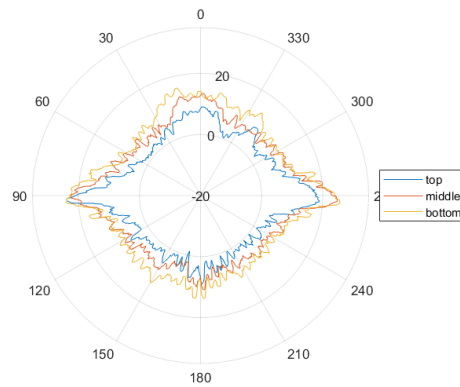
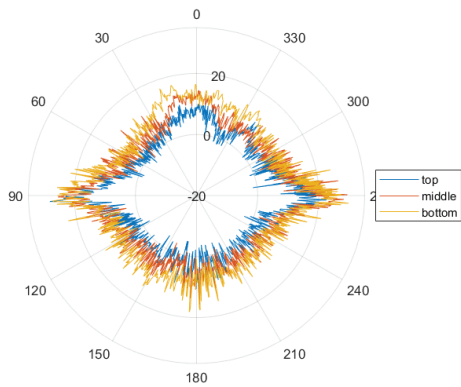
6.5.5.2 Motorcycle – leaning left (30 m)

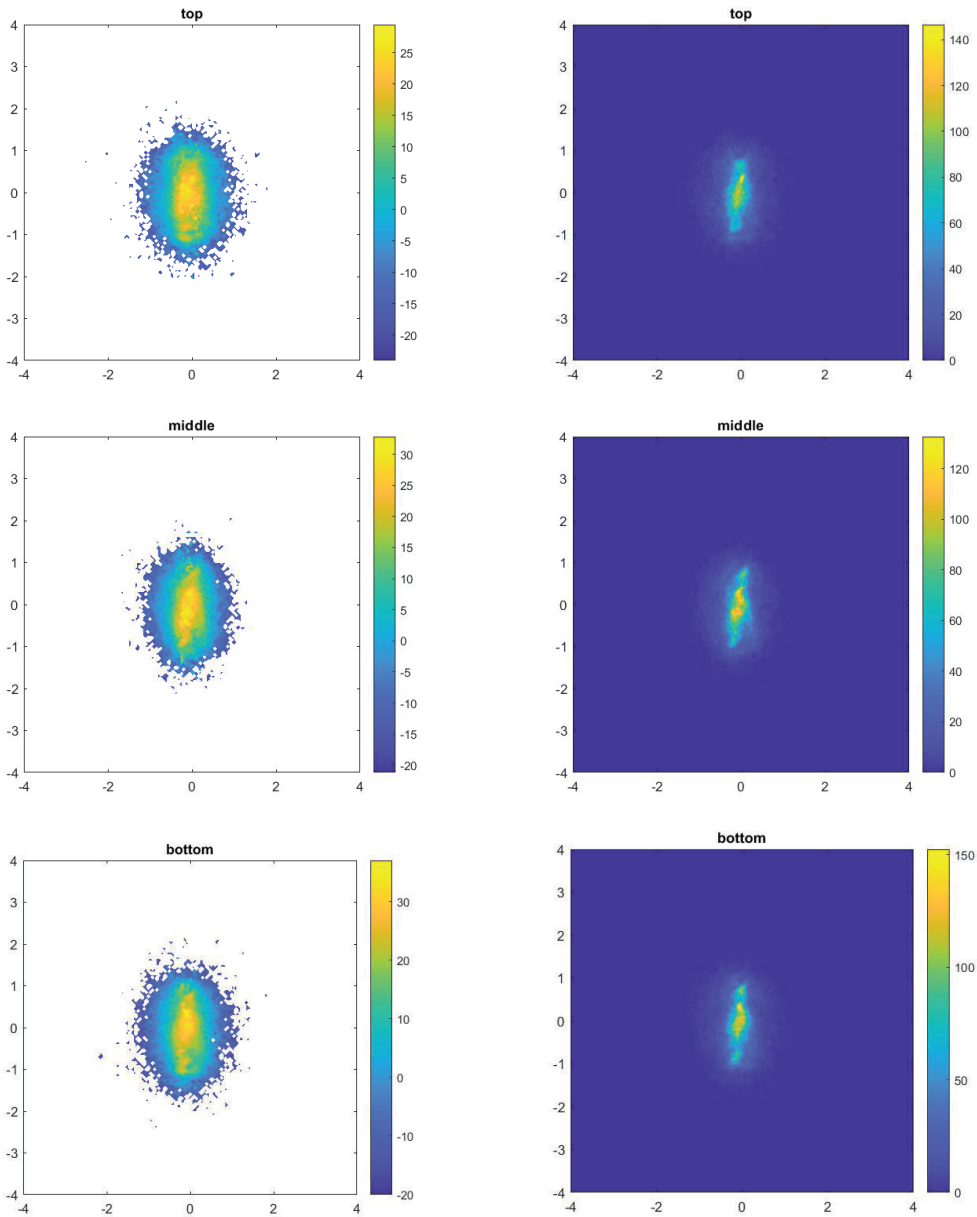




Comparing the RCS diagrams from the leaning motorcycle to the same motorcycle in an upright position it can be seen that the reflectivity when viewing the target from the sides goes down for both sides. The asymmetric feature seen at the rear, and mentioned also for the upright target, prevails.

6.5.5.3 Soft surrogate motorcycle (15 m)

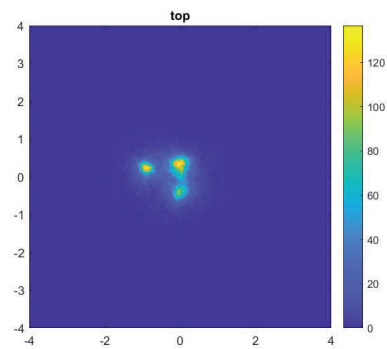
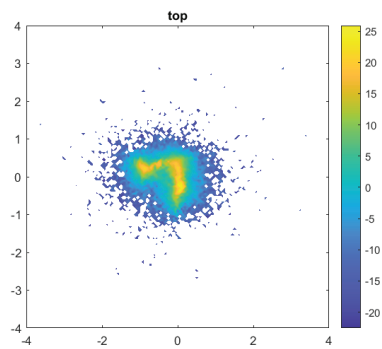
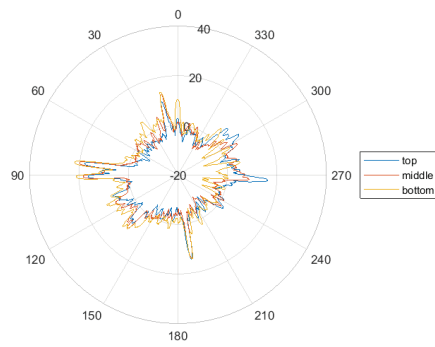
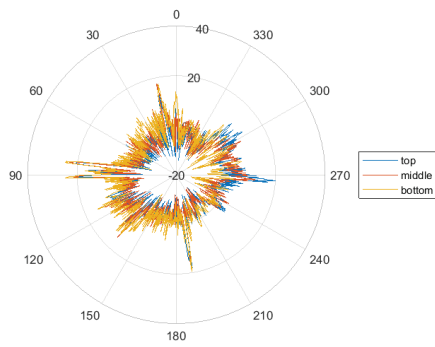


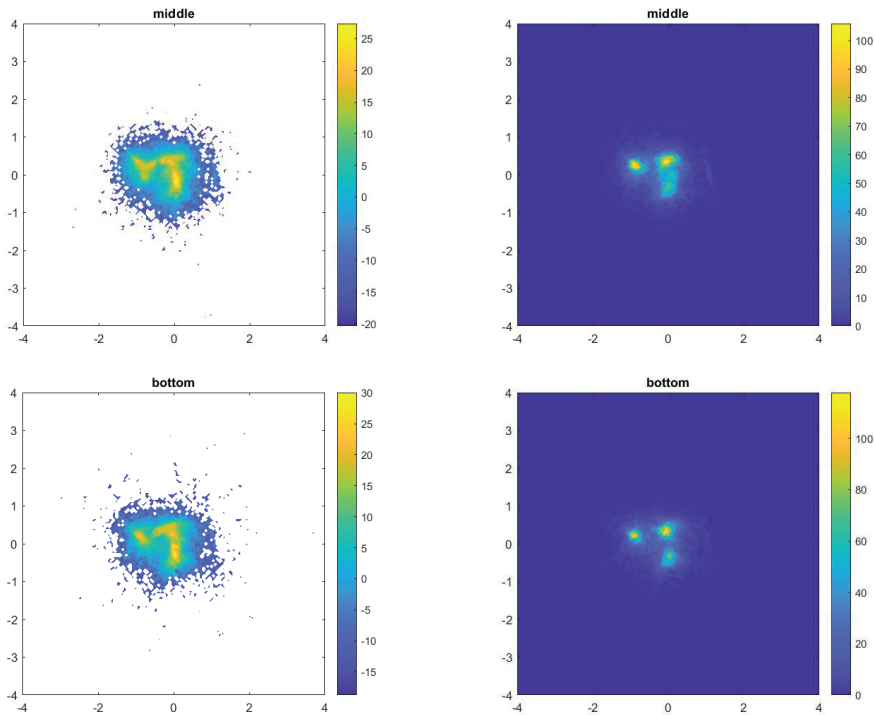


The surrogate motorcycle target appears to show similar features to the real counterpart. Without measuring more targets it is impossible to say if the differences that do exist are specific for the surrogate target or can be said to be reasonable for a general powered two wheeler type target. One possible difference is that the most common detection points appears to be focused to a smaller area for the soft surrogate target, which can be seen in the unweighted occupancy grid (right column), as a much higher maximum detection count per grid.

6.5.6 Kick-bike: standing, lying, and surrogate

6.5.6.1 Kick-bike – Lying down

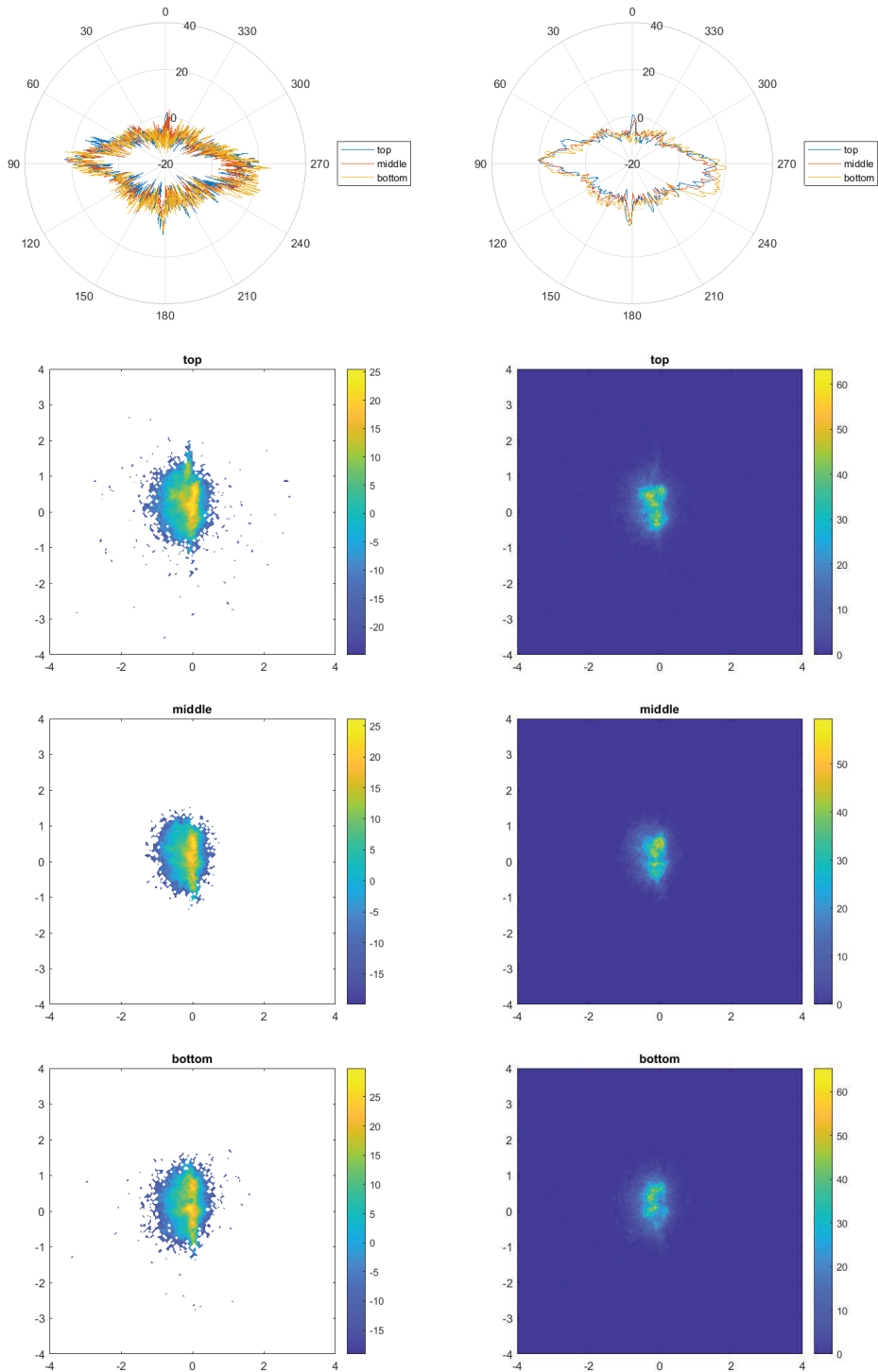




In the weighted occupancy grid figures, the entire kickbike appears reflective. The unweighted occupancy grid figures reveal areas around the handlebar, the corner front wheel area or corner between handlebar and standing platform, and the rear wheel as points visible from many directions. Judging from the RCS diagrams the visibility of the lying down scooter is very high from a small number of directions but low for most.

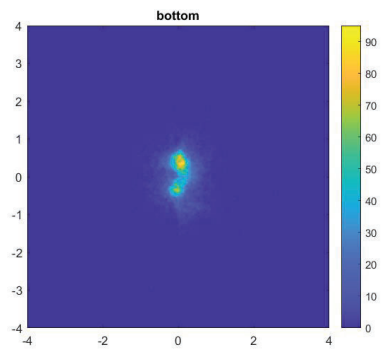
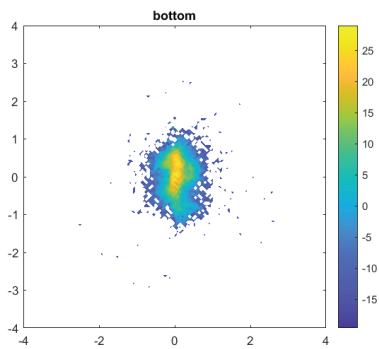
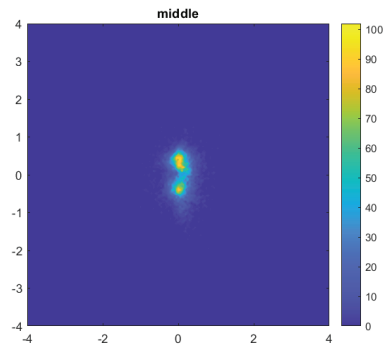
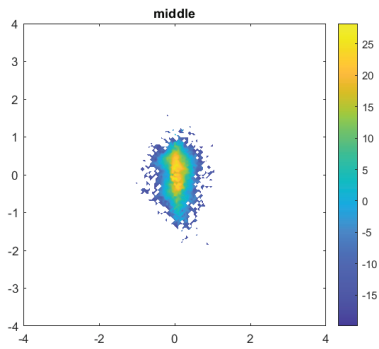
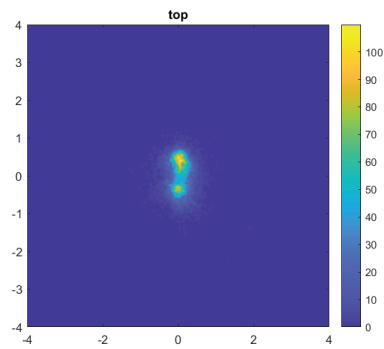
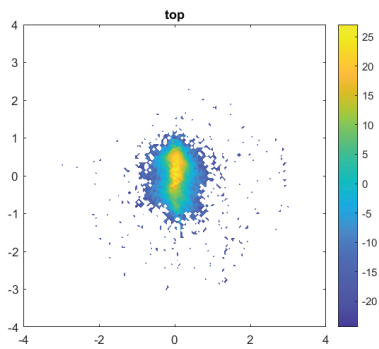
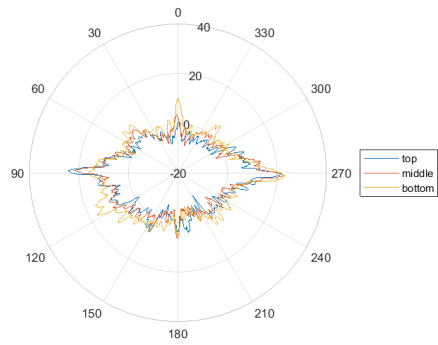
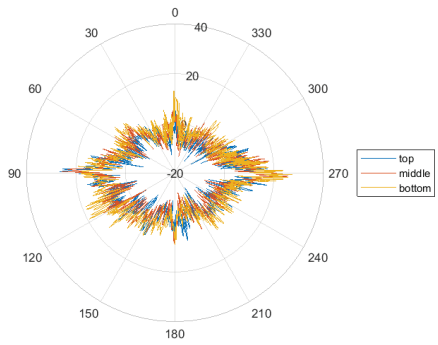
6.5.6.2 Low type of kick-bike

Target is kept standing by a small supporting wood block



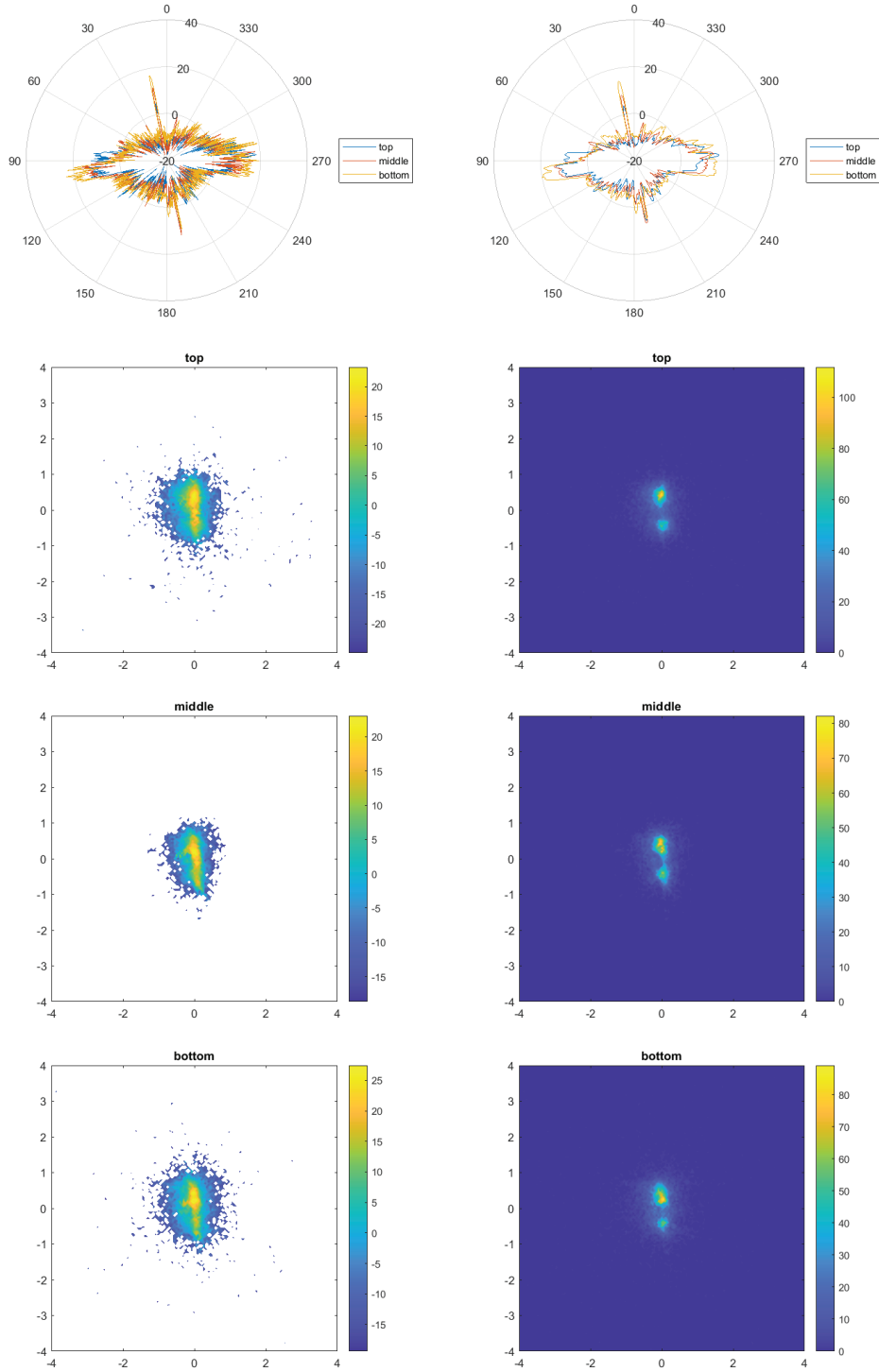
6.5.6.3 High type of kick-bike

Target is kept standing by a small supporting wood block



6.5.6.4 Surrogate kick-bike

Target is kept standing by a small supporting wood block.



All three standing scooters generate quite similar results. From the RCS diagrams it can be concluded that they can likely easily be detected if viewed from the sides. At the front and rear it may be more difficult as they show a quite narrow peak in the RCS diagrams at these directions. The occupancy grids indicate scattering centers around the rear and front. From these measurements the soft surrogate target does not appear obviously different than the two real targets measured. The scooters without rider may be interesting as targets as it is not uncommon to find similar objects parked or thrown at awkward locations. Measurements with a rider should also be of interest.

The surrogate kick-bike was made in the project “Vulnerable road users – Escooter” and the measurement of RCS was a collaboration between the two projects.

6.5.7 Exploration of miscellaneous objects

6.5.7.1 Bicycle lying

The bicycle lying down could prove to be more of a curiosity than an imposing target for the test track. It could however serve as an illustration of the detail possible to acquire with the methods used within the project.



Figure 81 A quite ordinary bicycle on the asphalt

With the bicycle lying down the RCS appears to be of a magnitude roughly comparable to that of a pedestrian.

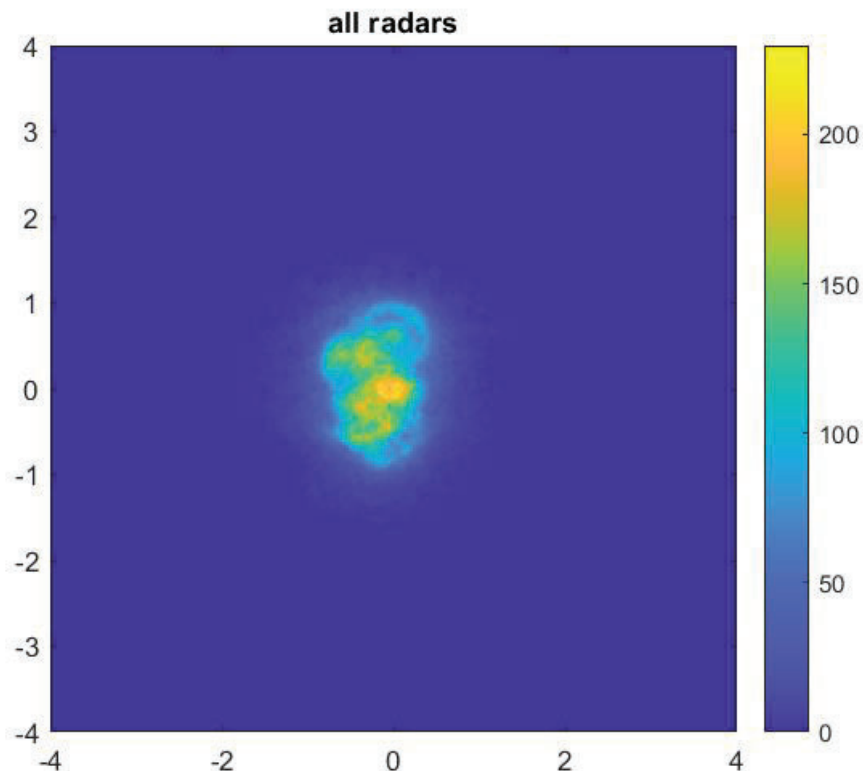


Figure 82 Occupancy grid using all radars.

Note how the wheels of the bicycle appear to be visible when inspecting the unweighted occupancy grid. A simple addition of the unweighted occupancy grids from the three radars is shown which appears to make the image of a bicycle slightly clearer. This perhaps shows how different parts of a target might end up dominating an instantaneous detection depending on the multipath effect.

6.5.7.2 Car tire

A test was made to see if it is difficult to spot a car 17-inch tire on flat asphalt. Figure 83 shows the appearance 10 m and 20 m away, where 3 seconds of data (30 scans) from the Hydra lidar has been aggregated. The height of this obstacle and the shadow should also be easy to detect, especially if the road is dry. The returned intensity of the rubbery part is about half the magnitude as that of the asphalt. The tyre used had a white sticker on the side of about 1 dm size, which made a good contrast to the rubber. The result is similar for the Velodyne VLP32C sensor.

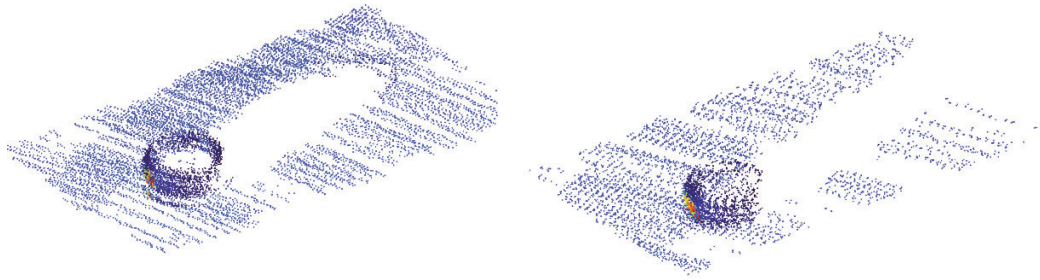
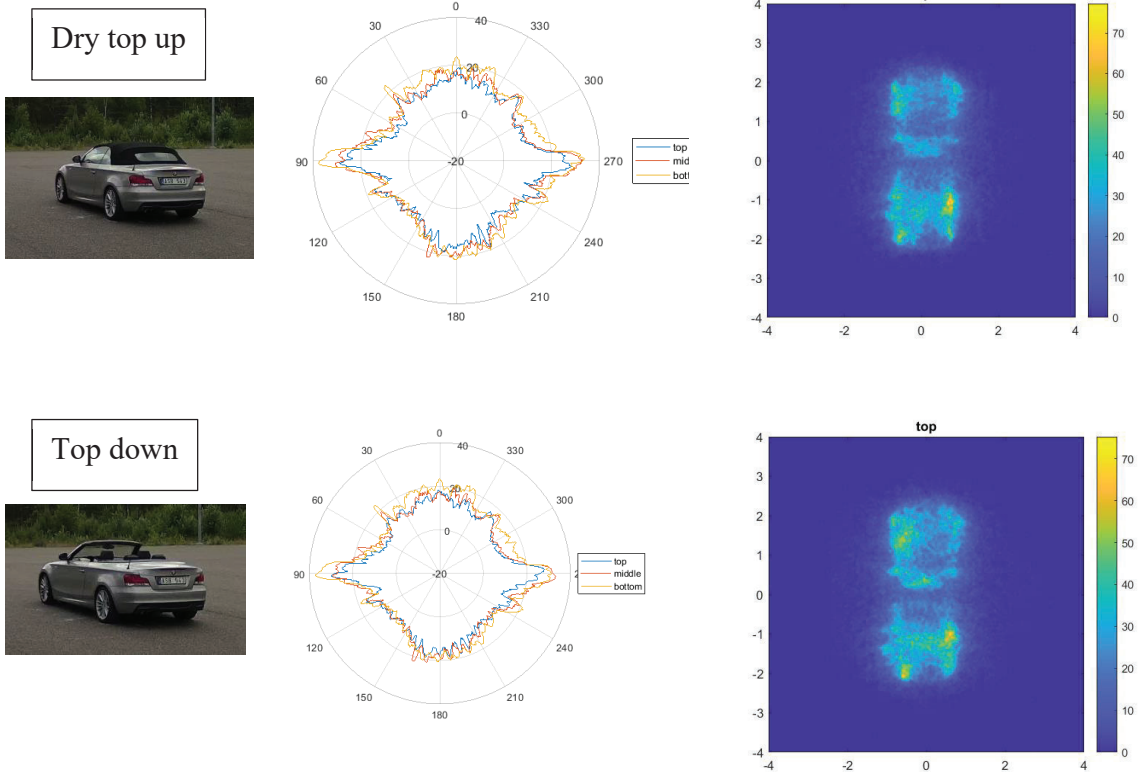
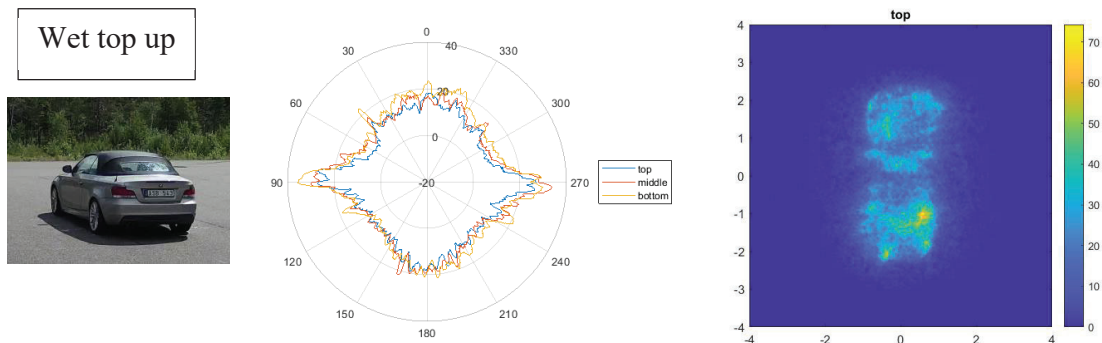


Figure 83 Tire on the road, 10 m away (left) and 20 m away (right). The sticker is clearly visible to the left.

6.5.7.3 Convertible: up, down, wet





There is no clear difference between the results with the top up and top down. It does look like the inside features of the target may appear a bit sharper when the top is down. This refers to what is suspected to be head rests and center rear view mirror. Further, there is no obvious difference between the results from when the top is dry/wet. It does look a little bit like regions with low detection frequency become fewer and/or smaller making the inside features of the target a little bit less pronounced.

The lidar return is to a not much affected by the added water on the top. From a circular pattern around the convertible, and by aggregating 900 consecutive scans to a full point cloud using the Velodyne VLP32C, a dry top was compared with a wet top. The aggregation means that same areas are viewed from different azimuth angles. A cube with 25 cm side selects a region on the fabric at either side of the rear part – this is a mainly vertical area in between the side and rear windows. The size of the cube is quite large, and the number of hits is in order of thousands. The difference is hardly noticeable in the relative number of returns or their intensity values.

6.5.7.4 Wet aerosols obscuring a plate

Water in the air between a lidar and target will be briefly discussed. There is no measure how much liquid water there is in the air. The target object is in this case a one square meter sheet with nominal 50% reflectivity and is located 18 meters away from the sensor (the sensor reports 0.45 instead of 50%). The experiment runs as follows: at time 16:45:00 water spray using a high-pressure cleaning nozzle is applied perpendicular to the sensor's line of sight. The spraying goes on for 10 seconds, trying to obscure the target as much as possible. The vehicle (sensor) is standing still. There was a slight wind, making the cloud slow drift towards the vehicle while dissolving.

For each ray in the scan, a typical time-of-flight lidar can report several detections, extracted from the time series response being an intermediate step to form a point cloud for the scan. The aerosol cloud is a non-compact object that lets through most of the rays, detecting both the cloud and objects behind it. The echoes are however dampened. The damping is typically modelled as being exponential with an extinction coefficient describing, but in this experiment we had no instrument to estimate this property.

The number of hits on the target and their average reflectivity are plotted in Figure 84 along with thumbnail pictures showing the amount of the disturbance. The number of hits is constant throughout the experiment. The reflectivity goes down from an initial value of 45 when the plate is obscured, and slowly back when the air gets clear again. An interesting point is that even though a cloud of wet aerosols is invisible on to the eye and camera, the lidar can still be used to detect its presence.

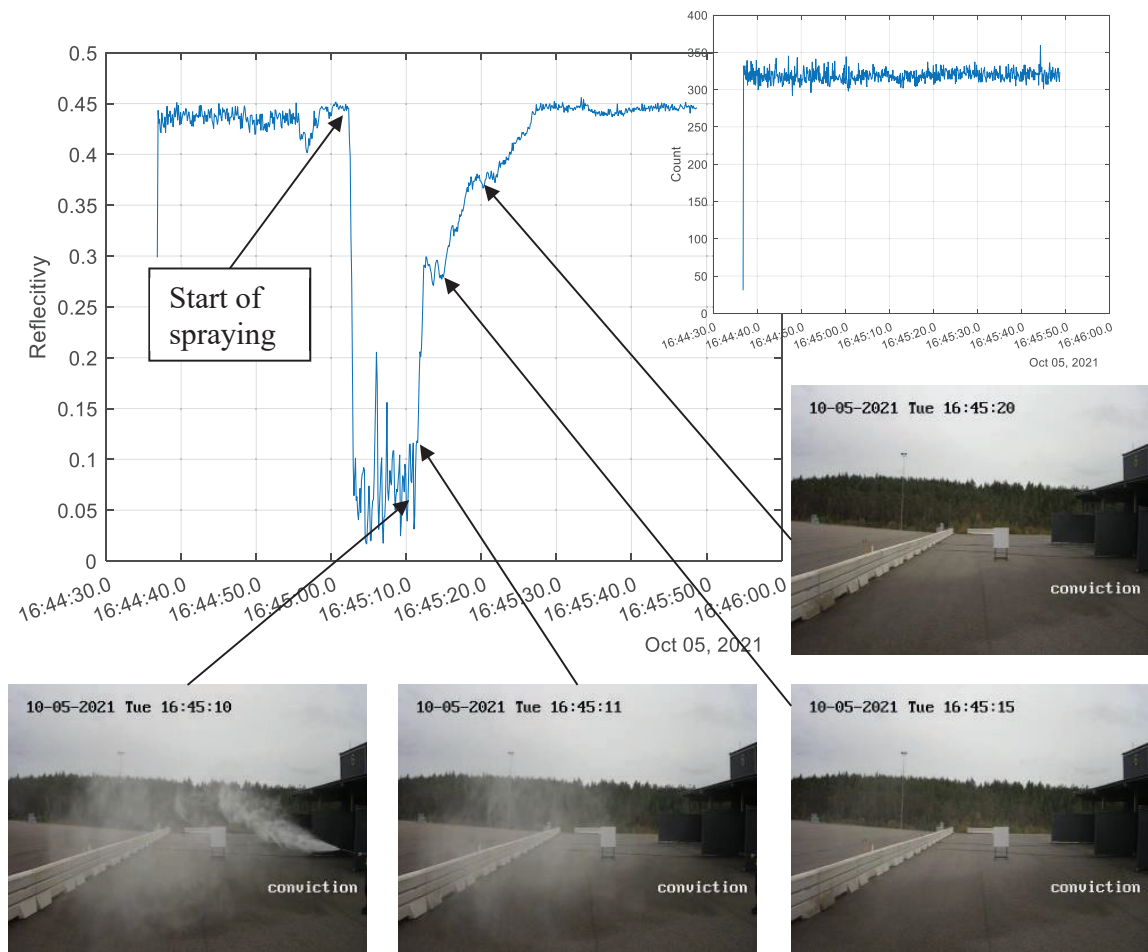


Figure 84 The wet aerosols are no longer visible for the eye but the sensor's reported reflectivity values [0 ... 1] still rises. It takes 15 seconds to reach initial value after the spray has stopped.

6.5.7.5 A black painted alu plate on the ground

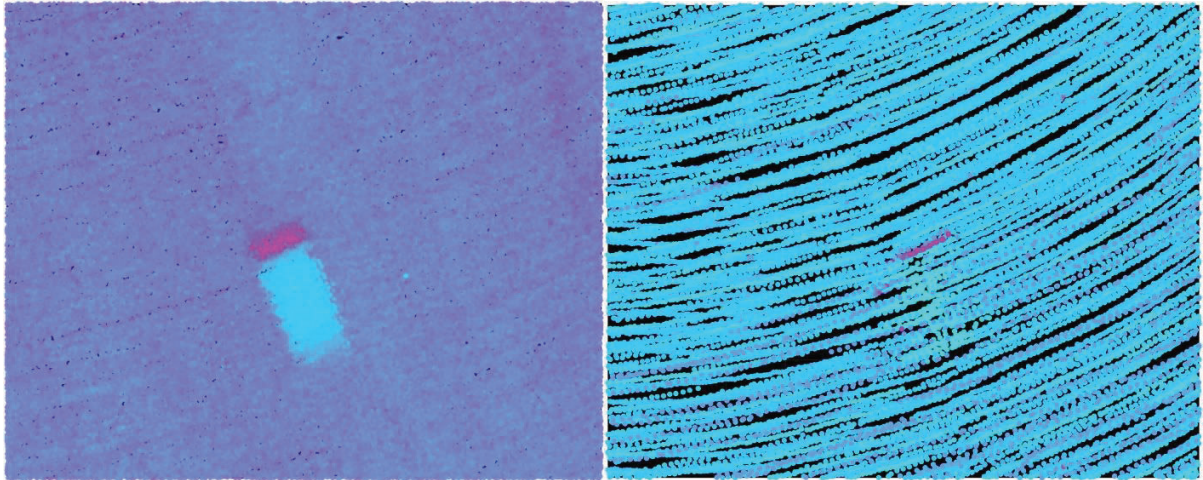
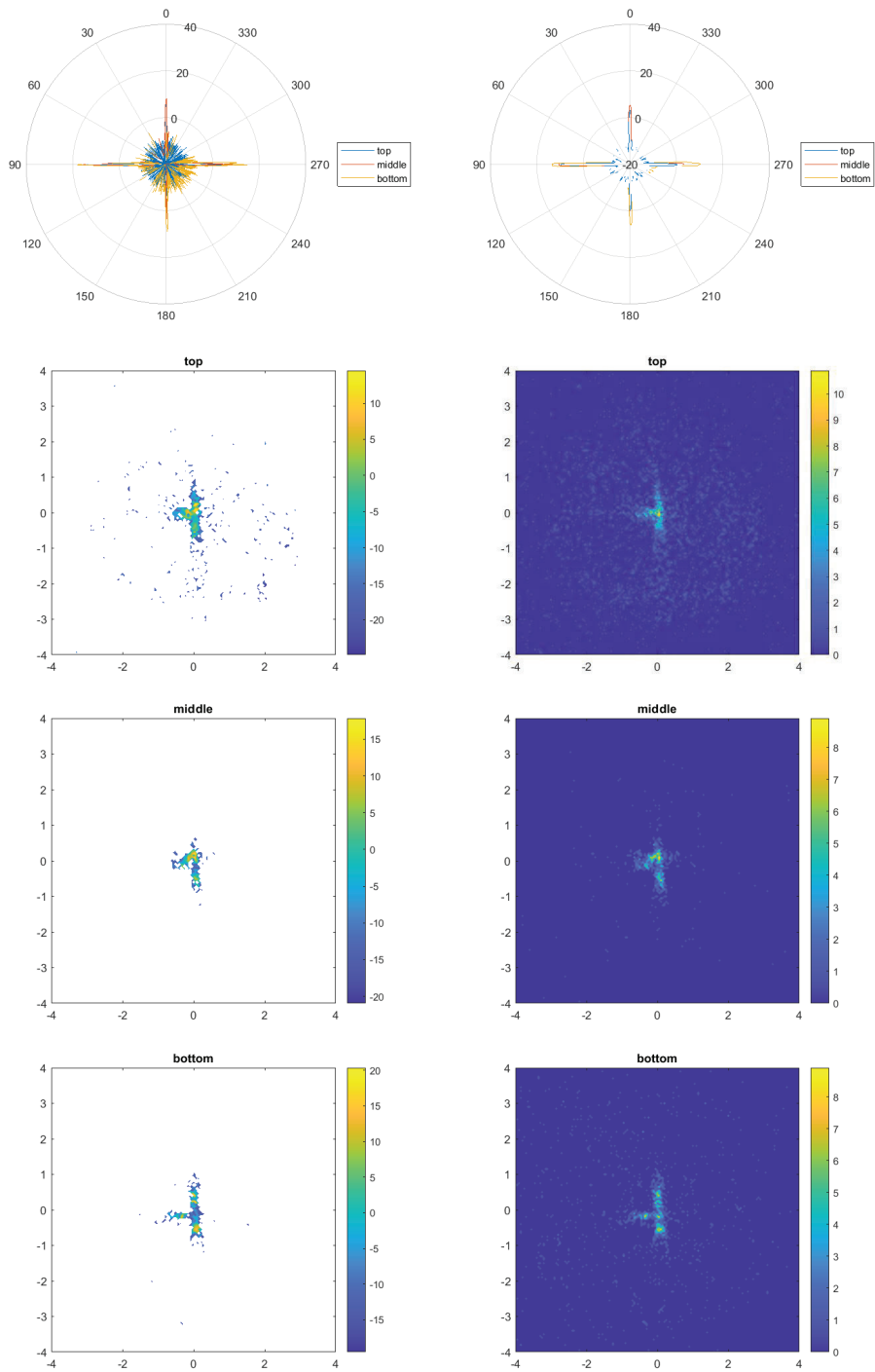


Figure 85 A black painted aluminium sheet laying on the asphalt. The travel direction of the vehicle is from top left to bottom right, along the long axis of the sheet. Left: Hydra, right: VLP32C. Intensity returned from non-painted leading edge is high (magenta), the asphalt is low (dark blue), plate itself is lower (light blue) and black means no measurement.

A test was carried out with a black painted 3 mm thick aluminium sheet, 90 cm long and a width of 50 cm. A special black colour was used, that allegedly only returns a small percentage of the light. The idea was to simulate a divergent intensity of the ground and to test the capability of the sensor. The sheet was placed flat on the asphalt and overrun by the vehicle (forward looking sensors) at walking speed. The 3 mm thick edges of the sheet were not painted. This flat object does not cast any shadow as for example the tire does. Most noticeable in Figure 85 is that both lidars pick up the edge facing the on-coming vehicle (sensor). It is also obvious that the reflectivity of the sheet is different from that of the ground, but it is still detected. The number of aggregated scans is about 90 for each sensor, while the sensor platform was moving slowly towards the object.

6.5.7.6 Supporting wood block

The wooden block used for supporting the scooters was also measured on its own.



It is difficult to rule out any impact of the wood block. It only shows an intrinsically high reflectivity at the angles attributable to being perpendicular to the flat surface of the wood block. It may still affect the measurements in other directions. When inspecting the

measurement results from the scooters however the wood block does not clearly appear in the occupancy grid figures. Still caution should be taken when drawing conclusions.

Another interesting note is how clearly the method of using all parts of the signal above threshold introduces some errors as the signal spills into neighbouring bins giving the illusion of cross like features of the block. The risk of this happening should be remembered when performing analysis and drawing conclusions. In all occupancy grid figures presented here there can be seen some form of halo or glow around the actual target, which may likely not be due to the target but rather an effect of our treatment of the data.

7. Dissemination and publications

The CONVICTION project has cooperated with the FFI project “Vulnerable road users - Escooter”, diary number 2020-02959, led by AstaZero, ending in September 2021. The collaboration was to measure the RCS of a kick-bike and its soft surrogate target.

7.1 Final event

The final event of the CONVICTION project was announced in spring 2022 and held May 24 at the generally open Volvohallen at Volvo Cars premises. In total there were 40 guests of which a dozen belonged to the project itself. The speeches were also followed by about 15 people on-line. Every partner took the chance to speak about their main activities and achievements in the project. We covered all topics worked upon in the project, from radar antennas to optics simulation.



Figure 86 Final event seminar.

Besides the speeches, on display were four demo stations with equipment for people attending on-site to pay visit to during the breaks. UniqueSec demoed one of their HIL setups with frontend and radar. Veoneer demoed their moving platform with all sensors mounted. RISE showed the spectrometer measurement system. ESI showed their simulation software with a relevant Euro NCAP scenario.

The schedule of the seminar was quite dense during the three hours and the event seemed to be much appreciated.

7.2 Dissemination

How are the project results planned to be used and disseminated?	Mark with X	Comment
Increase knowledge in the field	X	There have been several areas of interest, to mention just one, it is interesting to learn from optics analysis and simulation how water affects the lidar.
Be passed on to other advanced technological development projects	X	The logging equipment built will be used in succeeding projects
Be passed on to product development projects	X	Data from sensors has been passed to verify sensor simulation model and target.
Introduced on the market	X	Improvements of the simulator worked on in the project is planned to be introduced on the market
Used in investigations / regulatory / licensing / political decisions	X	There is an interest group for soft targets, to which knowledge from the project will prove very useful in the standardization discussions.

7.3 Publications

The following paper has been written and will be submitted for publication.

Title: Over-the-Air Automotive Radars Hardware-in-Loop Test for Development and Validation of Active Safety Systems and Autonomous Cars

Abstract: Due to the development of new radar technology for advanced driver-assistance systems (ADAS) and automated driving (AD) applications, testing radars in real world situations is highly desirable. Testing autonomous driving functions on public roads can be dangerous and is not reproducible. In this paper, we present a novel Over-the-Air (OTA) Hardware-in-Loop (HIL) radar target simulator for testing radars. The complete configuration with hardware and software implementation will be presented in this article. We illustrate test procedures by creating Euro NCAP scenarios and explain the benefits and importance of real-time HIL testing of automotive radars.

8. Conclusions and future research

This section summarizes the work and results in CONVICTION, discusses a few difficulties encountered during the project and ends with a set of ideas for future work.

In the CONVICTION project we have worked with a set of the tools for verification and validation of driver automation: investigation of soft targets, scenario simulation with high fidelity sensor models, and HIL simulation. It is necessary to make sure the models are sufficiently representative for the V&V to be efficient and adequate. The focus has been on the lidar and radar sensors.

The project has systematically and successfully worked towards its goals. Rigs for collecting data from lidar and radar have been built. A set of typical test track surrogates have been compared to their counterparts. Analysis methods have been suggested and used to show the difference between real objects and soft surrogate models. Sensor simulation models have been improved and verified. Radar HIL has been connected to scenario-based simulation and verified against simulation and logging at AstaZero. We have analysed and simulated how typical disturbances – rain and fog – impact on lidar output. This is the right way to proceed to improve efficiency of V&V.

An interesting finding for the motorcycle target is that the peak RCS towards the sides goes down when the motorcycle is leaning. This means that a turning thus leaning motorcycle may be more difficult to detect. This should have a correspondance in the soft surrogate targets, which we believe not to be the present case.

The radar characterization identified the corners and wheelhouses of a car as important scattering centres, while the surface and rear axis appear to be the strongest reflectors. The surface is the strongest reflector also for the surrogate target, but the inside structural skeleton appears as scattering centres for the surrogate car target. We also saw indications of how important it could be to make sure the target is properly mounted.

It has been found that the RCS of a convertible car with a soft roof does not change very much when the roof is down or when it is wet. For a lidar at close range, the difference in intensity (and number of recorded hits) between a dry or a wet soft roof is very small.

A couple of black objects of low reflectivity has been tested flat on the asphalt. Neither a car tire without rim nor a thin slate of aluminium were possible to detect by the lidars used.

In collaboration with the project “Vulnerable road users – Escooter”, a soft kick-bike was compared to real ones, both standing and lying. It was concluded that the RCS and heatmaps are quite similar. The kick-bikes have been evaluated without a driver.

For the car soft target the effect of multiple returns from within the target, found for an older revisions of the target and with the previous characterization method, was not seen during this project. Further investigations are needed conclude if this is an effect of the new target revision or the new method.

The surrogate motorcycle target appears to show similar features to the real counterpart. One possible difference is that the most common detection points appear to be focused to a smaller area for the soft surrogate target, which can be seen as a much higher maximum detection count per grid.

Rain, fog, and water droplets on the target all have a significant impact on the lidar signal. The impact has been studied by deriving equations from a physical model. Water droplets are effective scatterers both in the atmosphere and on the target. Fog is the most impairing condition for a lidar (using a wavelength of 905 nm). Operating in thick fog will 'completely kill' the signal at 100 m range. In relation to fog, rain is not as limiting. However, very heavy rain will still significantly reduce the detection lidar power by approximately 50%. The wetting of the target (water film and water droplets) has a significant impact on the lidar signal, but it is weaker than fog and rain in the most common scenarios. For a target that is mostly reflecting diffusely, a water film will introduce a specular component that will be orders of magnitude higher than the diffuse component. In the conducted study, the diffuse part decreased by 5% depending on the specifics of the scenario. Droplets acts as scattering centers for most of the lidar beam, but a small portion will be reflected back straight into the detector. The latter will add to the power in the detector, but the effect is often small, on the order of 1%. There are many parameter dependencies, and it is not appropriate to draw general definitive conclusions.

Ray tracing simulations have been performed using Zemax OpticStudio for lacquer, cloth, and soft plastic. Parameter variations were tilt angle, wetting ratio and droplet radius. A general conclusion is that water droplets change the lidar response by effectively scattering the rays in all directions. The size of the water drops is effectively varying the scattering divergence angle and in effect the amount of reflected specular light. For a lidar the diffuse scattering of the light is probably the most important parameter. The results show that diffuse scattering is not affected very much by water drops on the target, the loss is on the order of a few percent. It should be noted that the simulations are much more detailed in scope than the mathematical model and some details are not fully captured in the mathematical model. However, the general behavior seen in the results of the ray tracing simulations corresponds well with the mathematical model.

The lidar sensor models in PROSIVIC help us to simulate the target reflectivity and laser energy attenuation with a disturbance of the airborne particles. In addition, the sensor model provides a synthetic data of noise issued from rain fog which can be injected into post-processing or artificial intelligence algorithms. The use of a scenario-based simulation platform allows to decrease the number of kilometres necessary to travel in the

real world to evaluate a system in critical scenarios integrating degradations of infrastructure, weather conditions, sensors, and algorithms. It ensures the repeatability and reproducibility of driving conditions and equipment.

Over-the-air radar HIL testing using ASGARD1 enables validation of radar-based ADAS/ADS. It gives several advantages. First, by providing capability of testing radars with different performance under the same conditions/or testing different radars under the same conditions. Second, access to ground truth from PROSIVIC and thus capability of analysis of radar performance. Third, testing radars with real-world conditions by running HIL radar simulation and comparing the results with the real-world measurements and simulations. Finally, capability of recording data from radar synchronized with time stamps come from PROSIVIC to make accuracy analysis possible. With this setup, we can test richer and more complicated scenarios with multiple targets. At the end we demonstrated and analysed the results of radar simulation with CPNC scenario for different speeds of ego vehicle. These test cases were clearly showing the effect of ego vehicle's speed and radar performance for detecting the child. The child can be detected by the radar at low speed, but when the speed is increasing it becomes more challenging to detect the child well in advance. The higher the speed, the child either is occluded or partially confused by another target (the parked car) and therefore the radar is less capable of detecting child. Moreover, with the proposed radar HIL test, we can score different radars under the same conditions for a specific scenario or use case.

From comparing the voxel grid outcome of the real car and soft car targets, a few characteristics can be seen in the point cloud comparing the soft and real target. The rear shape of the soft car is flat and vertical enough to make the voxel grid resemble a flat wall with a flat roof while the real car's curved trunk and bumper makes the voxel grid contain steps. Another difference is the hole in the voxel grid where the rear window of the real car is due to the lidar beams hitting the glass providing only a limited number of detections that are registered at the range of the window. This is not the case for the soft target since there is nothing to represent the rear window other than a different colour of its vinyl cover. Another interesting difference are the exterior rear-view mirrors. On the real car these have relatively low reflectivity and at long range they stop providing detections all together. On the soft target however, the measured reflectivity is significantly higher and remain a high intensity detection at longer range. The reflectivity of the license plate on the soft target seems very representative to the real target, especially at closer range.

The output from the sensors is used by the perception. A major difficulty when comparing objects (e.g. a soft and a real target) or two sensors are the unknown "performance" of the perception module used by the intended application. The perception can be thought of set of software features such as classification of objects, tracking of objects, etc. In this project we treat perception as a black box. In the project there is no specific perception included, which means that nothing represents the user which ultimately must be the judge of how well objects and environments are modelled. An

alternative is to describe the quality of the sensor data entering the perception. To some extent this is straight forward, for example by the signal-to-noise ratio, or the resolution. However, it is still necessary to know what is important for the perception.

One thing that is noticed when looking at the results of voxelization with mean intensity per voxel from the Velodyne HDL-64 data is the overall difference in dynamic range over the target surface compared to the Luminar lidar. This makes it difficult to distinguish between different characteristics of the targets, even at close range. It seems to indicate a downside of using this method for comparing different lidars but more measurements with different lidars will have to be made to confirm.

Another approach is to apply a well-known or at least an openly available perception function to let that represent a user of sensor data. The perception is now a model, a simplification. If the implementation or training set are similar to the vehicle-under-test's perception, it could help point what direction to continue with further analysis. It is similar to benchmarking typically seen in research papers. The approach of modelling the perception has been used in the project for comparing soft and real vehicles at different distances and angles.

A continuation of the work in the CONVICTION project could follow along the lines suggested in the following.

Continued work on the data using the circular characterization method used at the test track could include identifying specific intervals of view angles for deeper analysis. Development of model targets consisting of multiple scattering centers for traffic simulators or similar should also be an interesting track.

New radar technology with high resolution output, including good resolution in both azimuth and elevation angles effectively delivering a point cloud to the perception will most probably enter the market, see for example the radars from Arbe [2] or the open dataset from Delft [3]. The higher resolution provides more detailed and data intense input to the perception. This is in contrast to traditional automotive radar which embedded perception renders a list of objects. Apart from the doppler dimension, the tools and neural networks for lidars are close at hand, changing the way sensor fusion is made to become more centrally located in the vehicle.

Another topic to continue with, is development and verification of a more detailed radar simulation model. The type of simulation model used in the project was based on placing an object's RCS at some position of the object. This is often a large simplification compared to the needs. A more detailed simulation would be to model propagation of electromagnetic waves, although with simplifications to keep computational cost at bay. Then it will also be of interest to compare the two approaches with each other and verify with real data. In general, more complex scenarios should run in simulation, e.g. varying different configurations, using dynamic objects, etc.

The literature study on lidar in adverse weather shows that a lot of work that has been undertaken regarding atmospheric attenuation. Many of the characteristics, properties and limitations of various conditions are well-known. While atmospheric properties and the resulting signal attenuation is well understood, little has been done on wet targets. The reports on wet targets are sparse and the field is basically an uncharted territory and more research in this area is needed. It would be useful to include more atmospheric and target reflection conditions into the model. For example, snow and ice but also a more elaborate description of water drop scattering would make the library of models more complete and more accurate. Another interesting future development would be to consider the impact of adverse weather temporal response with the current model as a basis.

A spin-off from the CONVICTION project is the FFI pre-study project “Dimhöljt” (2021-02582) by RISE and Veoneer [32]. The pre-study ended successfully in June 2022. The aim was to take a first step of generating and measuring fog in a climate chamber, exploring methods and feasibility of lidar testing in fog, and exploring the possibility of using lidar for weather classification. The idea is to offer a tool for testing sensors and perception both for development and verification. A conclusion is that a suitable location would be a moist about 200 m long corridor with multiple lanes protected from wind and the sun.

During last year an initiative for standardization of automotive lidar performance, ISO/PWI 13228, has been taken [4]. The idea is to provide a universal description for lidar performance to allow for comparisons of sensors. The idea is also to standardize test methods with respect to perception performance and reliability. Most probably, water-based disturbances will be discussed within the initiative and that will be an interesting development to follow.

More effort needs to be spent in the analysis of data. This is true both for lidar data comparison and radar performance analysis. A fundamental task is to compare two similar data structures coming from a sensor, for example two signals, two images or two point-clouds. They could for example have been captured at different disturbance magnitude or be the real object versus its surrogate model. What is the difference? The difference is not simply the data points in one of the structures versus data points similarly located in the other structure. There can be differences in many dimensions. A common approach is to identify features, either by engineering principles or by an automated process. In general, a comparison is non-trivial. In many cases the resort is to visualize the differences.

The CONVICTION project did not put any weight on analysing the response of ADS or ADAS functions, but instead aimed to create better conditions for other projects to do this. The methods used to characterize the targets put more focus on high sample density and less on dynamic conditions than would be expected in a traffic scenario. This leaves room for improvement. Various metrics to qualify sensors, post-processing and data-fusion algorithm would be studied to provide objective comparative measurements. The

goal of this study will be to assess the level of representativeness of simulated data and the capability of tested sensors.

To overcome the black box nature of automotive perception, some software features of perception might be possible to compile into an open toolbox accessible for non-profit benchmarking, that is, for research and education. A toolbox would then offer reference implementations of different features. A well-known example in another domain, computer vision, is the OpenCV toolbox [5] which in recent year has grown much on its AI part. An answer might be the ROS linux middleware [6], which is an eco-system for more general robotics research also extensively used by enterprises in the automotive industry. Much of the value of ROS lies in the community where it is possible to find packages with application related code that uses ROS client libraries.

9. Participating parties and contact persons

Organization	Contact person
RISE	Martin Sanfridson, (at ri and se)
Volvo Cars	Elías Marel (at volvocars and com)
Veoneer	Rustem Elezovic (at veoneer and com)
ESI Nordic	Jonas Fredriksson (at esi-group and com)
Asta Zero	Jesper Ekstener (at astazero and com)
UniqueSec	Toktam Bagheri (at uniquesec and com)

Material for this report has been produced by all participating persons, many of which are not mentioned in the table above. Material also comes from consulting firm Entangly via Volvo Cars. Editor has been project leader Martin Sanfridson.

10. Abbreviations

Abbreviation	Description
ADS	Autonomous Drive System
ADAS	Advanced Driver Assistance Systems
ASGARD1	Radar Target Emulator from UniqueSec
EM	Electro-Magnetic
HIL	Hardware-in-the-Loop
Lidar	Light Detection And Ranging
NIR	Near Infra Red
PROSIVIC	Simulation tool from ESI
Radar	Radio Detection And Ranging
RCS	Radar Cross Section
RF	Radio Frequency
ROS	Robot Operating System
SAE	Society of automotive engineers
TOF	Time Of Flight
VIL	Vehicle-in-the-Loop
V&V	Verification and validation

11. References

- [1] <https://www.sae.org/blog/sae-j3016-update>, accessed August 2022
- [2] <https://arberobotics.com/>, accessed August 2022
- [3] A. Palffy et al., “Multi-Class Road User Detection With 3+1D Radar in the View-of-Delft Dataset”, IEEE Robotics and application letter, Vol. 7, No. 2, April 2022
- [4] <https://www.automotivetestingtechnologyinternational.com/news/cavs/hesai-heads-up-lidar-iso-test-method-working-group.html>, accessed August 2022
- [5] <https://opencv.org/>, accessed August 2022
- [6] <https://www.ros.org/>, accessed August 2022
- [7] <https://www.euroncap.com/en/for-engineers/protocols/vulnerable-road-user-vru-protection/>
- [8] <https://www.esi-group.com/products/virtual-systems-controls>
- [9] <https://www.zemax.com/>
- [10] DENSE, “D2.1 Characteristics of Adverse Weather Conditions”, <https://www.dense247.eu>, accessed August 2022
- [11] Palmer, James M., and Barbara G. Grant. 2010. *The Art of Radiometry*. Bellingham, Wash: SPIE Press.
- [12] Steinvall, Ove. 2000. “Effects of Target Shape and Reflection on Laser Radar Cross Sections.” *Appl. Opt.* 39 (24): 4381. <https://doi.org/10.1364/AO.39.004381>.
- [13] Ginneken, Bram van, Marigo Stavridi, and Jan J. Koenderink. 1998. “Diffuse and Specular Reflectance from Rough Surfaces.” *Appl. Opt.* 37 (1): 130. <https://doi.org/10.1364/AO.37.000130>.
- [14] Wandinger, Ulla. 2005. “Introduction to Lidar.” In *Lidar*, edited by Claus Weitkamp, 102:1–18. Springer Series in Optical Sciences. New York: Springer-Verlag. https://doi.org/10.1007/0-387-25101-4_1.
- [15] Segelstein, David J. 1981. “The Complex Refractive Index of Water.” Thesis, University of Missouri–Kansas City. <https://mospace.umsystem.edu/xmlui/handle/10355/11599>.
- [16] Feingold, Graham, and Zev Levin. 1986. “The Lognormal Fit to Raindrop Spectra from Frontal Convective Clouds in Israel.” *J. Climate Appl. Meteor.* 25 (10): 1346–63. [https://doi.org/10.1175/1520-0450\(1986\)025<1346:TLFTRS>2.0.CO;2](https://doi.org/10.1175/1520-0450(1986)025<1346:TLFTRS>2.0.CO;2)
- [17] Ma, Nan, ChunSheng Zhao, Jing Chen, WanYun Xu, Peng Yan, and XiuJi Zhou. 2014. “A Novel Method for Distinguishing Fog and Haze Based on Pm2.5, Visibility, and Relative Humidity.” *Sci. China Earth Sci.* 57 (9): 2156–64. <https://doi.org/10.1007/s11430-014-4885-5>.
- [18] Podzimek, Josef. 1997. “Droplet Concentration and Size Distribution in Haze and Fog.” *Studia Geophysica Et Geodaetica* 41 (3): 277–96. <https://doi.org/10.1023/A:1023350917344>.
- [19] <https://github.com/l3pilot/l3pilot-cdf>, February 2021

- [20] <https://www.oxts.com/wp-content/uploads/2020/03/rtman-200302.pdf>, August 2021
- [21] <https://www.ti.com/sensors/mmwave-radar/overview.html>, January 2022
- [22] <https://www.4activesystems.at/>, January 2022
- [23] <https://cdn.euroncap.com/media/58226/euro-ncap-aeb-vru-test-protocol-v303.pdf>, January 2022
- [24] <https://www.dri-ats.com/>, January 2022
- [25] <https://optek.humaneticsgroup.com/>, January 2022
- [26] <https://www.soflow.com/>, January 2022
- [27] <https://www.abdynamics.com/>, January 2022
- [28] https://en.wikipedia.org/wiki/Hierarchical_Data_Format, January 2022
- [29] <https://www.labsphere.com/labsphere-products-solutions/materials-coatings-2/coatings-materials/permafect-1/>, August 2021
- [30] <https://velodynelidar.com/downloads/datasheets%20first>, e.g. VLP-32C User Manual, August 2021
- [31] Hadj-Bachir, Mokrane, and Philippe de Souza. "LIDAR sensor simulation in adverse weather condition for driving assistance development." (2019). <https://hal.archives-ouvertes.fr/hal-01998668/document>
- [32] <https://www.vinnova.se/p/dimholjt/>, Accessed Sept 2022